

AN ANALYSIS OF GRAVITY MEASUREMENTS ON THE ROSS ICE SHELF, ANTARCTICA

LAWRENCE L. GREISCHAR,¹ CHARLES R. BENTLEY, AND LARRY R. WHITING²

Geophysical and Polar Research Center, University of Wisconsin-Madison, Madison, Wisconsin 53706

During the Ross Ice Shelf Geophysical and Glaciological Survey (RIGGS) field program, between 1973 and 1978, gravity measurements were made at 181 sites on a 55-km grid covering the Ross Ice Shelf and along 350 km of profile lines at base camps. These data and earlier gravity observations on the ice shelf have been reduced using the gravity datum International Gravity Standardization Net 1971 and Geodetic Reference System 1967. Marine gravity data, which have been approximately adjusted to the new datum and reference system, have been used to extend coverage to the edge of the Ross Sea continental shelf. Free-air, Bouguer, and Airy isostatic anomaly maps reveal linear anomalies paralleling the Transantarctic Mountains as a dominant feature. Block faulting due to extension between East Antarctica and West Antarctica is a likely tectonic source for these features. Modeling of local gravity observations made at the five RIGGS base camps revealed probable faulting at every camp. Since location of base camps was not based upon any knowledge of geological structure, the implication is that the seafloor beneath the entire Ross Ice Shelf has been tectonically affected. The correspondence of modeled local structures to regional trends suggests that they are the result of regional tectonic activity. A spectral analysis technique applied to the free-air anomaly, Bouguer anomaly, and bathymetry maps of the Ross embayment revealed that relatively short wavelength (<500 km) topographic loads appear isostatically uncompensated. For these features, which reflect the dominant ridge-trough submarine topography of the embayment, this presumably means that rifting has produced lower crustal densities under the troughs than under the ridges. An apparently negative overcompensation at the longer wavelengths, we believe, is due to glacio-isostatic imbalance. Regional free-air gravity anomalies in the Ross embayment are everywhere negative: they decrease (numerically) from a minimum of -28 mGal along the Siple Coast to -18 mGal in the grid easternmost Ross Sea. The observed field is even more negative than the low-order terms of the satellite-derived free-air anomaly field; the difference increases with distance into the Ross embayment. We interpret this as reflecting the mass deficit left by the Holocene retreat of a more extended grounded ice sheet. A simple exponential model of crustal rebound has been used to derive isochrons of ice retreat. The result generally agrees both spatially and temporally with retreat models based on ice sheet dynamics.

CONTENTS

Introduction	106
Description of the RIGGS program	106
Other gravity measurements on and near the	
Ross Ice Shelf	106
Data Collection and Reduction	106
Field procedures	106
Measurement of gravity and ancillary data	108
Computation of gravity anomalies	112
Gravity anomaly maps	114

Local gravity gradients	123
Modeling of Local Gravity Anomalies	124
Gravity modeling programs	124
Local gravity modeling	124
Discussion of local gravity models	137
Analysis of Isostasy in the Ross Embayment	138
Spatial frequency spectra of gravity and bathymetry	138
Gravity admittance function	141
Speculations on glaciological implications of	
isostatic gravity	143
Isostatic equilibrium grounding line between the West	
Antarctic inland ice sheet and the Ross Ice	
Shelf	151
Summary	151
Appendix	153

¹Now at Department of Meteorology, University of Wisconsin-Madison, Madison, Wisconsin 53706

²Now at P.O. Box 1021, Pocatello, Idaho 83204.

INTRODUCTION

The Ross Sea and Ross Ice Shelf together with the adjacent part of interior West Antarctica between Marie Byrd Land and the Transantarctic Mountains form the Ross embayment, which penetrates more than 1000 km into the Pacific sector of the Antarctic continent. The Ross embayment is a boundary zone between the old continental craton of East Antarctica and the geologically younger mountains of Marie Byrd Land. Study of this area is integral to understanding the evolution of the whole Antarctic plate. In this work we report on gravity studies on the Ross Ice Shelf and integrate the results with other work in the Ross embayment.

Unless otherwise specified, grid coordinates are used throughout this paper. In grid coordinates, meridians are parallel to the prime meridian, and grid north is toward Greenwich, England, i.e., toward the top of an Antarctic map with standard orientation. All our maps have that same orientation.

Description of the RIGGS Program

The Ross Ice Shelf Geophysical and Glaciological Survey (RIGGS) program was an airlifted survey supported by Twin Otter aircraft. Flight operations were carried out over four austral summer seasons (RIGGS I: 1973–1974; RIGGS II: 1974–1975; RIGGS III: 1976–1977; and RIGGS IV: 1977–1978) from four base camps (BC, RI, Q13, and C-16) strategically located on the ice shelf (see Figure 1). In addition, local experiments were carried out at J9DC, the site of the Ross Ice Shelf Project drilling through the ice shelf. Camp J9DC was one of three seasonal camps within 2 km of each other at RIGGS station J9 [Bentley, 1984]. Measurements at a typical geophysical field station comprised radar soundings of ice thickness, seismic soundings of water depth, and gravity measurements. Gravity measurements were made at 181 sites spread at intervals of approximately 55 km (one half of a grid degree) across the Ross Ice Shelf (for specifics, see Bentley [1984]).

Other Gravity Measurements on and Near the Ross Ice Shelf

Several oversnow traverses have crossed parts of the Ross Ice Shelf since the beginning of the International Geophysical Year (see the map in the work of Bentley [1984]). Between 1957 and 1960, the Ross Ice Shelf Traverse (1957–1958), the first Victoria Land Traverse (1985–1959), and the Discovery Deep Traverse (1960) were completed; each included gravity measurements on the ice shelf. Results from

these traverses were given for the ice shelf by Crary *et al.* [1962]. Bennett [1964] further analyzed the gravity data from these traverses and also considered data collected along the Little America Station to Byrd Station Trail. Gravity profiles across eight outlet glaciers through the Transantarctic Mountains at their junction with the ice shelf were presented by Giovinetto *et al.* [1966].

During the austral summers of 1961–1962 and 1962–1963, geophysical studies were carried out on Roosevelt Island (Figure 1), a large ice rise in the grid southwestern part of the ice shelf. Roosevelt Island is 120 km long and 70 km wide, nearly oval in shape, and rises to 500 m above the floating ice that surrounds it. Geophysical studies were part of a program to study the ice flow of this small ice cap. Gravity, magnetic, and seismic measurements made along traverse lines covering Roosevelt Island are summarized in an unpublished manuscript by C. R. Bentley and M. Hochstein (1965).

Marine gravity data were collected in the Ross Sea on cruises 32, 51, and 52 of the USNS *Eltanin* [Hayes *et al.*, 1972, 1978] (Figure 1). Extensive additional data in the grid easternmost Ross Sea (the Victoria Land basin) [Cooper and Davey, 1987] have not been incorporated into our study because the minor effect they would have on the overall gravity picture of the Ross embayment did not seem to us to warrant the large additional computational effort that would have been required to redo all our analyses.

DATA COLLECTION AND REDUCTION

Field Procedures

Two LaCoste and Romberg model G geodetic gravimeters (G-1 and G-19) were used during all four RIGGS seasons. The power required by these meters to maintain a constant internal temperature and to operate the reading light was provided by 12-V rechargeable nickel-cadmium batteries. In addition, jumper cables were used for connection to storage

Fig. 1. (opposite) Map of the Ross embayment showing the locations of gravity measurements and tracks of cruises of the USNS *Eltanin* in the Ross Sea. RIGGS stations are denoted by small solid circles; large solid circles are base camps. Station J9 is a composite station that includes J9DC. Open circles and crosses indicate points of previous surveys. Free-air and Bouguer anomalies have been calculated at all points shown. Cruise tracks are from Hayes *et al.* [1972, 1978]. Names of geographic features referred to in the text are also shown. The grid coordinate system in this and all subsequent maps has its origin at the south pole; the 0° longitude line runs toward Greenwich, England.

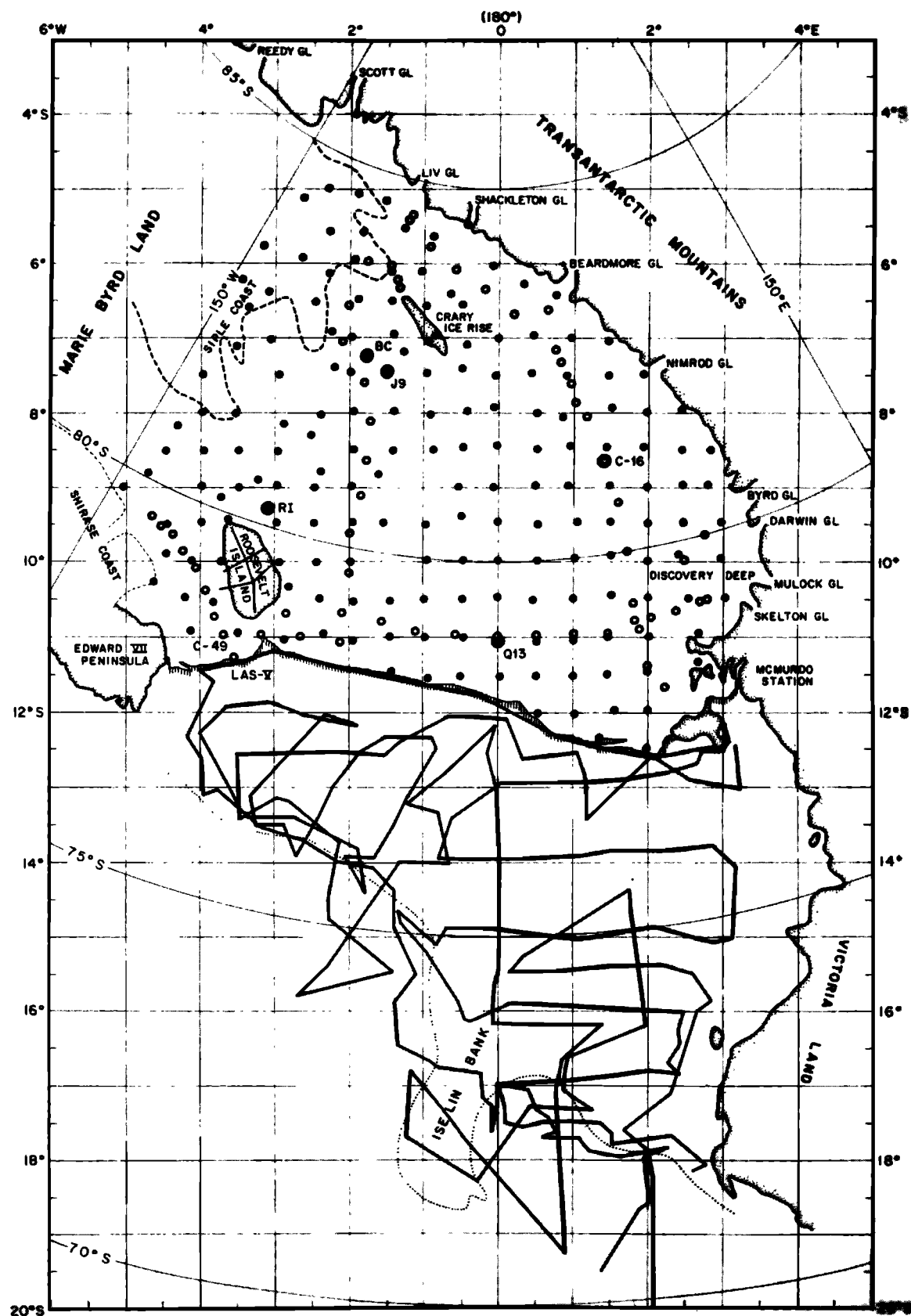


TABLE 1. Absolute Gravity Values at RIGGS Base Camps (Based on McMurdo)

Base Camp	Meter	Date	Gravity Value	Adopted Value
BC	G-1	Dec. 17, 1973	983 085.50	
	G-19	Dec. 17, 1973	085.52	983 085.64 ± 0.16
	G-1	Feb. 3, 1974	983 085.885	
	G-19	Feb. 3, 1974	975.68	
	G-1	Dec. 5, 1974	983 011.05	
RI	G-19	Dec. 16, 1974	001.09	983 001.13 ± 0.25
	G-1	Jan. 27, 1974	983 000.96	
	G-19	Jan. 27, 1975	000.97	
	G-19	Dec. 5, 1976	983 001.59*	983 001.57 ± 0.03
	G-19	Dec. 23, 1976	001.55	
C-16	G-1	Dec. 1, 1976	983 029.90*	
	G-19	Jan. 26, 1977	029.66*	983 029.75 ± 0.13
	G-19	Feb. 8, 1977	029.69	
	G-1	Jan. 17, 1978	983 003.01*	
	G-1	Jan. 23, 1978	029.61	
Q-13	G-1	Jan. 27, 1978	029.79	983 029.76 ± 0.16
	G-19	Jan. 17, 1978	029.63*	
	G-19	Jan. 27, 1978	029.78	
	G-19	Dec. 26, 1976	982 989.24	983 989.26 ± 0.03
	G-19	Jan. 26, 1977	989.28*	
	G-1	Dec. 23, 1977	982 989.24	
	G-1	Jan. 17, 1978	989.02*	982 989.18 ± 0.12
	G-19	Dec. 23, 1977	989.16	
	G-19	Jan. 17, 1978	989.30*	

*Indirect tie.

batteries during extended field operations. Thus except for occasional mishaps, both meters were continuously on heat throughout each season in Antarctica.

A gravity observation at a station consisted of at least two consecutive readings made within a few minutes. Near the ice front, where vertical movements of the ice shelf caused gravity oscillations, many readings were averaged in order to make a satisfactory observation [see Bennett, 1964]. Every series of observations formed a closed loop. A base station at the base camp was occupied at the beginning and end of each day's loop of remote field stations. Meter drift and tares (if any) during each loop were thus determined. The first and last observations for each season were made at the McMurdo base station, part of the International Gravity Standardization Net 1971 (IGSN 71) (see the next subsection).

Transportation to remote field sites was by Twin Otter aircraft. Gravity observations were made upon arrival and just before departure from each field site; as many as five sites were occupied during a day of field operations. At 63% of the stations occupied during RIGGS I and II there was sufficient time to determine gravity gradients by taking readings at the points in a "strain rosette" set up to determine strain rates in the ice [Thomas *et al.*, 1984].

Ice thicknesses and water depths were measured by radar and seismic soundings [Robertson and Bentley,

1990; Albert and Bentley, 1990]. Station positions were determined by a variety of methods including satellite Doppler positioning by geoceivers, sunshots, the inertial navigation system on the Twin Otter, and sighting of landmarks [Bentley, 1984].

When weather conditions precluded flying to remote field sites, gravity measurements were made as part of local surveys around the base camps. Gravity readings were routinely made at all points surveyed for glaciological or other geophysical measurements. In addition, a few lines were surveyed solely to provide data needed to fill in a local gravity map. Station spacings varied from 0.5 to 2.0 km. The terrain surrounding each of the base camps was relatively flat, and elevation differences between adjacent stations probably did not exceed 1 m. Base ties generally were made within about 6 hours so that tidal variations could be approximately removed.

Measurement of Gravity and Ancillary Data

Gravity bases. All RIGGS gravity values are based on the International Gravity Standardization Net 1971, which has both a relative and an absolute accuracy of ±0.1 mGal or better [Morelli, 1971; Hammond and Iliff, 1978; Harrison and LaCoste, 1978]. The primary base station was the McMurdo U.S. Antarctic Research Program (USARP) garage (B) base station

(IGSN 59676D), which is one of a group of gravity bases in McMurdo Sound tied to the world gravity net. It has a value of 982,973.45 mGal relative to IGSN 71.

At base camps BC and RI, piers that consisted of a platform mounted on four 4 × 4 in. posts each extending 3 m into firm were constructed inside small Jamesways. These platforms served both as tie points for field measurements and as bases for a recording gravity meter used to measure the tidal variation of gravity [Williams and Robinson, 1980]. Reading points at C-16 and Q13 were located on the snow surface just outside a Jamesway. Table 1 lists the gravity ties to RIGGS base camps and the adopted gravity values.

The base camps at RI, C-16, and Q13 were used in two different seasons. The movement of the ice shelf is large enough to change the geographic positions of these stations significantly over a 12-month period. However, only at RI, where 2 years passed between occupations, did the gravity value change significantly (Table 1).

Since readings at RI were made on the same pier in both seasons, the 0.44 ± 0.25 mGal increase in the base gravity value between 1974–1975 and 1976–1977 was presumably due to a combination of ice shelf movement and a decrease in elevation. Ice shelf movement at RI is 360 m yr^{-1} in a direction approximately 170° magnetic [Thomas et al., 1984]. The free-air anomaly gradient in that direction is $\sim 0.25 \text{ mGal km}^{-1}$ (Figures 14 and 15); so the movement in 2 years would increase observed gravity at RI by about 0.18 mGal (the latitudinal change is negligible). The surface accumulation rate is 0.15 m yr^{-1} of ice [Thomas et al., 1984], corresponding to about 0.4 m yr^{-1} of snow. Thus Sorge's Law ($\partial p/\partial t = 0$, where p is the density of the firm) would imply a 2-year decrease in elevation of 0.8 m, causing an additional gravity increase of 0.24 mGal. Added together, these two factors essentially match the observed change.

The gravity bases at C-16 and Q13 were on successive snow surfaces, so the elevation change is unknown, although an elevation decrease like that inferred for RI is not to have been expected. Camp Q13 moves along 188° grid at nearly 1 km yr^{-1} [Thomas et al., 1984]; it is difficult to estimate the free-air anomaly change in that direction from the free-air anomaly map (Figure 17), but there is a latitudinal gradient of $-0.31 \text{ mGal km}^{-1}$. The fact that the observed gravity changes only by -0.08 ± 0.12 mGal (Table 1) suggests that the free-air anomaly actually increases by about 0.2 mGal between the successive positions of Q13. At C-16, where the ice movement is 0.5 km yr^{-1} to the grid south [Thomas et al., 1984], the corresponding free-air anomaly and latitudinal gradients are about 1 mGal km^{-1} (Figure

26) and $-0.25 \text{ mGal km}^{-1}$, respectively. The absence of an increase in observed gravity of a few tenths of a milligal in one year at C-16 may reflect the canceling effect of an increase in elevation of the reading point, owing to the buildup of a snow drift hill around the camp buildings between field seasons.

Meter drift and calibration. Corrections for meter drift were computed from differences in base station readings. The drift was assumed to be linear except for cases where jarring the gravity meter caused a tare. In such cases a step variation was introduced into the drift curve. Figure 2 shows drift curves for gravimeter G-1 at C-16 and gravimeter G-19 at Q13, illustrating ocean tidal effects (surface elevation changes), instrumental drift, and tares. It can be seen that long-term instrumental drift is negligible and that the measured tidal effect is less than about 0.3 mGal. Since the tidal gravity variations are smaller than the uncertainty introduced by elevation errors, a theoretical tidal curve was not calculated, nor were observed tidal gravity data, which were sometimes available, applied. The largest tidal variation measured by Williams and Robinson [1980] was approximately 0.5 mGal at spring tide.

Only three tares occurred during the entire RIGGS program, all in the 1976–1977 season. Tare A (~ 0.7 mGal) resulted from rough handling of gravimeter G-19 at McMurdo. Tare B (~ 1.9 mGal) occurred when gravimeter G-19 fell from a snowmobile during the return trip from the magnetic south end of line A at Q13. Tare C (~ 4.8 mGal) occurred from a fall with gravimeter G-1 while deplaning at station N12. Stations in base loops containing tares could be referred to the proper base reading because it was known when each tare occurred. Hence the net effect of the tare on field gravity readings was minimized, although no drift corrections could be applied to stations read in a base loop containing a tare.

Calibrations of gravity meters G-1 and G-19 were checked by a tie between the USARP garage (McMurdo B) base and Christchurch A base (IGSN 71, number 48732A) at the close of the RIGGS III field season in February 1977. Comparison of this tie with the accepted IGSN 71 gravity difference revealed the following:

1. The manufacturer's calibration for gravimeter G-1 (dated 1960) yields an error of about 1.04 mGal over the 2479.16-mGal difference between the bases (McMurdo B: 982,973.45 mGal; Christchurch A: 980,494.29 mGal).

2. The calibration of gravimeter G-19 made by the Army Map Service in 1964 over 46 stations of the North American Calibration Line from Point Barrow, Alaska, to Paso de Cortez, Mexico, leads to agreement with the IGSN 71 difference between McMurdo and Christchurch to within 0.1 mGal.

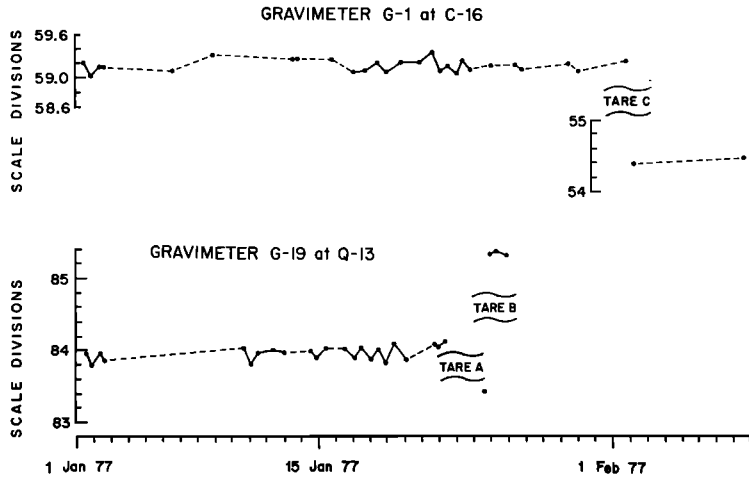


Fig. 2. Gravimeter drift curves during January 1977 (RIGGS III). Ordinates are in scale divisions on the gravimeter dials; one scale division very nearly equals one milligal. Tares are described in the text.

Gravity ties between McMurdo and South Pole stations made during each RIGGS field season as part of a long-term program of measuring the secular change of gravity at South Pole Station showed good agreement between gravimeters G-1 and G-19, after the adjustment determined in point 1 was applied to readings with gravimeter G-1. The largest disagreement over the 661-mGal difference between the two stations was 0.07 mGal. The secular change in gravity at "new" South Pole Station measured during the RIGGS program (0.10 ± 0.03 mGal/yr $^{-1}$) between February 1974 and October 1978 agrees with the change measured at "old" South Pole Station during the period December 1957 to November 1967 (0.10 ± 0.01 mGal/yr $^{-1}$) [Behrendt, 1967; Bentley, 1971]. Thus it appears that the calibrations for gravity meters G-1 and G-19 are stable and that it is valid to use these calibrations throughout the RIGGS program, particularly over the relatively small range (~216 mGal) of gravity values measured on the Ross Ice Shelf.

Determination of positions, elevations, and thicknesses. Geographic positions of RIGGS stations were determined by four different methods [Bentley, 1984]. Approximately two thirds of the RIGGS station positions were determined by satellite Doppler fixes, with an accuracy of better than ± 10 m [Thomas *et al.*, 1984]. Most of the remaining stations were fixed by sunshots to an accuracy of about 1 km. At 13 stations where neither a satellite fix nor a sunshot position was available, the position indicated by the inertial navigation system (INS) of the Twin Otter aircraft was used; the estimated accuracy for these positions is ± 3 km. Finally, at seven stations near the end of the RIGGS IV field season where the INS on the Twin Otter failed to operate, positions were determined by

sights taken on Mount Erebus, Mount Terror, Mount Discovery, and the tip of Minna Bluff (see Figure 1). These positions are estimated to be accurate to within ± 5 km [Greischar *et al.*, 1978].

Surface elevations e at RIGGS stations on floating ice were calculated by assuming the ice to be floating in hydrostatic equilibrium with seawater according to the following equation:

$$e = \frac{(\rho_w - \bar{\rho}_i)}{\rho_w} h_i + \frac{\bar{\rho}_i}{\rho_w} \delta \quad (1)$$

where $\delta = h_i (1 - \bar{\rho}_i/\rho_w)$, h_i is ice thickness, ρ_i and ρ_w are densities of ice and water, respectively, and $\bar{\rho}_i$ is the vertically averaged density in the ice shelf; δ is a correction value to be subtracted from e and h_i to reduce them to equivalent values for solid ice [Shabtaie and Bentley, 1982].

Direct measurements and seismic determinations of densities in the upper 100 m of the ice shelf both have been reported [Crary *et al.*, 1962; Robertson and Bentley, 1990; Langway, 1975; Chiang and Langway, 1978; Kirchner and Bentley, 1990; Albert and Bentley, 1990]. Table 2 shows average densities to 100 m, $(\bar{\rho}_i)_{100}$, calculated by using seismic determinations down to the maximum depth of wave penetration, z_{\max} (54–70 m), and assuming a linear increase in density below z_{\max} to an assumed value of 0.910 Mg m $^{-3}$ at 100 m (rounded off from a density of 0.908 Mg m $^{-3}$ at 101 m at Little America Station [Gow, 1963]). Also listed in Table 2 are values of $(\bar{\rho}_i)_{100}$ calculated from measurements on ice cores from Little America Station and RIGGS station J9DS (a substation of station J9). 16 seismically determined values of $(\bar{\rho}_i)_{100}$ range from 0.763 Mg m $^{-3}$ to 0.794 Mg m $^{-3}$ with a

TABLE 2. Densities in the Upper Ross Ice Shelf, From Seismic and Core Studies

Station	z_{\max} , m	Density at z_{\max} , Mg m^{-3}	Average Density Surface to z_{\max} Mg m^{-3}	Average Density, Upper 100 m, Mg m^{-3}	Source
BC	70	0.905	0.736	0.787	a
H7	70	0.901	0.727	0.781	a
H11S	70	0.889	0.708	0.765	a
J7S	70	0.904	0.730	0.783	a
J9DS	70	0.890	0.721	0.775	a
K11	70	0.889	0.728	0.779	a
P5	70	0.890	0.704	0.763	a
RI	70	0.909	0.722	0.778	a
C16	55	0.883	0.692	0.784	b
J9DC	54	0.902	0.699	0.794	b
H13	56	0.868	0.675	0.770	b
M14	54	0.893	0.699	0.792	b
Q13	56	0.892	0.691	0.783	b
O11	56	0.888	0.688	0.781	c
O19	57	0.889	0.696	0.784	c
R16	56	0.882	0.684	0.778	c
LAS	ice core			0.763	d
J9DS	ice core			0.774	e

Sources: (a) Robertson and Bentley [1990]; (b) Kirchner and Bentley [1990]; (c) Albert and Bentley [1990]; (d) Gow [1963]; (e) Langway [1975].

mean of 0.780 Mg m^{-3} and a standard deviation of 0.009 Mg m^{-3} . The agreement with the average of directly measured densities at the one common station, J9DS, is excellent [Kirchner and Bentley, 1990].

Using $\rho_i = 0.910 \text{ kg m}^{-3}$, $\rho_w = 1.029 \text{ kg m}^{-3}$ (at a temperature of -2°C and a salinity of 35% [Crary, 1961a]), and $\delta = 14.3$ (average for the 16 stations in Table 2) in equation (1) for e and h_i in meters gives

$$e = 0.116h_i + 12.6 \quad (2)$$

Elevations computed for lower bound and upper bound ice thicknesses of 200 m and 900 m, respectively, and lower bound and upper bound average densities for the upper 100 m of ice (Table 3) show that the uncertainty in elevation arising from the adoption of a single mean value of δ is no more than 2 m. There is also an elevation error due to uncertainties in the ice thickness given simply by $de/dh_i = 0.116$.

The uncertainty in ice thickness is about ± 10 m [Robertson and Bentley, 1990; Albert and Bentley, 1990]; so the total uncertainty in surface elevation is about ± 3 m. A comparison of elevations computed as above and satellite elevations computed in relation to the GEM 10C geoid at RIGGS stations where at least two satellite-determined elevations were available (S. Shabtaie, personal communication, 1990) yielded a mean difference (hydrostatic minus satellite) insignificantly different from zero: -1.2 ± 4.3 m for 60 stations.

One check point on the ice shelf is available: the hole through the ice at station J9DC [Clough and Hansen, 1979]. The surface height there was determined to be 59.6 m above sea level [Shabtaie and Bentley, 1987], close to the value of 60.7 m calculated from equation (2) for $h_i = 415$ m [Albert and Bentley, 1990].

Elevations at grounded stations F7, I10S, J4, and KL7 were determined by satellite observations to an

TABLE 3. Variation of Elevation With Average Density of Upper 100 m of Ice Shelf

Ice Thickness, m	Average Density, Upper 100m, Mg m^{-3}	Average Density, Ice Shelf, Mg m^{-3}	Surface Elevation, m
200	0.763	0.836	37.5
200	0.794	0.852	34.4
900	0.763	0.894	118.1
900	0.794	0.897	115.5

accuracy of about ± 5 m. Measurements of the elevation at the other three grounded stations (F10, I10, and Q18) were made only with altimeters. Both a hand-carried altimeter and the altimeter of the Twin Otter were used to measure elevation differences between those stations and either the base camp or the nearest floating station. Altimetry errors are difficult to determine; we will follow Bentley [1964] and take ± 10 m for instrument error and 0.1 m per kilometer distance from the reference point for the pressure gradient effect. That distance was of the order of 100 km, giving another ± 10 -m elevation error. We will take the sum of these two factors, ± 20 m, as a reasonable estimate of the elevation error at those stations.

Evaluation of satellite elevations by Shabtaie and Bentley [1987] revealed that seven RIGGS stations grid northwest of Crary Ice Rise previously believed to be floating were actually on grounded ice. Elevations for these stations were interpolated from the contour map of Shabtaie and Bentley [1987, Figure 10, p. 1324] to an estimated accuracy of ± 10 m.

The thickness of the water layer at RIGGS stations was measured either by seismic reflections alone or by seismic echoes from the seafloor combined with ice thicknesses determined by radar. The error in water layer thickness was estimated to be ± 5 m [Robertson and Bentley, 1990; Albert and Bentley, 1990]. Combining this with the error in ice thickness determination gives ± 15 m for the uncertainty in the depth of the seafloor.

Computation of Gravity Anomalies

The gravity anomaly at a point on the Earth's surface is the difference between the value of gravity observed at that point and a corresponding theoretical gravity value computed there. In this paper we calculate and examine the free-air, Bouguer, and Airy isostatic anomalies (listed in the appendix).

Theoretical gravity. The theoretical gravity at an observation point at latitude ϕ is the value at that latitude on an ideal equipotential surface (reference ellipsoid) given by a standard gravity formula. The formula that approximates the Earth's gravitational field has been modified several times since the turn of the century as the amount and precision of gravity and geodetic information have increased. We used the gravity formula adopted by the International Union of Geodesy and Geophysics in 1967 [Morelli, 1971] known as the Geodetic Reference System (GRS) 1967 [Woollard, 1979]. Data from RIGGS and all data used in this paper were reduced using the GRS 1967:

$$\gamma = 978031.85 [1 + 0.0053024 \sin^2(\phi) - 0.0000059 \sin^2(2\phi)] \quad (3)$$

where γ is the gravity value (in milligals) on the reference ellipsoid and ϕ is the latitude.

Differentiating (3) yields, for the latitude correction to gravity, $0.815 \sin 2\phi$ mGal km $^{-1}$. This varies from 0.15 to 0.35 across the range of latitudes of RIGGS stations; at a nominal latitude of 80° it is 0.28 mGal km $^{-1}$.

Free-air anomaly. The free-air (elevation) correction is $0.3086e$ mGal (e is in meters), whence the free-air anomaly, Δf_{fa} , becomes $\Delta f_{fa} = g_{obs} + 0.3086e - \gamma$ where g_{obs} is the observed gravity value.

Bouguer anomaly. The effect of the mass between the observation point and sea level is generally approximated by the Bouguer correction for an infinite horizontal slab, δg_B :

$$\delta g_B = 2\pi G\rho e = 0.0419\rho e \quad (4)$$

where ρ is the density of the material in the slab (in megagrams per cubic meter), i.e., between the observation point and sea level. The Bouguer correction is subtracted to remove the effect of the intervening mass in adjusting g_{obs} to sea level. The application of both the Bouguer and the free-air corrections to g_{obs} gives the simple Bouguer anomaly ("simple" means "without terrain corrections").

At sea level on land, since both corrections are zero, the free-air and Bouguer anomalies are the same. On the ocean, however, it is standard practice to extend the Bouguer correction to the mass deficit between the ocean water and crustal rock: in equation (4) e becomes d_w , the ocean depth (in meters), and ρ becomes $\rho_r - \rho_w$, the density difference between water and rock, and the correction is now added. Bouguer anomalies were calculated in this way for the RIGGS measurements made on the ice shelf. (Note that on ice floating in hydrostatic equilibrium, $\delta g_B = 0.0419(\rho_r - \rho_w)d_w$ independent of the surface elevation.) Taking $\rho_r = 2.67$ Mg m $^{-3}$ and $\rho_w = 1.028$ Mg m $^{-3}$, we then have for the Bouguer anomaly on the ice shelf, δg_B ,

$$\delta g_B = g_{obs} + 0.3086e + 0.0687d_w - \gamma$$

For consistency, Bouguer anomalies at grounded RIGGS stations were also calculated by replacing ice below sea level with rock.

A terrain correction, which is sometimes applied to correct for the deviation of the real Earth from a flat Bouguer slab, was not included in our data reduction. The ice shelf is very flat and local sea bottom slopes, measured beneath seismic spreads of the order of 1 km in length, are mostly less than 1°; only 7 of the 56 observed local slopes are larger than that [Crary et al., 1962; Robertson, 1975]. Furthermore, since the RIGGS gravity observations were made on the surface of the ice shelf which is hundreds of meters above the

seafloor, the gravitational effects of local submarine topographic highs and lows tend to cancel, thereby diminishing the terrain effect.

Airy isostatic anomaly. An isostatic gravity correction attempts to account for the gravitational effects of the masses associated with isostatic compensation. For topographic features that are large in comparison with depths of compensation, the Bouguer and isostatic corrections are nearly equal, so that the combined correction approaches zero. On the other hand, for topographic features that are small in comparison with depths of compensation, the gravitational effect of the compensating mass is relatively small; so the combined Bouguer-isostatic correction approaches the Bouguer correction.

An idea of the magnitude of the gravity disturbance due to compensated surface masses can be obtained from a model composed of one or more circular disks [Nettleton, 1976, Figure 7A-8, p. 232]. For compensation at a depth of 30 km, the combined Bouguer-isostatic correction for a circular topographic feature 40 km across is 83% of the simple Bouguer correction, but it drops to only 35% of the simple Bouguer correction for features 160 km across (Table 4). A topographic feature as large as the Ross embayment would retain a combined Bouguer-isostatic correction equal to about 5% of the simple Bouguer correction. Taking an average water depth of 600 m in the Ross embayment, the combined Bouguer-isostatic correction would be approximately 2 mGal.

The Airy mechanism of perfect local isostatic compensation, whereby topographic features are balanced by crustal roots (antiroots in oceanic regions) in the mantle, has been assumed for our calculations. Isostatic corrections were computed using the three-dimensional Talwani procedure [Talwani and Ewing, 1960]. A constant crustal thickness of 30 km throughout the Ross embayment was assumed. That value was based on data available at the time of RIGGS [Bentley, 1973]; the crust is now believed to be about 5 km thinner [Cooper et al., 1991]. As explained below, changing the assumed thickness by 5 km would change the average isostatic anomaly only

by about 1 mGal; anomalies were therefore not recalculated. Densities of 2.67 Mg m^{-3} for the upper crust, 2.95 Mg m^{-3} for the lower crust, and 3.32 Mg m^{-3} for mantle material were used. For 243 gravity stations on the Ross Ice Shelf, the mean isostatic correction was -42.02 mGal .

The Airy isostatic gravity anomaly, δg_A , is given by

$$\Delta g_A = g_{\text{obs}} + 0.3086e + 0.0687d_w + \delta g_A - \gamma$$

where δg_A , the computed Airy isostatic correction, is negative everywhere on floating ice.

The isostatic correction is insensitive to changes in the choice of density, since the mass of the isostatic compensation remains fixed. Furthermore, particularly in a region of subdued submarine topography such as the Ross embayment, the isostatic anomalies are insensitive to a change in isostatic model. Kososki [1972] calculated both Pratt-Hayford and Airy-Heiskanen average isostatic anomalies for one-degree ($111 \text{ km by } 111 \text{ km}$) squares for West Antarctica and found that differences between individual anomalies rarely exceeded 2 mGal, even in the mountainous interior. Similarly, the crustal thickness assumed for the Airy model is unimportant. For a typical feature in the Ross embayment with a linear dimension of approximately 160 km and relief of the order of 200 m, corresponding to a simple Bouguer correction of 14 mGal, the isostatic correction would change only 2 mGal for a 10-km change in crustal thickness (Table 4).

Errors in gravity anomalies. The various contributions to the estimated errors for free-air and Bouguer anomalies at field stations are listed in Table 5. Errors from uncertainty in latitude were evaluated at a latitude of 80° . At the 94% of the RIGGS stations located on the floating ice shelf, gravity anomalies are accurate to about $\pm 2 \text{ mGal}$. For grounded stations the error ranges from 2 mGal to 6 mGal, depending on the method of elevation determination.

Bennett [1964] estimated the accuracy of pre-RIGGS gravity stations on the ice shelf to be $\pm 6 \text{ mGal}$ for both free-air and Bouguer values; the larger errors in his work stem from larger uncertainties in surface elevations, which were determined by altimetry alone.

TABLE 4. Magnitude of Combined Airy-Isostatic and Bouguer Correction Relative to Bouguer Correction Alone for Cylindrical Disks

Diameter, km	Crustal Thickness, %		
	20 km	30 km	40 km
40	71	83	90
160	23	35	46
320	11	17	23
800	4	7	9
1600	2	3	4

TABLE 5. Estimated Errors in Gravity Anomalies

Measurement	Method or Source	Error, mGal	
		Free-Air Anomaly	Bouguer Anomaly
Elevations (surface and bed)			
Floating stations	hydrostatic balance	0.9	1.9
Grounded stations	satellite	1.6	2.6
	map [<i>Shabtaie and Bentley, 1987</i>]	3.1	3.4
	altimetry	6.2	6.1
Latitude	satellite	0	0
	sunshot	0.3	0.3
	INS	0.8	0.8
	landmark	1.4	1.4
Earth and ocean tides	<i>Williams and Robinson [1980]</i>	0.5	0.5
Base station value	<i>Morelli [1971]</i>	0.1	0.1
Total error (rms)	floating stations	1.0–1.8	2.0–2.4
	grounded stations	1.7–6.4	2.6–6.3

Gravity Anomaly Maps

Figures 3a and 4a show the free-air and Bouguer gravity anomaly maps of the Ross embayment, respectively. Versions of the same maps filtered to remove wavelengths less than ~160 km are shown in Figures 3b and 4b. The data in the Ross Sea were approximately adjusted to the new reference system and datum (GRS 67 and IGSN 71) by applying a constant correction of ~10 mGal [*Bentley and Robertson, 1982*]. The bathymetric map of the Ross embayment (reproduced in Figure 5a; the filtered version is in Figure 5b), prepared by *Albert et al. [1978]* and published in the work of *Albert and Bentley [1990]*, was used to compute the Airy isostatic gravity anomaly map.

Aliasing is sure to be present in the maps, since the measurement points are approximately 55 km apart over most of the ice shelf and the distance between ship's tracks in the Ross Sea was mostly even more. There are some clues to the magnitude of the resulting error. As discussed below, 65% of the 57 gravity gradients measured in the grid western part of the Ross Ice Shelf agree in direction (within $\pm 60^\circ$) with the regional gradient of the free-air anomaly map. All the local gravity surveys at RIGGS base camps (see below) showed considerable variation in gravity over distances of a few tens of kilometers (30 mGal at Q13 and C-16, 9 mGal at J9DC, 16 mGal at RI, and 14 mGal at BC), but the local variations are generally consistent with the regional anomaly field. Departures of the gravity anomaly values at Q13, C-16, J9DC, BC, and RI from the average gravity anomaly values estimated from the local coverage at these stations are approximately +6, -4, -5, +4, and -3 mGal, respectively. From those

figures we estimate ± 5 mGal for the error in using station anomaly values to represent the mean anomaly for the 0.5° square surrounding each station. This error, combined with the errors in the anomalies themselves, is large enough to suggest that any features on the following maps defined by only one 10-mGal contour interval are of questionable significance.

We base the following discussion on the unfiltered maps, to which the specific positions cited refer, but most of the features can be seen, many of them more clearly, on the filtered maps, to which we direct the reader also.

Free-air anomaly map. Except for a few isolated anomalies, free-air gravity values in the Ross embayment (Figure 3) are negative. Several of the free-air anomalies are clearly related to bottom topography (Figure 5); several more are not. Most notable of the former are the linear high-low gravity anomalies over the ridge-trough topography of the grid northwestern area of the ice shelf, the gravity high on Roosevelt Island, the low directly grid southwest of Roosevelt Island (grid 11°S , 3.5°W), the gravity low over Discovery Deep (grid 10.6°S , 2.7°E), and the gravity lows adjacent to Ross Island (grid 12°S , 2°E). Anomalies not clearly associated with submarine topography include the gravity low directly grid southeast of Roosevelt Island (grid 10.7°S , 2.8°W), the large gravity high trending grid north-south in the Ross Sea between 1°E and 2°E (grid), and gravity lows roughly paralleling the continental shelf edge in the Ross Sea. *Bennett [1964]* suggested that the gravity low grid southeast of Roosevelt Island may be due to a low-density granitic intrusion, and *Hayes and Davey [1975]* postulate a similar source for the gravity lows near the edge of the

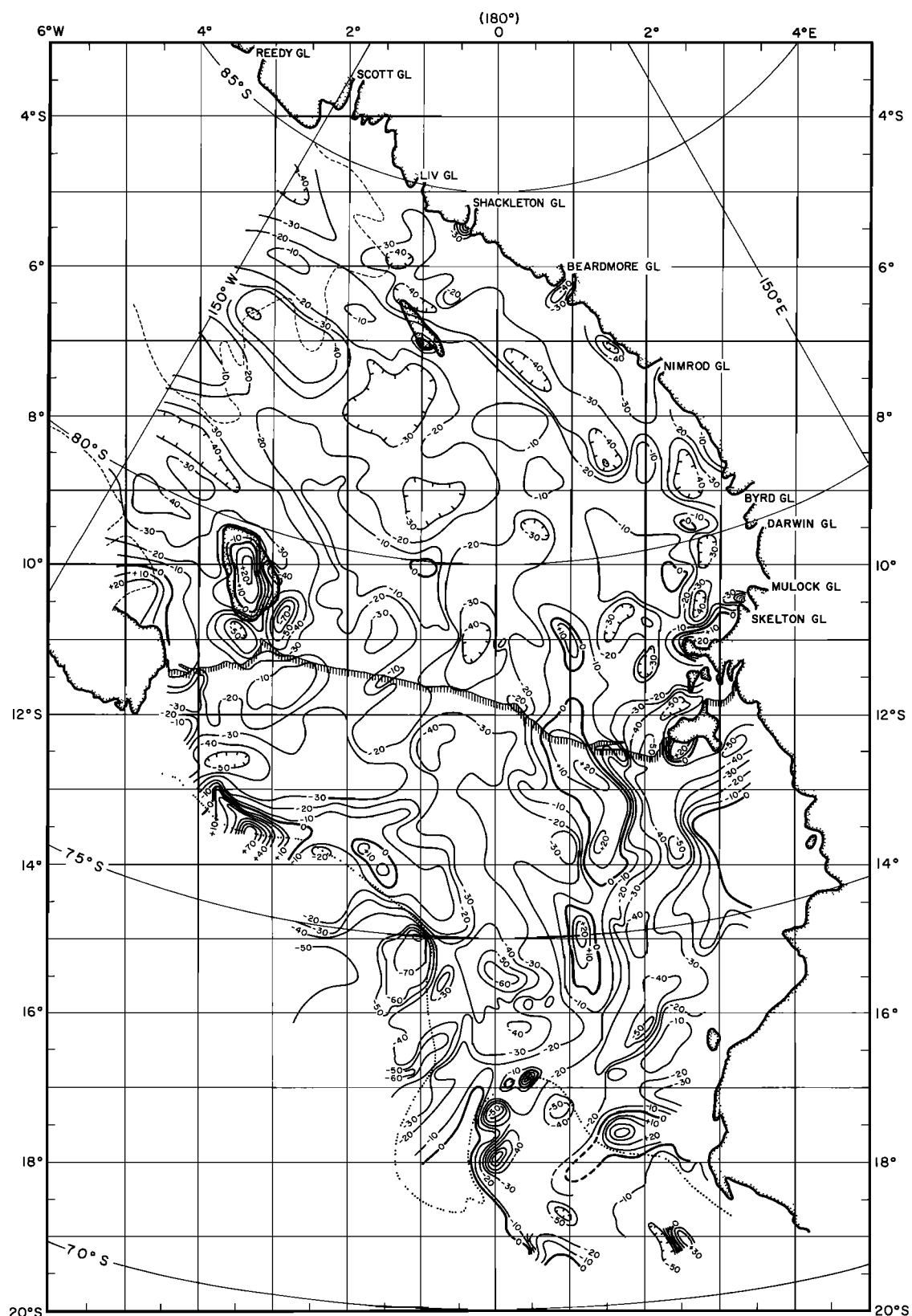


Fig. 3a. Map of free-air anomalies in the Ross embayment. The contour interval is 10 mGal. A heavy line marks the 0-mGal contour.

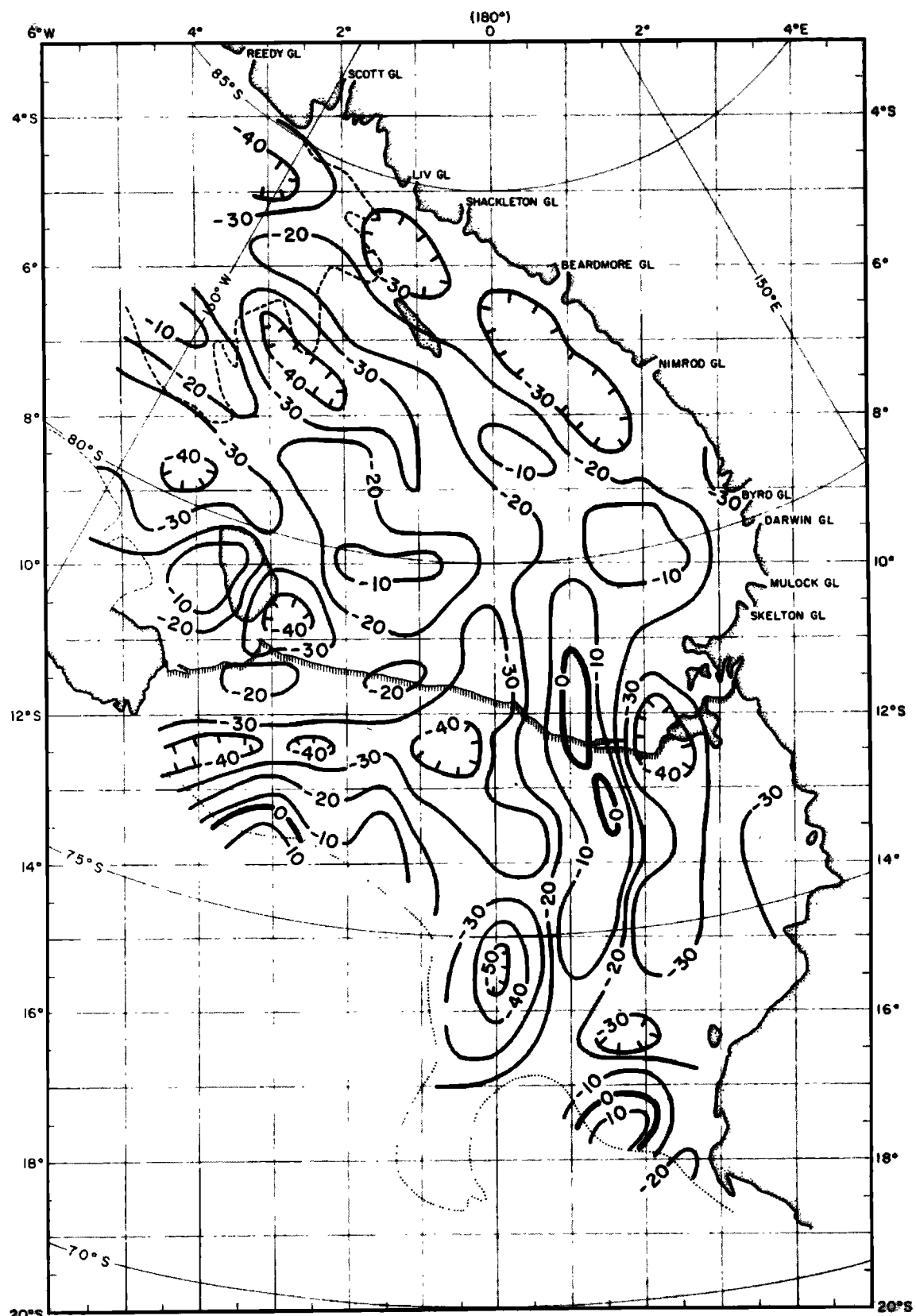


Fig. 3b. Map of free-air anomalies in the Ross embayment, filtered to remove wavelengths less than 160 km. The contour interval is 10 mGal. A heavy line denotes the 0-mGal contour.

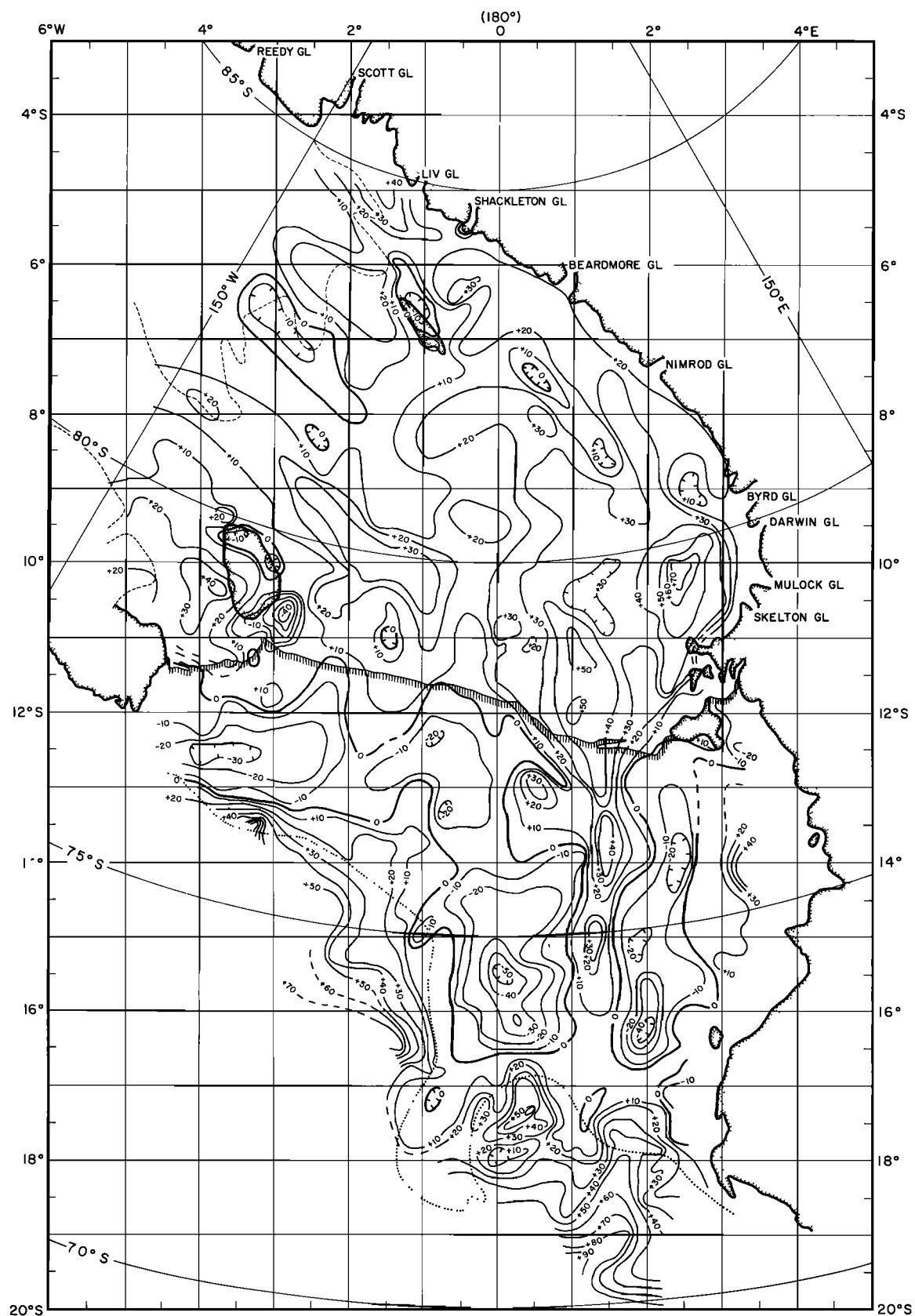


Fig. 4a. Map of Bouguer anomalies in the Ross embayment. The contour interval is 10 mGal. A heavy line marks the 0-mGal contour. RIGGS base camps are denoted by black circles.

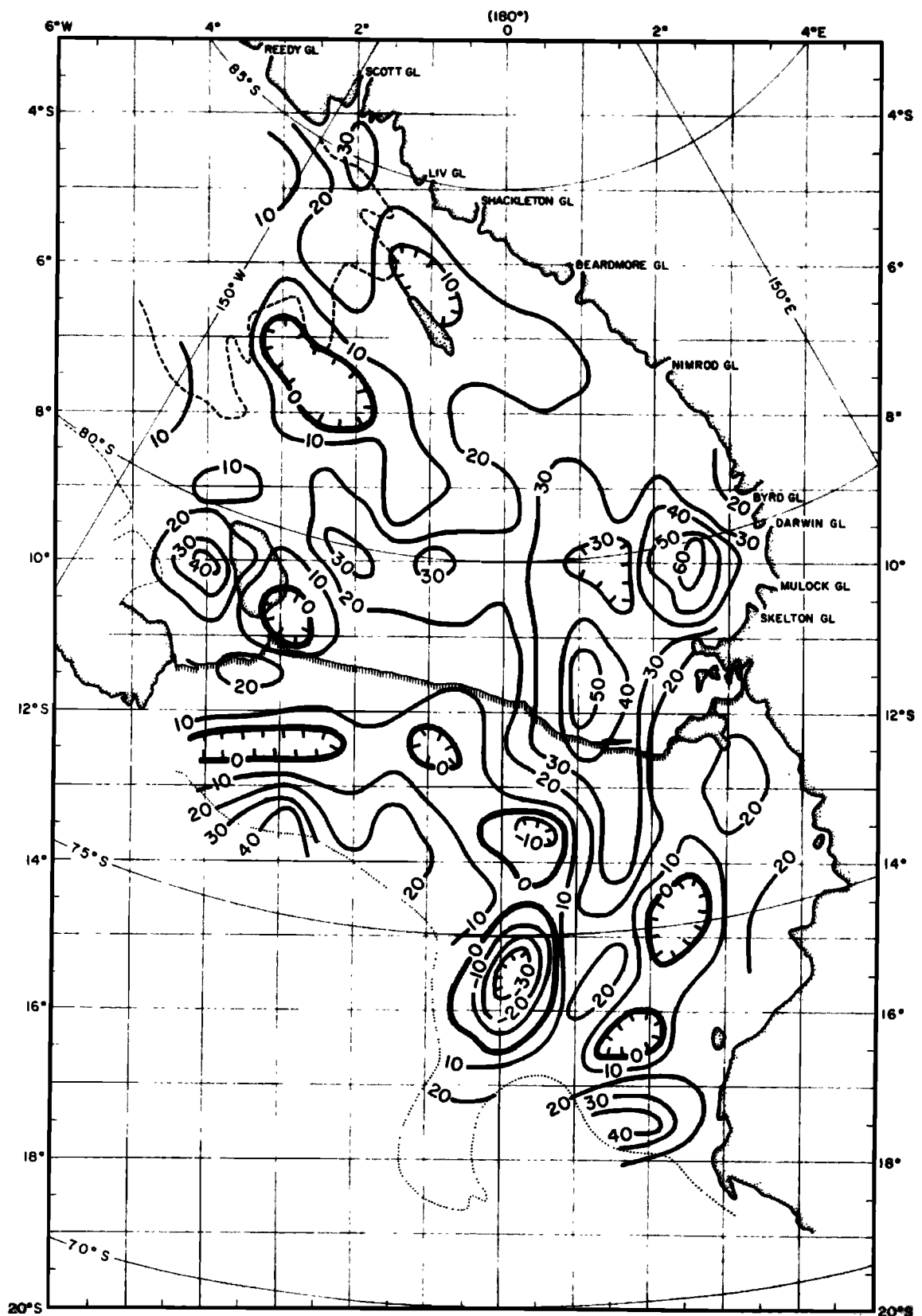


Fig. 4b. Map of Bouguer anomalies in the Ross embayment, filtered to remove wavelengths less than 160 km. The contour interval is 10 mGal. A heavy line denotes the 0-mGal contour.

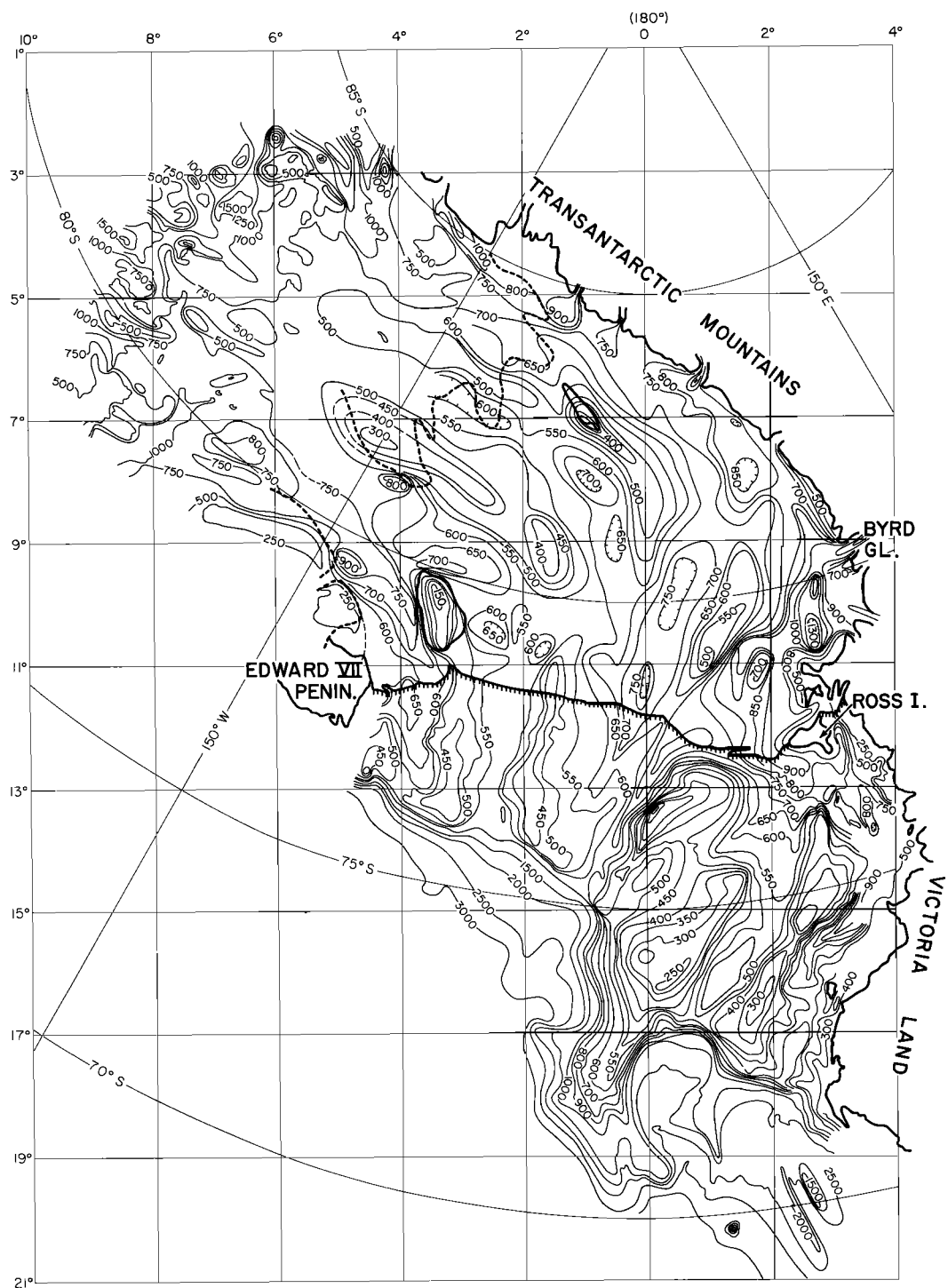


Fig. 5a. Map of submarine topography in the Ross embayment. The contour interval is 50 m beneath the Ross Ice Shelf and in the Ross Sea and 250 m under the inland ice in the grid northwest. RIGGS base camps are denoted by black circles.

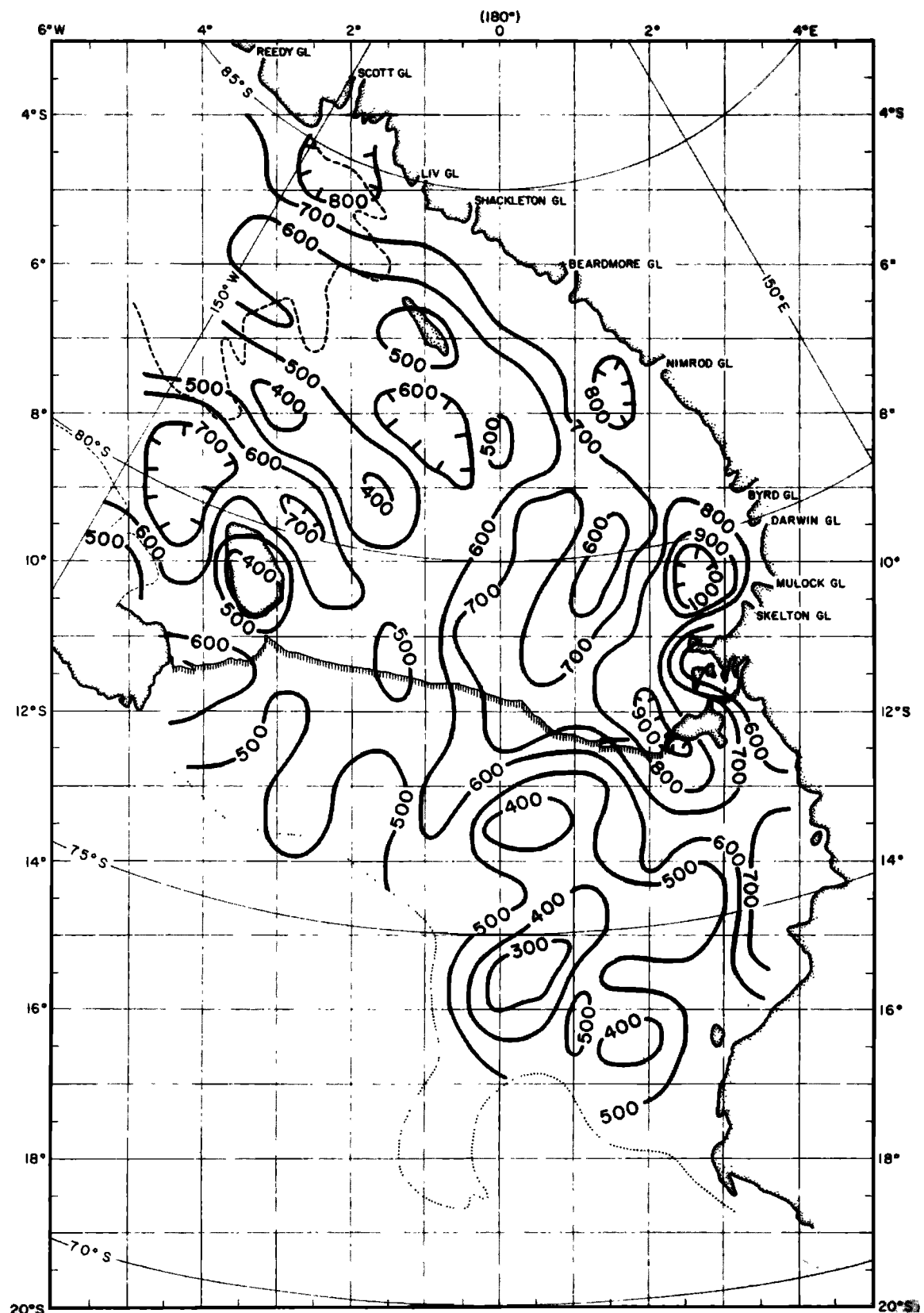


Fig. 5b. Map of submarine topography anomalies in the Ross embayment, filtered to remove wavelengths less than 160 km. The contour interval is 50 m.

continental shelf at grid 15.5°S , 0°W and grid 12.5°S , 3.5°W . Hayes and Davey [1975] modeled the large north-south trending gravity high in the central Ross Sea as a high-density intrusion into the upper crust, probably the result of crustal rifting. For a comprehensive discussion of the relationship between gravity anomalies and upper crustal structure on the Ross Sea continental shelf that includes many new data, particularly for the grid eastern Ross Sea, see Davey and Cooper [1987].

Bouguer gravity anomaly map. The Bouguer gravity anomaly map (Figure 4) emphasizes density contrasts beneath the seafloor including those due to masses compensating topographic loads. Correlation with bottom topography is largely removed except where topographic loads are extensive enough to be isostatically compensated.

The Bouguer gravity anomaly map can be divided into three regions based on anomaly amplitudes and trends. The first, around and grid south of Roosevelt Island, is characterized by roughly circular Bouguer anomalies with one anomaly as negative as -40 mGal (grid 10.3°S , 3.7°W) and one as large as $+40$ mGal (grid 10.6°S , 2.7°E). These anomalies may be related to low-density and high-density intrusions associated with Marie Byrd Land (see the paragraph on Roosevelt Island anomalies below).

The linearly trending anomalies over the ridges and troughs in the second region, between Roosevelt Island and the Transantarctic Mountains, range from -10 to $+40$ mGal. They are generally supposed to arise from horst and graben structures that have resulted from rifting between the Transantarctic Mountains and Marie Byrd Land [Elliot, 1980; Davey, 1987; Cooper et al., 1991; Behrendt et al., 1991]. Vertical crustal displacements of 1 or 2 km could easily account for these anomalies.

Grid southeast of a curved line extending from Byrd Glacier to the edge of the continental shelf grid west of Iselin Bank is the third region, characterized by grid north-south trending anomalies ranging from -50 to $+70$ mGal. The association of these anomalies with basins and highs beneath the shelf is discussed by Davey and Cooper [1987].

Airy isostatic gravity anomaly map. The isostatic anomalies (Figure 6) generally are intermediate between the free-air and Bouguer anomalies: as was pointed out above, the isostatic anomaly map approximates the Bouguer anomaly map over local topographic features, and the free-air anomaly map, over regional features. It is important to note that nonzero isostatic anomalies do not necessarily imply lack of isostatic equilibrium, particularly in regions of lateral density variations [Simpson et al., 1986]. However, it is unlikely that a region with a small isostatic anomaly is greatly out of balance.

It appears from Figure 6 that large areas of the seafloor below the ice shelf are in isostatic equilibrium. In particular, free-air anomalies at Discovery Deep (grid 10.6°S , 2.7°E), on Roosevelt Island, and on Crary Ice Rise have been removed by the isostatic correction, which implies that these features are isostatically equilibrated.

Several regions of pronounced isostatic anomalies remain, however. An elongated isostatic anomaly low reaching -40 mGal is centered over and parallel to the grid eastern edge of Roosevelt Island. This low extends grid north-northwest from the large closed low (-77 mGal) directly grid southeast of Roosevelt Island to grid 8.5°S , 4.0°W . Grid west of Roosevelt Island, however, the isostatic anomaly is small, which implies isostatic equilibrium of the topographic trough there (Figure 5a) as well as of Roosevelt Island.

The linear free-air anomalies that extend grid southeast from the West Antarctic grounding line remain on the isostatic map. Particularly pronounced, and scarcely smaller here than on the free-air map, is the anomaly of -30 to -40 mGal that runs parallel to the Transantarctic Mountains from grid northwest of Crary Ice Rise at 150°W longitude (grid 5°S , 3°W) to base station C-16. Grid northeast of Crary Ice Rise (grid 6.5°S , 0.5°W) left-lateral displacement of this low trend is suggested.

The negative anomaly is bounded to the grid northeast by a linear isostatic anomaly high that is even more pronounced than the corresponding free-air anomaly. The occurrence of this relative high over the submarine trough adjacent to the Transantarctic Mountains argues against the presence beneath the ice shelf of a thick sedimentary section such as the one (the Victoria Land basin) modeled by Stern and ten Brink [1989] for the East Antarctic/West Antarctic boundary in the Ross Sea. Also, the linear high that parallels the Transantarctic Mountains about 200 km offshore which, in the Ross Sea, Stern and ten Brink [1989] interpret as being linked with downward flexure at the western margin of the Ross embayment, is seen here (grid 6°S , 3°W to grid 10°S , 2°E), farther into the embayment, to be the middle one of three similar highs.

The low that trends from the Siple Coast at grid 6.5°S , 3°W to grid 9°S , 1°W is narrower and less continuous on the isostatic map than on the free-air map. In the extreme grid western part of the survey area, the anomaly is not centered on the topographic trench (grid 6.7°S , 3°W ; Figure 5a), but it instead lies over the flank of the topographic ridge to the grid north of it. The pinching of the anomaly in the center of the survey area (grid 8°S , 1°W) appears to be associated with a crosscutting trend that runs grid northeastward to near the Transantarctic Mountains. The positive trend running from the grid southern

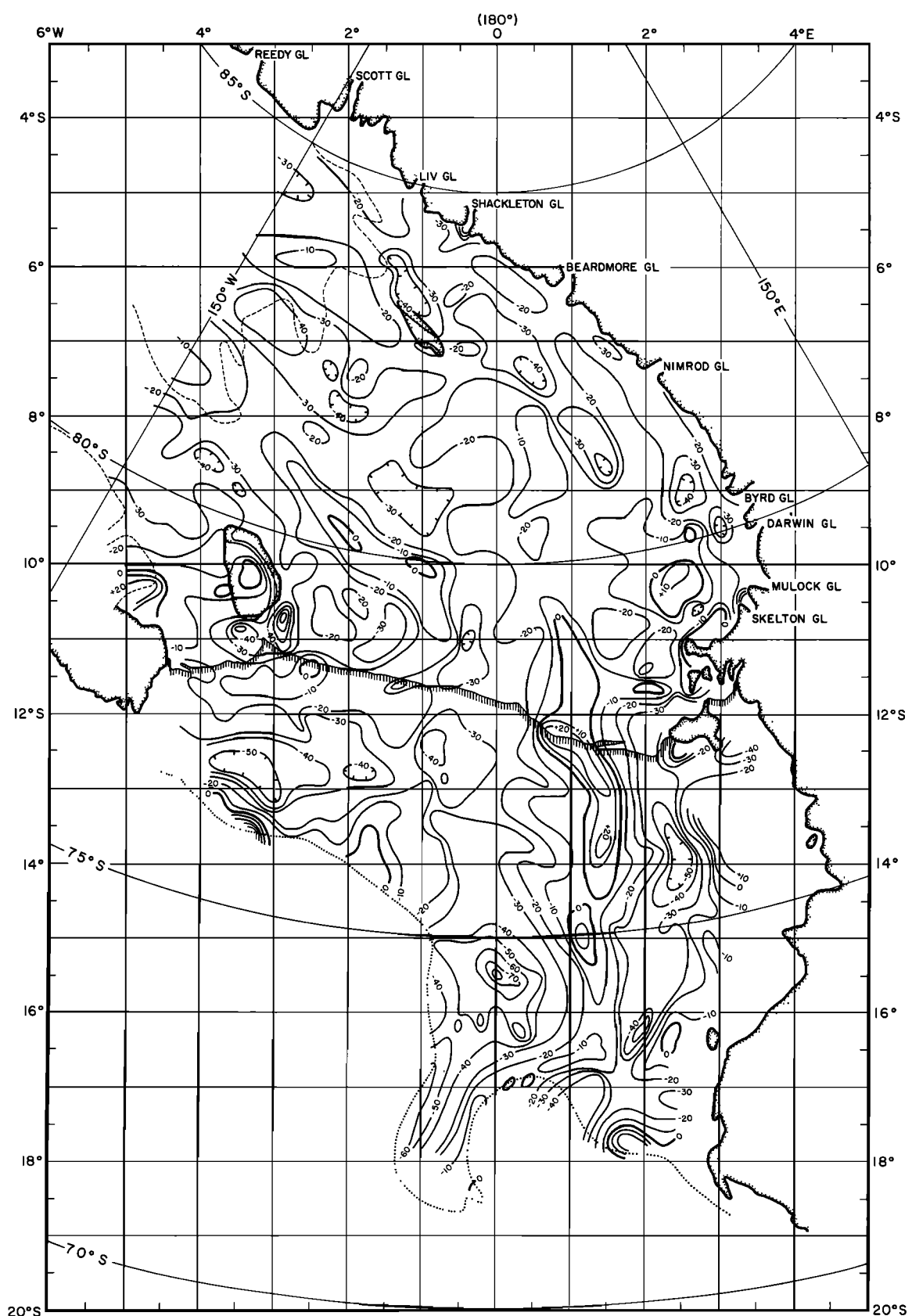


Fig. 6. Map of Airy isostatic anomalies in the Ross embayment. The contour interval is 10 mGal. A heavy line marks the 0-mGal contour. RIGGS base camps are denoted by black circles.

Siple Coast (grid 7.5°S , 4°W) to grid 10°S , 1°W , which overlies a topographic ridge, is little changed from the free-air to the isostatic map. The central Ross Sea gravity high is relatively unchanged by the isostatic correction.

Since the three principal negative-isostatic-anomaly trends are approximately parallel to each other and to the troughs and ridges in the ocean bottom topography, are directly associated with topographic troughs at least along the grounding line, and are of about the same magnitude, it appears likely that the three arise from the same geologic cause. Likely causes are (1) thick sequences of low-density sediments in the areas of negative anomalies or (2) infolding or downdropping of metasediments and/or felsic intrusives of upper crustal density into the lower crust.

An uncompensated, 1-km-thick, flat slab of glacial-marine sediments with a density of 2.0 Mg m^{-3} sitting in continental crust ($\rho = 2.67 \text{ Mg m}^{-3}$) produces a gravity anomaly of -28 mGal , about the right magnitude to account for the three observed negative anomalies. At J9DC and RI, both of which have an isostatic anomaly of -35 mGal , the estimated sediment thicknesses are about 1350 m and 850 m [Robertson and Bentley, 1990]. The gravity anomalies there could be reduced to less than 10 mGal by including uncompensated layers of low-density sediments of the proper thicknesses in the model. However, the 500-m difference in sediment thickness between those two stations should lead to an anomaly difference of about 14 mGal . Similarly, the seismic sections at Little America V (grid 11.25°S , 3.62°W) [Crary, 1961b] and I10S (grid 7.05°S , 0.95°W) [Robertson and Bentley, 1990] also contain large but different thicknesses of sediment (1325 m and 750 m, respectively), yet the isostatic anomalies at these sites, -16 mGal and -14 mGal , respectively, are nearly the same. On the other hand, at station C-49 (grid 10.98°S , 3.71°W) the thickness of the sediment layer is the same as at I10S, yet the isostatic anomaly is 14 mGal less. It is likely, in fact, that thick glacial-marine sediment layers underlie most parts of the RIGGS survey area and that the primary source of the isostatic anomalies is deeper. Supporting this conclusion is the fact that negative anomalies do not appear in areas where one would expect sediments to be thick, such as the trench next to the Transantarctic Mountains, the trench south of Crary Ice Rise, and the trough between Roosevelt Island and the Rockefeller Mountains.

From seismic evidence, Robertson and Bentley [1990] suggest that the basement beneath the ice shelf consists of metasedimentary and felsic intrusive rocks. Modeling calculations indicate that an uncompensated 3-km penetration of metasedimentary and felsic intrusive rocks into the lower crust is sufficient to

produce a -30-mGal anomaly. We conclude that the sea bottom topography is tectonically controlled and that the associated isostatic anomalies are associated with crustal faulting. Robertson *et al.* [1982] reached a similar conclusion from an examination of the Bouguer anomalies.

Local Gravity Gradients

General. Where gravity was measured on a strain rosette (Figure 7), a small free-air anomaly map of the rosette area was drawn, from which the direction and magnitude of the gravity increase were estimated (Figure 8; tabulated values are in the appendix). The relative error in anomaly between the points in the

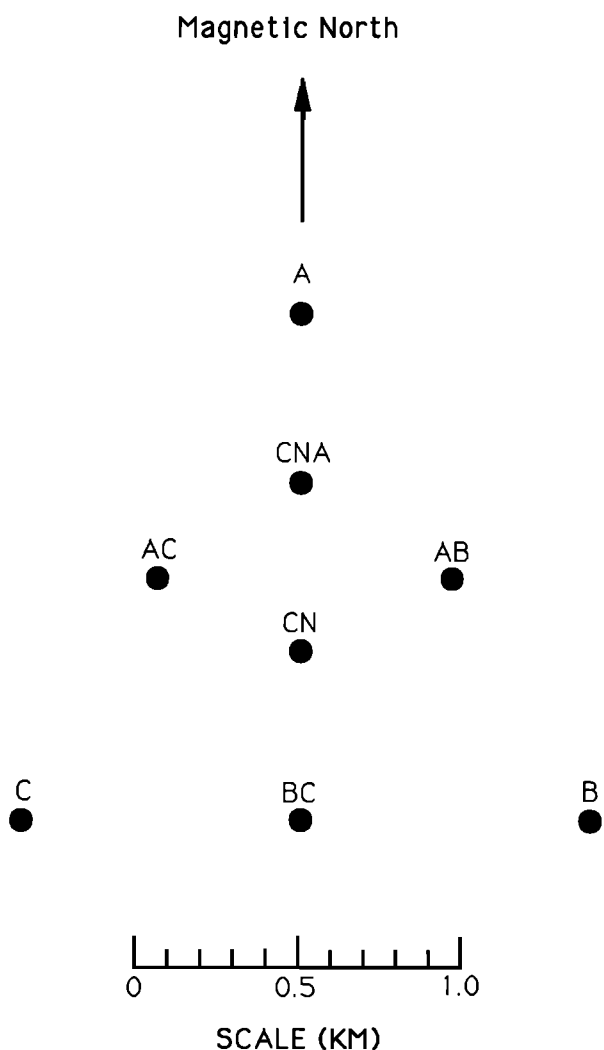


Fig. 7. Layout of a typical strain rosette at a RIGGS station [Thomas *et al.*, 1984].

strain rosettes was taken to be 0.6 mGal, corresponding to an uncertainty in elevation of 2 m, a conservative figure on the flat ice shelf. For eight stations in a rosette, this leads to an estimated error for the gradients of $\pm 0.2 \text{ mGal km}^{-1}$ in magnitude and $\pm 20^\circ$ in direction.

Of the 57 gradients measured, 38 (67%) agree in direction (within $\pm 60^\circ$) with the free-air map. Agreement does not depend upon size of the gradients: when only the 40 largest gradients are considered, the agreement rate increases only an insignificant 1%. About one third of local sources would agree in direction ($\pm 60^\circ$) just by coincidence; so we can say generally that about half of the local gradients have principally regional sources.

Regional bathymetric control also is suggested, most strongly in the region around Roosevelt Island, where eight of the nine gradients are in good agreement with both the free-air and the bathymetric maps.

Local gravity anomalies around Roosevelt Island.

The large positive free-air anomaly centered on Roosevelt Island clearly is caused by the several-hundred-meter increase in bottom elevation, as shown by the fact that the feature disappears from the Bouguer anomaly map. In contrast, the large negative free-air anomaly located at the grid southeastern edge of the ice rise is also pronounced on the Bouguer anomaly map. A positive magnetic anomaly of more than 200 γ was also found in this area [Bennett, 1964]. The gravity and magnetic anomalies both can be modeled by a sialic body with a density of 2.6 Mg m^{-3} intruding 5 km into the high-density subbasement [Bennett, 1964]. Bennett [1964] also calculated that the difference in Bouguer anomalies between Roosevelt Island and the center of the negative anomaly could be explained by a sediment thinning of 1.2 km or by a reduction in the vertical extent of the intrusion under Roosevelt Island. A similar, possibly connected intrusion is the likely source of the lesser but still pronounced free-air and Bouguer anomaly lows grid south by west of Roosevelt Island.

MODELING OF LOCAL GRAVITY ANOMALIES

The local gravity fields around station J9DC and the four RIGGS base camps can be taken as a random sampling of short-wavelength fields on the Ross Ice Shelf. In fact, strong anomaly gradients are present in all five of those local fields. To obtain a quantitative measure of the significance of those anomalies, we have calculated models that could explain each of them. Because there is insufficient control on various parameters, the models must be considered as representative rather than definitive. They show the types and magnitude of structures that must be called upon to produce the observed anomalies (see "discussion of local gravity models").

Gravity Modeling Programs

Computer programs were used to compute the gravitational effects of two- and three-dimensional bodies. Two-dimensional models were computed using the method of *Talwani et al.* [1959]. The computer program, POLYGON V, was originally written by A. G. Smith of Princeton University and later revised by E. Higgins, J. D. Robertson, and the authors in order to meet changing requirements. Three-dimensional models were computed by a program using the algorithm of *Talwani and Ewing* [1960] that approximates the gravitational effect of source bodies by numerical integration of polygonal laminae approximating the shape of the body. The computer program implementing the Talwani-Ewing algorithm is called THREED and was supplied by J. D. Robertson.

Local Gravity Modeling

Two-dimensional models of the local free-air anomaly fields at J9DC and the four RIGGS base camps were calculated. The free-air anomaly fields at BC and J9DC are particularly close to being two dimensional. At Q13, two dimensionality must be assumed, since the areal extent of gravity measurements is insufficient to define a three-dimensional pattern. Both two- and three-dimensional modeling was done at C-16, where areal coverage is good and two dimensionality is not a good approximation.

All local gravity models incorporated three layers: water (with a density of 1.03 Mg m^{-3}), sediment (2.0 Mg m^{-3}), and "basement" (2.7 Mg m^{-3}), lying upon a "subbasement" of density 3.0 Mg m^{-3} . This choice of layers was based principally on the seismic measurements of *Crary* [1961b] at Little America Station. Variations in water depth can potentially produce the largest gravitational effects because of the large density contrast at the seafloor. The water depth is poorly known near BC, RI, Q13 and J9DC, although the sediment thickness is approximately known from seismic long-refraction profiles. Conversely, at C-16, where the water depth is well known, the sediment thickness is not known. Additional information about the thickness of these layers can be inferred from models of the local gravity anomalies at these base camps.

Base camp BC (grid 7.2°S , 1.8°W). Profiles were completed along two lines. One line, 28 km long, lay on the magnetic north-south line that connects BC with J9; the second line was 24 km long perpendicular to the first. The magnetic north-south profile (Figure 9) looks like the classic example of a gravity anomaly caused by a nearly vertical fault. Its half width is 2.4 km, which implies a depth of 2.4 km to the center of the throw of the fault. For modeling, we assumed that

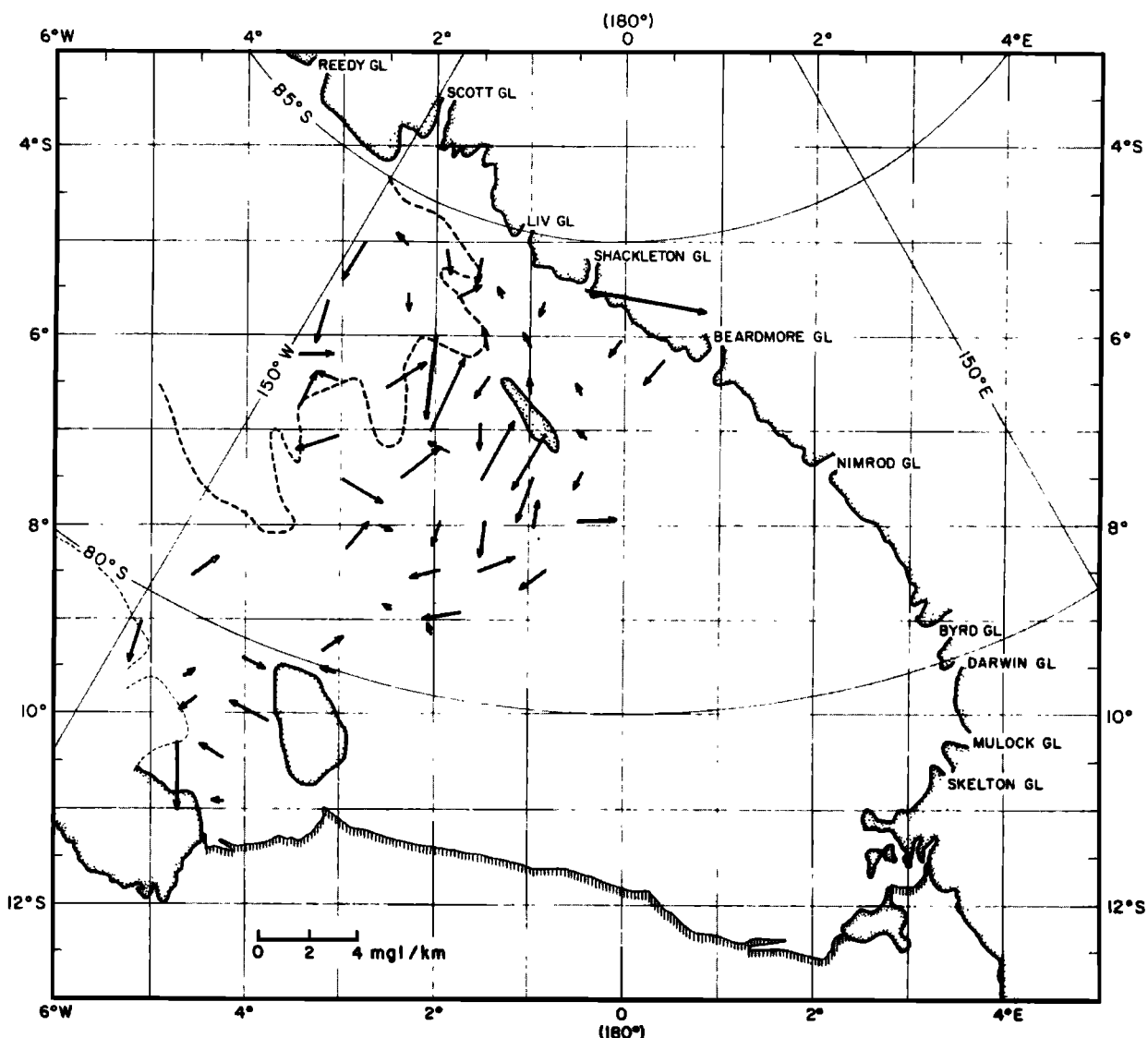


Fig. 8. Map of the Ross Ice Shelf showing the magnitude and direction of the local gravity gradients at RIGGS stations. The gradient scale is near the bottom of the figure.

the ice and water were infinite flat slabs (a discussion of why changes in water layer thickness are inadequate to explain the observed gravity gradients can be found in the section "base camp Q13"), with thicknesses as measured near camp. Two dimensionality is a good approximation here, as shown by the relatively small changes in anomaly on the cross profile (Figure 10). Assuming first a vertical fault, a model was found for which the calculated gravity agreed very well with the observed anomaly (Figure 9). Two additional models were calculated to determine the effect of thickening or thinning the sediment layer by 0.5 km. The slopes for those models were significantly

different from the observed slope, and the root-mean-square residuals increase from 0.20 mGal to 0.31 mGal and 0.49 mGal, respectively, which suggests that a depth estimate of 2.4 km for a vertical fault is accurate to within a few hundred meters. The best model has a sediment thickness ranging from 1.5 to 2.2 km (Figure 9), a range that includes the lower bound sediment thickness of 1.9 ± 0.4 km estimated by Robertson and Bentley [1990] for a seismic refraction path between BC and 20 km on the same line. The average thickness from the gravity model beneath the seismic shot and receiving points is 1.85 km. This agreement provides good support for

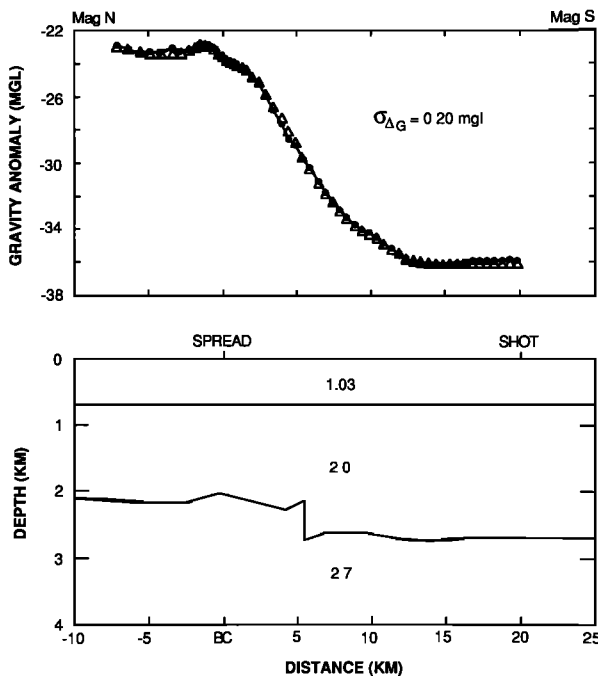


Fig. 9. (Top) Gravity profile and (bottom) modeled density structure along a magnetic north-south line at base camp BC. Dots indicate the observed free-air anomalies, and the triangles represent the modeled values. The standard deviation of the fit between the two is indicated by σ , in the top diagram in megagrams per cubic meters. Densities assumed for the modeling are shown in the bottom diagram, as are the locations of a seismic long-refraction shot and recording spread. Distances are measured from BC.

Robertson and Bentley's [1990] attribution of failure to record seismic arrivals through the bed to travel time delay by thick sediments.

Station J9DC (grid 7.5°S, 1.5°W). Local gravity observations at station J9DC (grid 7.5°S, 1.5°W) were made on a $2 \times 5 \text{ km}$ grid established for radar profiling (Figure 11). The center line, line P, was extended an additional 5 km to the grid northwest (magnetic north), and lines P and B both were

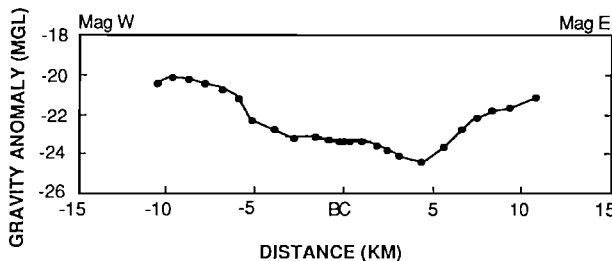


Fig. 10. Profile of free-air anomalies along a magnetic east-west line at base camp BC. Distances are measured from BC.

extended 5 km to the grid southeast (magnetic south). The free-air gravity map at J9DC (Figure 12) shows a steep anomaly increase to the grid northeast (9 mGal in less than 5 km). This gradient, where it is steepest (along the profile line indicated in Figure 12), can be modeled by a vertical step at the sediment-basement boundary 1.2 km grid northeast of J9DC (Figure 13). Also incorporated in the model is a 1° slope of the sea bottom toward the grid northeast. The top of the step was put 600 m below the seafloor to match the indicated sediment thickness found from refraction shooting at station I10S, 78 km grid northeast of J9 [Robertson and Bentley, 1990]. The thickness of the sediment over the bottom of the step, modeled at 1100 m, is essentially uncontrolled. The seismic refraction estimate of sediment thickness is $1700 \pm 300 \text{ m}$ [Robertson and Bentley, 1990]; this figure represents the average of thicknesses beneath J9DC and the seismic recording spread some 21 km to the grid northwest, i.e., only 1 or 2 km from the shot point on the BC refraction profile, where the modeled sediment thickness is 2000 m (Figure 9). That implies a sediment thickness beneath J9DC of $\sim 1400 \text{ m}$, which is compatible with the gravity model. There is, of course, the possibility that the locally steep gravity gradient reflects influences other than a simple fault, such as a three-dimensional effect (suggested by the curvature of the contours in Figure 12) or enhancement by deeper structures, but the necessity for a fault of some kind seems clear.

Base camp RI (grid 9.3°S, 3.1°W). Profiles were completed along two lines. One line, 32 km long, lay on a magnetic north-south line (azimuth 131° grid); the second line was 20 km long running magnetic east-west. Here the gravity anomaly pattern is decidedly not two dimensional. However, the magnetic

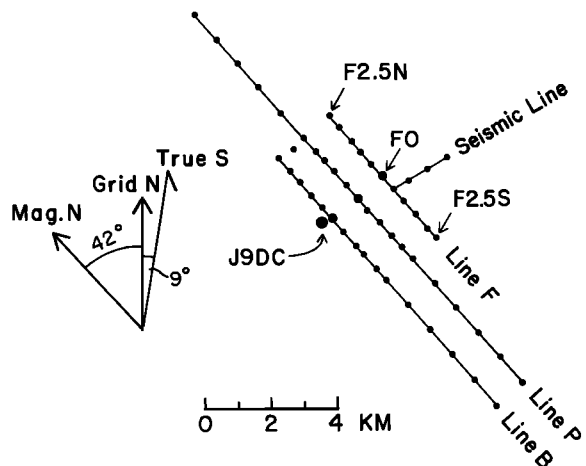


Fig. 11. Diagram of the local gravity survey net near base camp J9DC. Dots denote gravity reading sites.

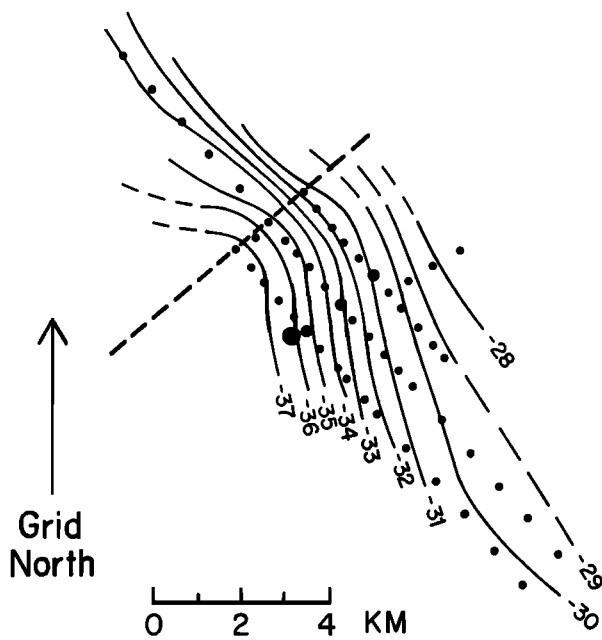


Fig. 12. Contour map of free-air anomalies near base camp J9DC. Dots denote gravity reading sites. The profile shown in Figure 13 is along the dashed line.

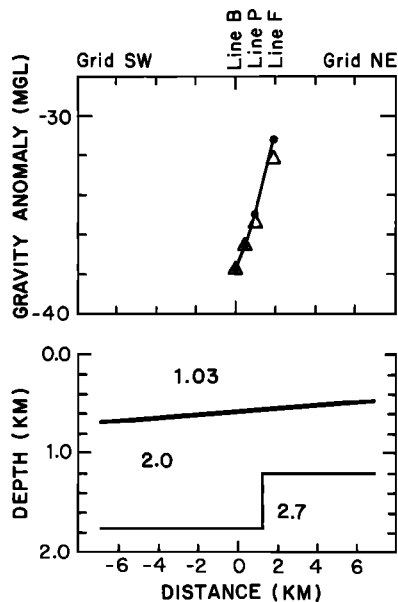


Fig. 13. (Top) Free-air anomaly profile and (bottom) modeled density structure near J9DC. Dots indicate the observed free-air anomalies, and triangles denote the modeled values. Locations of the survey lines shown in Figure 11 are indicated at the top of the diagram. Densities assumed for the modeling are shown in megagrams per cubic meter in the lower diagram. Distances are measured from line B.

north-south profile (Figure 14) can be fit to the first approximation by a simple linear slope; so we will assume that to arise from a sloping seafloor or sediment/basement interface and use two-dimensional modeling for the magnetic east-west profile (Figure 15). To get an estimate of the sediment thickness, the steepest portion of the profile, from -2.0 to 6.0 km, was assumed to reflect a vertical fault, and the half-width method was used to calculate a depth to the middle of the fault of 1.1 km and a throw of 0.3 km.

Again we assumed that the ice and water were infinite flat slabs, and we took their thicknesses to be as those measured near RI, but then the modeled sediment pinched out entirely before the west end of the profile. Moving the fault to a depth of approximately 1.3 km led to a model (Figure 15) that leaves some sediment at -10.0 km and still agrees very well with the observed anomaly.

The magnetic north-south profile suggests a thickening of the sediments and/or an increasing depth of water toward the magnetic north (grid northwest). Regionally, the seafloor shoals to the magnetic northeast (grid north) (Figure 5); so thickening sediments are the more likely cause. How much thickening is difficult to model because considerable isostatic compensation is likely on this scale. Qualitatively, our interpretation agrees with the increasing thickness of sediments inferred by *Robertson and Bentley* [1990]. Taken together, the gravity and seismic profiles indicate, surprisingly, a thinning of sediments going into the trough grid south of station RI.

Robertson and Bentley's [1990] refraction profile was made along the magnetic north-south gravity profile, with the shot at -24 km and receiving spreads at 0, 2, and 4 km. The sediment thickness obtained at 0 km from the gravity model is 0.71 km, which agrees well with *Robertson and Bentley's* [1990] mean thickness of 0.75 km and thickness at 0 km (24 km in their Figure 30) of 0.7 km.

Base camp Q13 (grid 11.0°S, 0.0°E). A total of 95 km of gravity profiling with station spacings of 1–2 km was done near base camp Q13 during the RIGGS III and IV field seasons. Figure 16 shows station locations. The longest gravity profile, line D, runs 46 km grid east-west through Q13 and is coincident grid west of Q13 with the RIGGS IV seismic long-refraction profile. Another long gravity profile, line A, runs through Q13 about 8° east of magnetic north-south coincident to the magnetic south with the RIGGS III seismic long-refraction line. Shorter gravity profiles are along line B, which extends magnetic east 7.6 km, and line C, which runs 11.0 km nearly along magnetic west. Additional data come from Ross Ice Shelf Traverse (RIST) stations [*Crary et al.*, 1962].

Figure 17 shows the free-air anomaly map of the Q13 area. Anomalies range from a high of +13.2

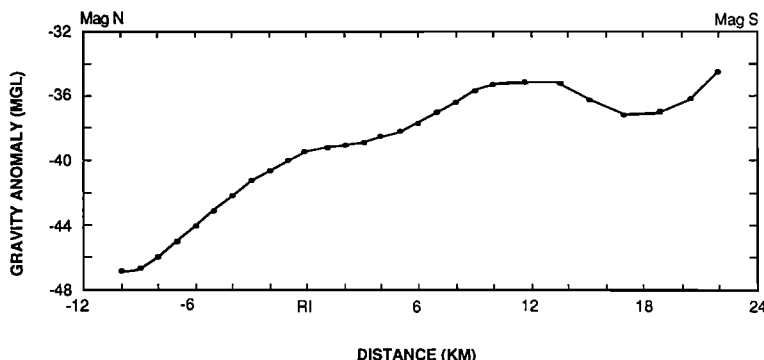


Fig. 14. Free-air anomaly profile along the magnetic north-south line near base camp RI. Distances are measured from RI.

mGal at the grid southeast end of line A to a low of -45.0 mGal approximately 21 km grid west of Q13. A local high of -20 mGal lies approximately 6 km grid east-southeast of Q13. The gravity gradient of approximately 3.5 mGal/km at the grid southeast end of line A is remarkable. Of the 57 gravity gradient measurements for RIGGS stations in the grid western portion of the Ross Ice Shelf, only two are as large as this value: one measurement (station F10; gradient 5 mGal km^{-1}) on Shackleton Glacier adjacent to the Transantarctic Mountains and one measurement (station G7; 3.5 mGal km^{-1}) near the Siple Coast grounding line. The locations of those two large gravity gradients suggest that they may be due to changes in bottom depths. Unfortunately, bottom depth control in the vicinity of Q13 is limited to three seismic reflection determinations: 732 m at Q13, 795 m at 9 km grid west of Q13, and 823 m at RIST station C-8.0 (Figure 16), approximately 14 km grid north-northeast of Q13.

The two seismic refraction profiles provide an indication of sediment layer thickness, although they are somewhat contradictory. These unreversed, one-shot profiles each involved two recording locations (Figure 16), at each of which there was a spread of 12 geophones. Signals were recorded in parallel with different gains on oscillograph channels 1-12 and 13-24. Seismograms from the shot at the end of line A (376 kg in a 15-m hole) are shown in Figure 18. The upper seismogram, recorded on a Texas Instruments model 7000B seismic system, shows fairly good arrivals on six of the twelve traces. Unfortunately, there are no timing lines on the record; a subsequent record with timing lines was used to give a time scale. The lower seismogram, recorded on a Southwest Industrial Electronics (SIE) seismic system, has only weak arrivals of uncertain onset time.

For the refraction recording along line D the charge was 475 kg of explosives located in a 100-m hole at Q13. Receiving spreads were located at 9.1 km and

30.7 km from the shot point (the former, too close to the shot point to record refracted energy from the seabed, was placed there in the unrealized hope of recording a Moho reflection). The seismogram recorded at 30.7 km (Figure 19) shows two different refracted arrivals with apparent velocities of 5.7 ± 0.3 km s^{-1} and 7.8 ± 0.2 km s^{-1} , respectively.

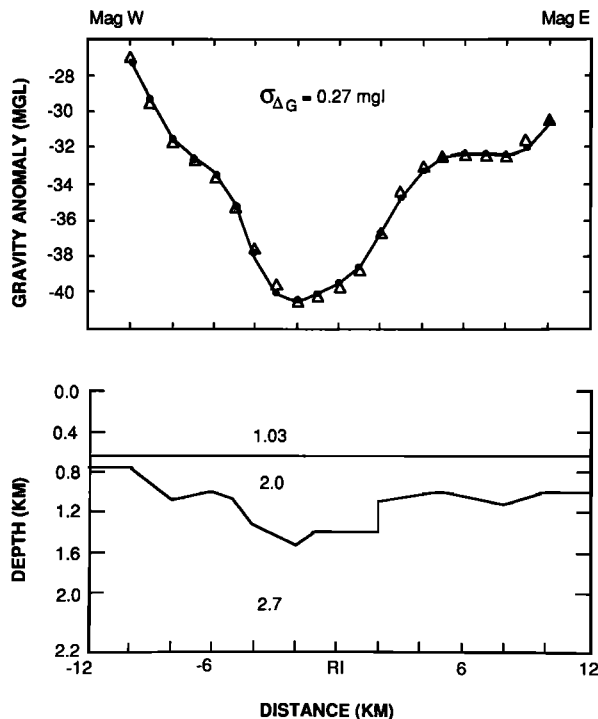


Fig. 15. (Top) Free-air anomaly profile and (bottom) density model along the magnetic east-west line near base camp RI. Observed values are denoted by circles, and modeled values are indicated by triangles; $\sigma_{\Delta G}$ is the standard deviation of the fit. Densities are given in megagrams per cubic meter. distances are measured from RI.

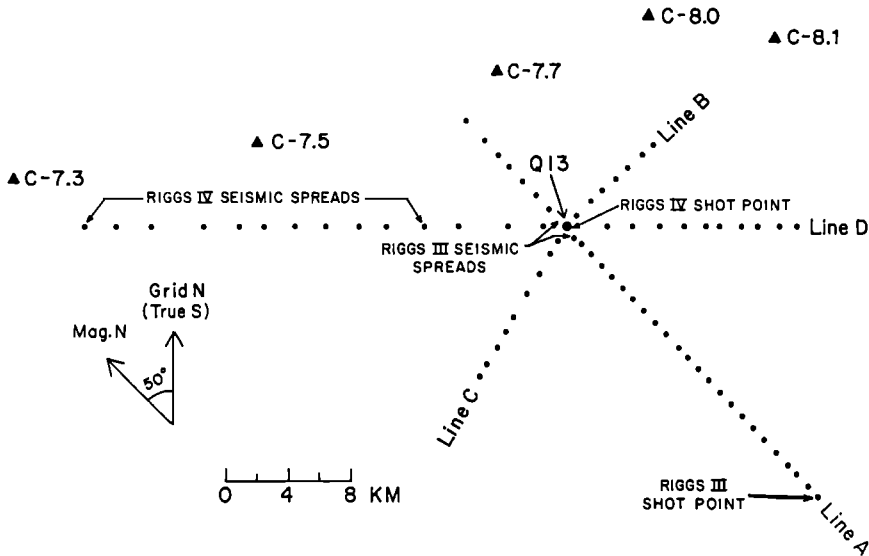


Fig. 16. Diagram of gravity sites, seismic shot points, and seismic spreads near base camp Q13. Circles mark RIGGS sites; triangles denote stations from the International Geophysical Year (IGY) survey of Crary *et al* [1962].

On the travel time plot for line A (Figure 20) a line between the arrivals from the two records yields an apparent velocity, 5.4 km s^{-1} , that agrees with that from the first peaks on record 7000B. If we use 5.4 km s^{-1} for v_4 , the wave speed in the seismic basement, wave speeds of $v_1 = 3.51 \text{ km s}^{-1}$ (vertical average), $v_2 = 1.44 \text{ km s}^{-1}$, and $v_3 = 2.4 \text{ km s}^{-1}$ in ice, seawater, and sediment, respectively, and the thicknesses of the ice and water layers, 328 m and 445 m, respectively, given by Albert and Bentley [1990] for Q13, we calculate a sediment layer thickness of 110 m. However, the strong free-air gravity gradient between the two recording spreads (-1 km to $+1 \text{ km}$ in Figure 22) suggests slopes (according to the model shown in Figure 22) on the seafloor and the sediment-basement contact of about 0.5° and 1° , respectively. These slopes would cause the apparent velocity to be too

small by about 0.3 km s^{-1} , which would imply that $v_4 \approx 5.7 \text{ km s}^{-1}$. That, in turn, leads to a sediment thickness of $\sim 370 \text{ m}$ that is increased further to $\sim 400 \text{ m}$ if the seafloor is shallower under the shot point than beneath Q13, as is implied by the gravity-derived map of seafloor topography (Figure 24).

This large sediment thickness is difficult to reconcile with the travel times for the earlier of the two arrivals along line D (Figure 21), which imply a minimum velocity of 5.6 km s^{-1} (taking the seafloor topography of Figure 24 into account) for no sediments at all. To accommodate 400 m of sediments would require that $v_4 \approx 6.0 \text{ km s}^{-1}$. This value not only does not agree with v_4 on line A, but is substantially higher than wave speeds generally found in the seismic basement in the Ross embayment: $5.5\text{--}5.7 \text{ km s}^{-1}$ beneath the ice shelf [Robertson and Bentley,

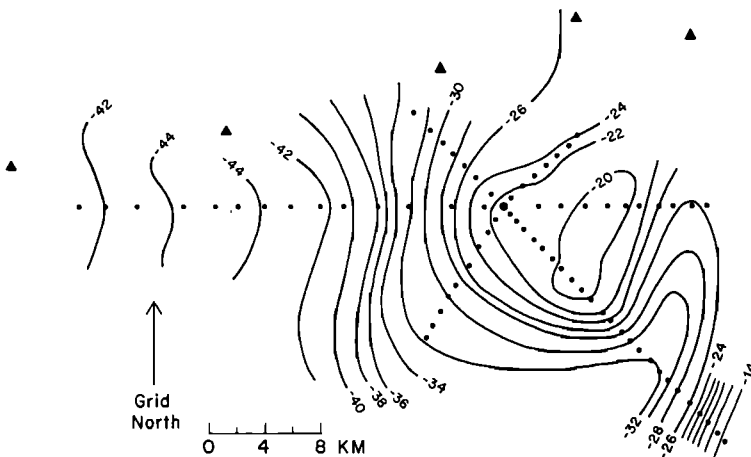
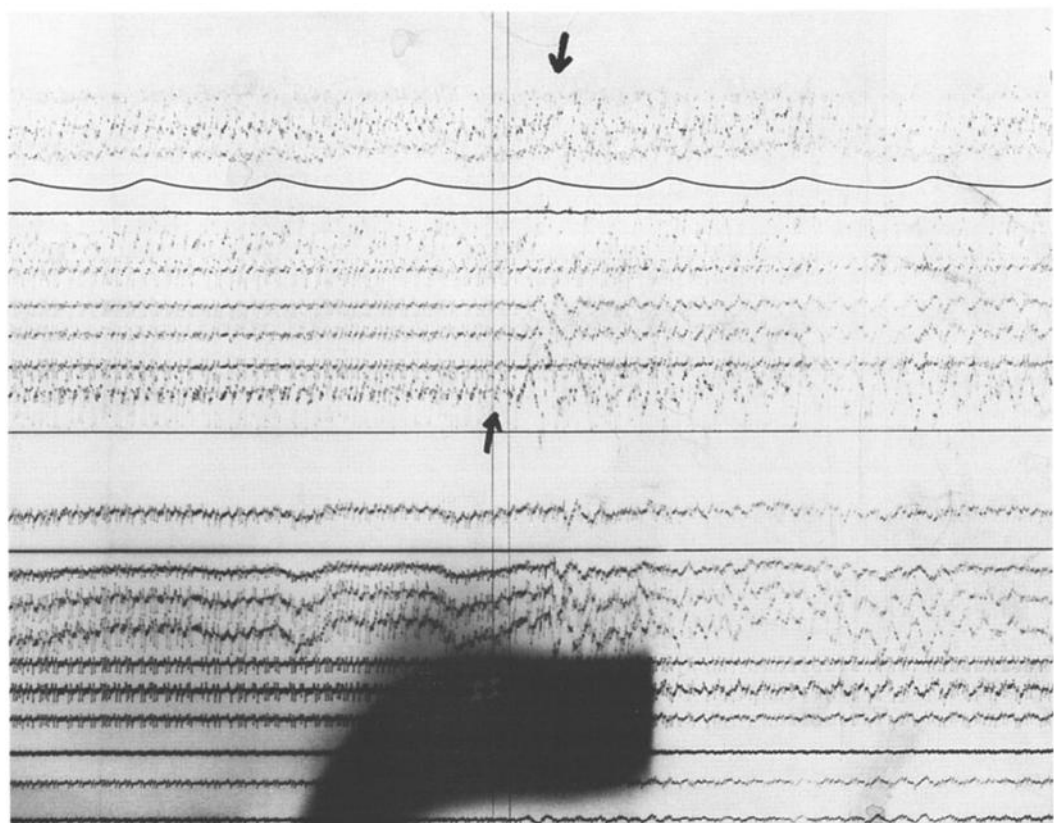
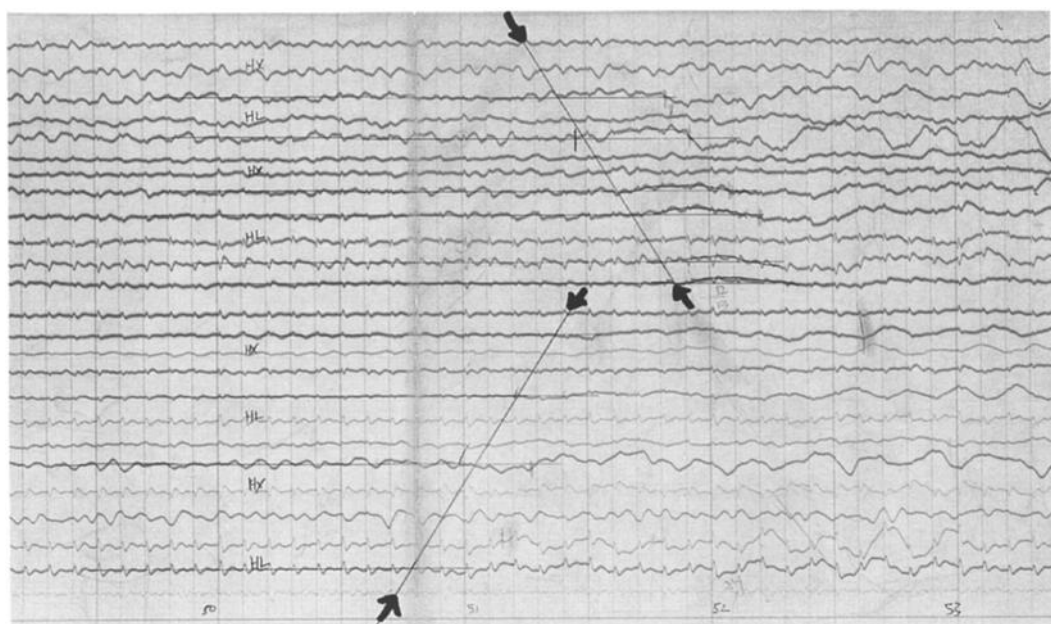


Fig. 17. Map of free-air anomalies near base camp Q13. The contour interval is 2 mGal.



a.



b.

Fig. 18 Portions of seismograms from the long-refraction shot (376 kg in a 15-m hole) on line A recorded near base camp Q13, showing arrivals through seismic basement (arrows). (a) Record 7000 B, recorded 23.4 km from the shot on a spread of 12 geophones 30 m apart recorded at different gain, on traces 1-12 and 13-24. Horizontal motion recorded on traces 7 and 19 (longitudinal) and 3, 10, 15, and 22 (transverse); vertical motion on all other traces. (b) Record 355 recorded 24.7 km from the shot on a spread of 12 geophones 30 m apart, recorded at different gain on traces 1-12 and 13-24. Horizontal motion recorded on traces 4, 10, 18, and 24 (longitudinal) and 2, 7, 15, and 21 (transverse); vertical motion on all other traces.

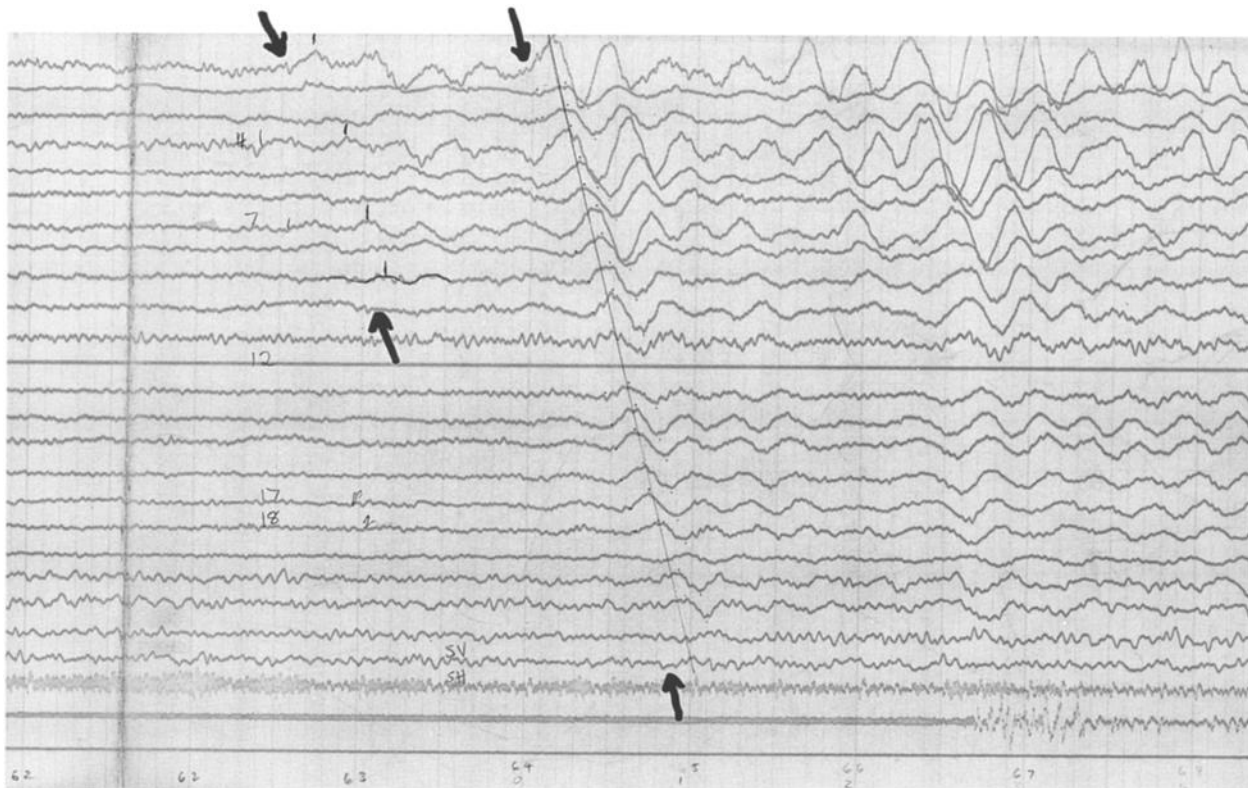


Fig. 19. Portion of the seismogram from the long-refraction shot (475 kg in a 100-m hole) on line D recorded near base camp Q13, showing arrivals through seismic basement, and through a deeper layer (two pairs of arrows). The spread comprised 24 geophones 30 m apart 30.7 km from the shot. Horizontal motion was recorded on traces 23 (longitudinal) and 24 (transverse); vertical motion on all other traces.

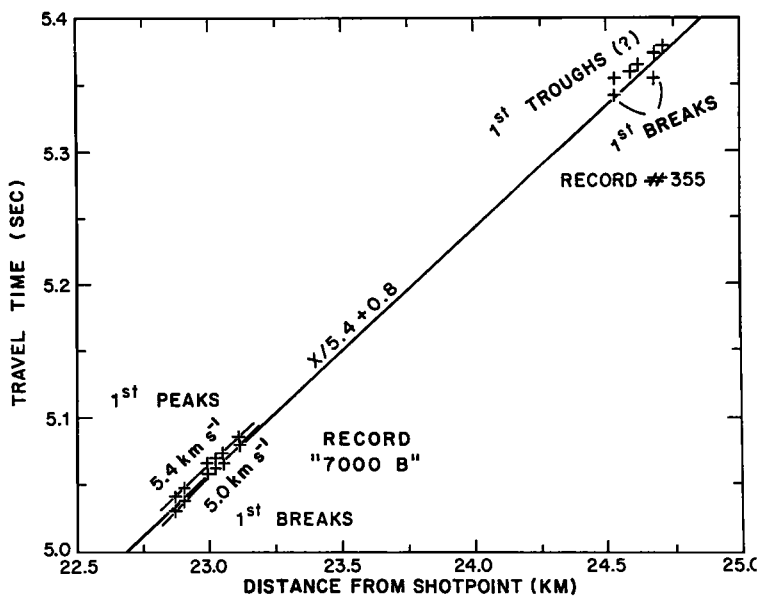


Fig. 20. Travel times from the long-refraction shot on line A recorded near base camp Q13. Apparent velocities from first breaks and first peaks on record "7000B" and a travel time equation for the line between records are shown.

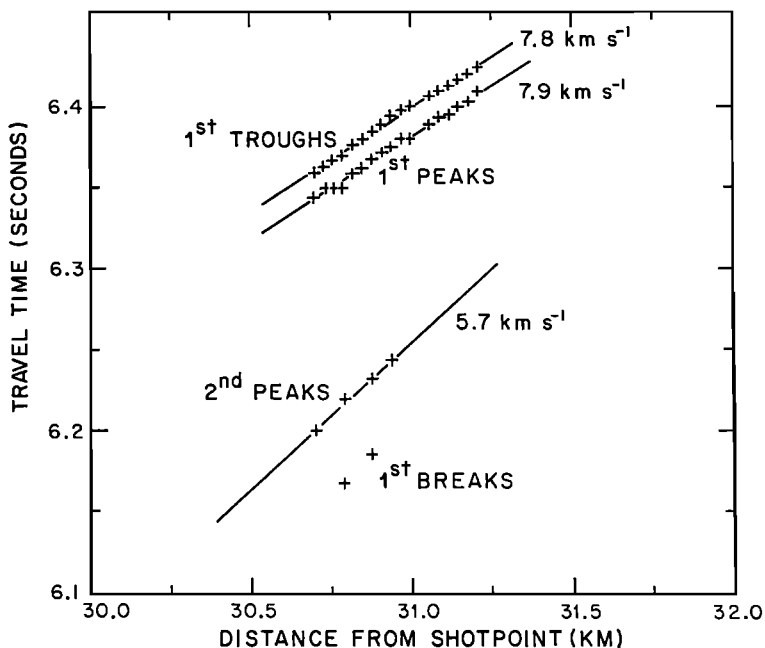


Fig. 21. Travel times from the long-refraction shot on line D recorded near base camp Q13. Apparent velocities for second peaks on the basement arrival and first peaks and troughs on the subbasement arrival are shown.

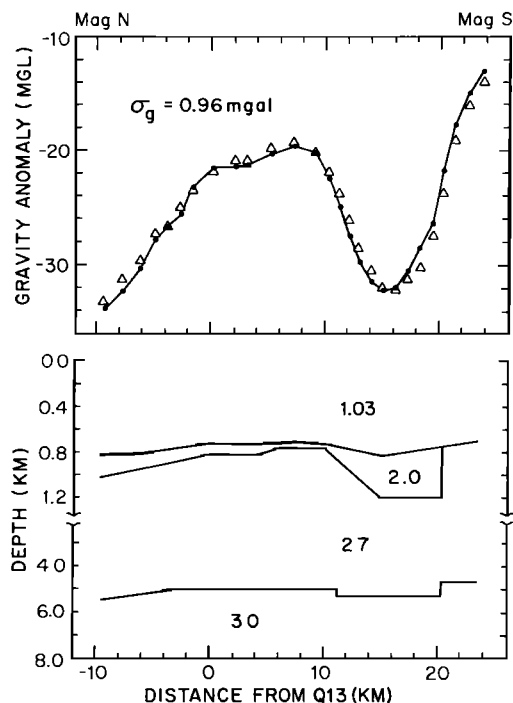


Fig. 22. (Top) Free-air anomaly profile and (bottom) density model along line A near base camp Q13. Observed values are denoted by circles, and modeled values are indicated by triangles; σ_g is the standard deviation of the fit. Densities are given in megagrams per cubic meter. Distances are measured from Q13.

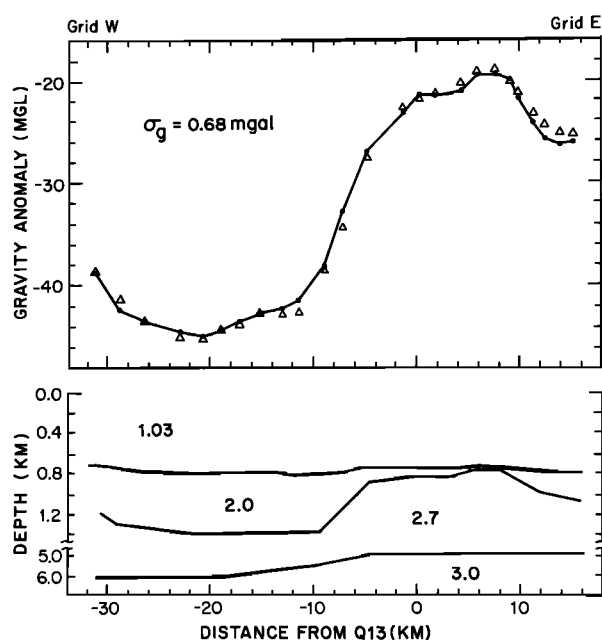


Fig. 23. (Top) Free-air anomaly profile and (bottom) density model along line D near base camp Q13. Observed values are denoted by circles, and modeled values are indicated by triangles; σ_g is the standard deviation of the fit. Densities are given in megagrams per cubic meter. Distances are measured from Q13.

1990] and an average 5.5 km s^{-1} in the Ross Sea [Houtz and Davey, 1973]. We conclude that in fact $v_4 \approx 5.7 \text{ km s}^{-1}$ and that the sediment thickness is highly variable. This variability also shows in the gravity models (Figures 22 and 23). The sketchy nature of the seismic evidence and the various sources of uncertainty in interpretation (absence of timing lines on record 7000B, weak arrivals on record 355, uncertain water depths) preclude more definite conclusions about thicknesses of sediments.

The strong secondary arrival along line D (Figure 19) shows an extremely high apparent wave speed (Figure 21) that cannot reasonably be the true wave speed, v_5 , in the deeper crustal layer. Crary [1961b] found $v_5 = 6.4 \text{ km s}^{-1}$ from a reversed profile near Little America. Several of the sonobuoy profiles in the Ross Sea discussed by Cooper *et al.* [1987] show wave speeds of around 6.4 km s^{-1} ; several others show wave speeds of around 7.4 km s^{-1} . Assuming successively that $v_5 = 6.4 \text{ km s}^{-1}$ and 7.4 km s^{-1} and that the sedimentary layer is thin leads to depths below the seafloor to the high-speed layer of 4.5 and 6 km, respectively.

Free-air anomalies along line A were fitted with a model (Figure 22) that consists of the seawater layer ($\rho_w = 1.03 \text{ Mg m}^{-3}$) and three rock layers with densities of 2.0, 2.7, and 3.0 Mg m^{-3} . The root-mean-square residual for this model of line A is 1.0 mGal. The modeled ocean bottom along line A passes through the measured depth of 732 m at Q13 and follows the trends established by the regional bathymetry with bottom slopes that never exceed 1° . Although bottom depth control along this line consists only of the single value at Q13, it appears likely from the modeling calculations that bottom depth variation can account for no more than approximately 50% of the gravity variation, since a larger contribution would imply excessively large sea bottom slopes. For example, a seafloor slope of almost 6° would be required at 20 km magnetic south to model the 4.3 mGal km^{-1} gravity gradient that occurs there. For comparison, only 7 of the 46 seismically estimated local seafloor dips reported by Crary *et al.* [1962] and none of the 9 reported by Robertson and Bentley [1990] are greater than 1° . Hayes and Davey [1975] report maximum sea bottom slopes of 1.6° for the Ross Sea from bathymetric profiling. Although one of the largest local sea bottom slopes reported by Crary *et al.* [1962], 6.5° over a distance of about 0.2 km, is near Q13 at RIST station C-8.0 (Figure 16), it is highly unlikely that a large dip would extend over distances of several kilometers in light of the generally smooth character of the observed bathymetry in the Ross embayment. A 6° bottom slope over 6 km would correspond to a 600-m change in ocean depth. Such a depth change would require the existence near

Q13 of an ocean deep comparable to Discovery Deep. A change in sediment thickness combined with limited variations in ocean depth appears to be a much more likely way to explain the gravity change at the south end of line A. Assuming a minimal seafloor slope between 15 and 21 km leads to a model with a nearly vertical fault truncating the sediments at 20.4 km (Figure 22). (Deeper structure is shown in the model but is not essential.)

The gravity model for line D is shown in Figure 23. As it is modeled, the 25-mGal range in free-air anomaly along the line principally reflects changes in sediment, from a minimum of 35 m at 8 km and east of Q13 to a nearly constant maximum of about 600 m between 10 km and 29 km grid west of Q13. The high-density layer is put at a depth of 5 to 6 km to accord with the seismic refraction results; the slight slope shown is not essential.

The bottom topography in the vicinity of Q13 was contoured (Figure 24) based upon the three seismic depths and the depths estimated from the gravity modeling. This local coverage suggests that Q13 lies on the grid northwest edge of a localized topographic high trending grid northeast-southwest. The length of this high is not clearly defined by these data or by the regional bathymetry. Its shape may be better defined by the gravity map (Figure 17), which suggests that it is more domelike than ridgelike. The gravity modeling shows that the topographic high reflects a more pronounced high in the subsediment basement.

Base camp C-16 (grid 8.7°S , 14°E). Figure 25 shows the locations of local gravity measurements made at RIGGS base camp C-16. Profile lines EP and DM, each approximately 24 km in length and centered at EP1, were oriented in the true north-south and east-west directions, respectively, whereas line G extends 11 km true southwest from EP1. A gravity reading was taken also at survey point DM107, located 36 km true east of C-16. RIST stations C-15.6, C-16.0, and C-16.1 provide additional isolated data points nearby. Additional gravity measurements were made 0.5 km apart in a $1.5 \times 5.0 \text{ km}$ grid near camp that was used for a radar survey.

Free-air anomaly values around C-16 (Figure 26) show a striking, partially closed low of -52 mGal . From this low, anomalies increase rapidly in all directions except possibly to the grid north, where data are lacking. Regionally, C-16 is located at the grid southeast end of a long linear trend of negative free-air anomalies (Figure 3), which suggests that the anomaly at C-16 may be part of a regional feature. Seismic reflection profiling of ocean depths along lines DM and EP made possible the contouring of the bottom topography near C-16 (Figure 27) and the construction of a Bouguer gravity anomaly map (Figure 28). The Bouguer correction modifies the

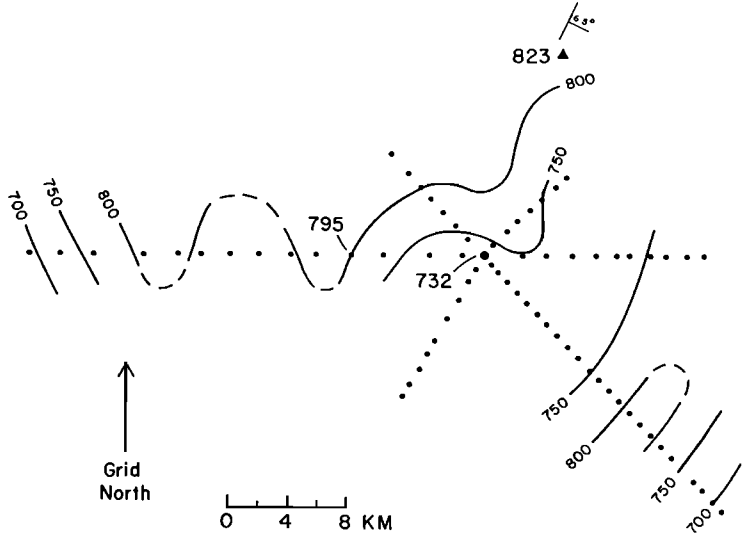


Fig. 24. Map of seafloor depths (meters below sea level) near base camp Q13. The contour interval is 50 m. The seafloor dip symbolized at the top of the figure was measured by Crary *et al.* [1962] from seismic reflections.

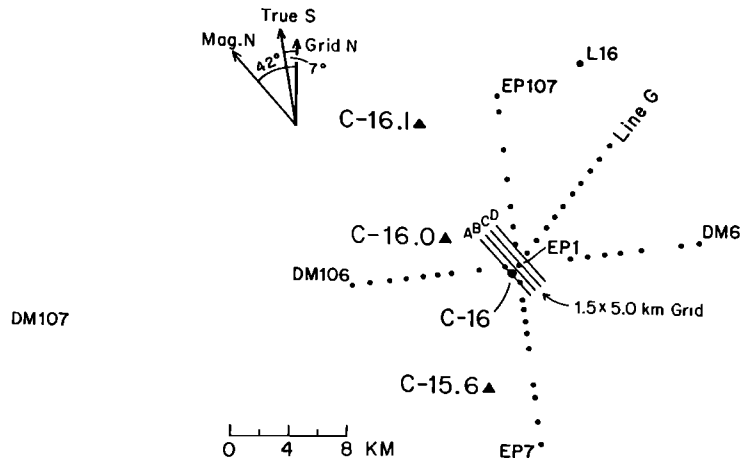


Fig. 25. Diagram of gravity sites near base camp C-16. Circles denote RIGGS sites; triangles denote stations from the IGY survey of Crary *et al.* [1962]. Measurements were made every 0.5 km along lines A, B, C, and D.

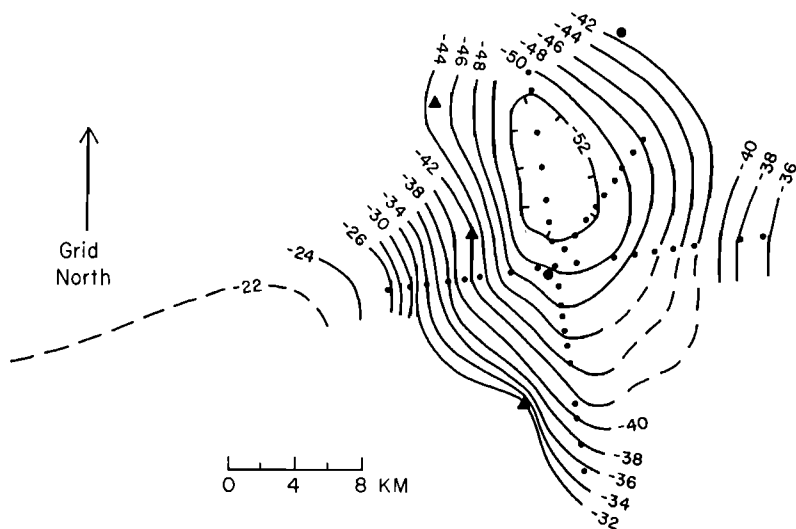


Fig. 26. Map of free-air anomalies near base camp C-16. The contour interval is 2 mGal.

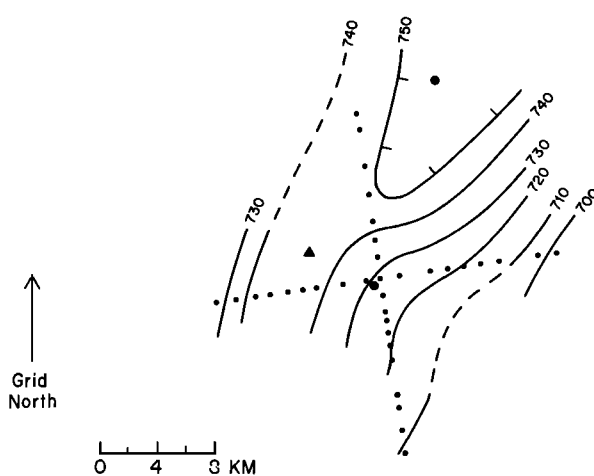


Fig. 27. Map of seafloor depths (meters below sea level) near base camp C-16. The contour interval is 50 m.

character of the free-air gravity map only by changing slightly the gravity gradients to the grid east and west of C-16.

Base camps C-16 and Q13 lie along the same submarine topographic low, which extends from Nimrod Glacier grid south-southwest into the Ross Sea (Figure 5a). The grid northeast-southwest trend of the local bottom topography near C-16 (Figure 27) fits this regional bathymetry well.

Seismograms from a long-refraction shot (295 kg in a 15-m hole) about 23 km grid south of C-16 along line EP are shown in Figure 29. The upper seismogram was recorded on the 7000B seismograph at EP1, 23.7 km from the shot, using a single spread of 12 geophones fed in parallel into channels 1–12 and 13–24. The lower seismogram was recorded on the SIE seismograph 2.6 km true south of EP1, 26.3 km from the shot, using all 24 channels. Both seismograms show good first arrivals on nearly all the traces with vertical geophones. Unfortunately, neither seismogram recorded the shot instant, so only relative travel times for these seismograms can be plotted (Figure 30). Picks of first breaks, first peaks, and first troughs on the 7000B seismograms give apparent velocities of 4.6, 5.4, and 5.0 km s^{-1} , respectively; the average is 5.0 km s^{-1} . Picks of first breaks and first peaks from the SIE seismogram both give apparent velocities of 4.3 km s^{-1} . Figure 31 shows an interpretation of these data in which it is assumed that the true basement velocity is 5.0 km s^{-1} . A 5° dip of the sediment-basement interface beneath the SIE spread is required to match the low apparent velocity observed there. (This section of the bed lies at the grid southern end of the -52-mGal contour in Figure 26.) The thickness of the sediment layer beneath C-16 is undetermined since total travel times were not recorded.

Even though the gravity anomaly is clearly three dimensional, we have fitted several two-dimensional models first for ease in comparing the effects of different structures. Line DM can be modeled entirely in terms of a sedimentary basin that is bounded by vertical faults on both sides (Figures 32 and 33, model a); according to this model, C-16 lies approximately over the center of a graben one side of which, 7 km grid west of C-16, has a throw of 1200 m and the other side of which, 8 km grid east of C-16, has a throw of 750 m. This model gives an estimate of the thickest sediment layer likely to occur at C-16 (2600 m), since the observed gravity gradients could not be produced by more deeply buried faults. Alternatively, the observations can be fitted by more gradual or lesser changes in sediment thickness by the inclusion of deeper structure (Figures 32 and 33, models b–d). It is even possible to fit the observed anomalies without any change in sediment thickness, but only with models that are geologically highly unlikely (for example, Figure 33, model e).

Only one three-dimensional model was fitted to the data. That model (Figure 34) includes a polygonal approximation to the sea bottom contours (Figure 27, solid lines) and a graben on the boundary between layer 3 and layer 4 (heavy dashed lines). A thick layer of low-density sediments in this model (~1750 m) coincides with the gravity low grid north of C-16. Thinning of these sediments to the grid south combined with the effect of approaching the upthrown high-density fault block causes the increasing gravity values at this end of line EP (Figure 35). A similar though smaller effect associated with the fault bounding the grid northeastern side of the graben occurs at the grid northern end of lines EP and G. The details of this model are, of course, subject to the

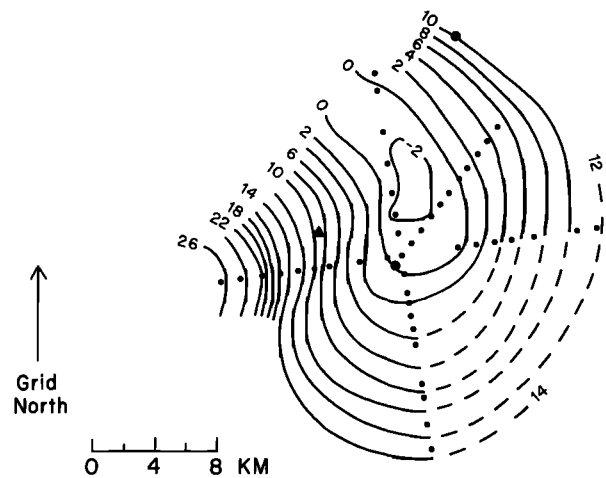


Fig. 28. Map of Bouguer anomalies near base camp C-16. The contour interval is 2 mGal.

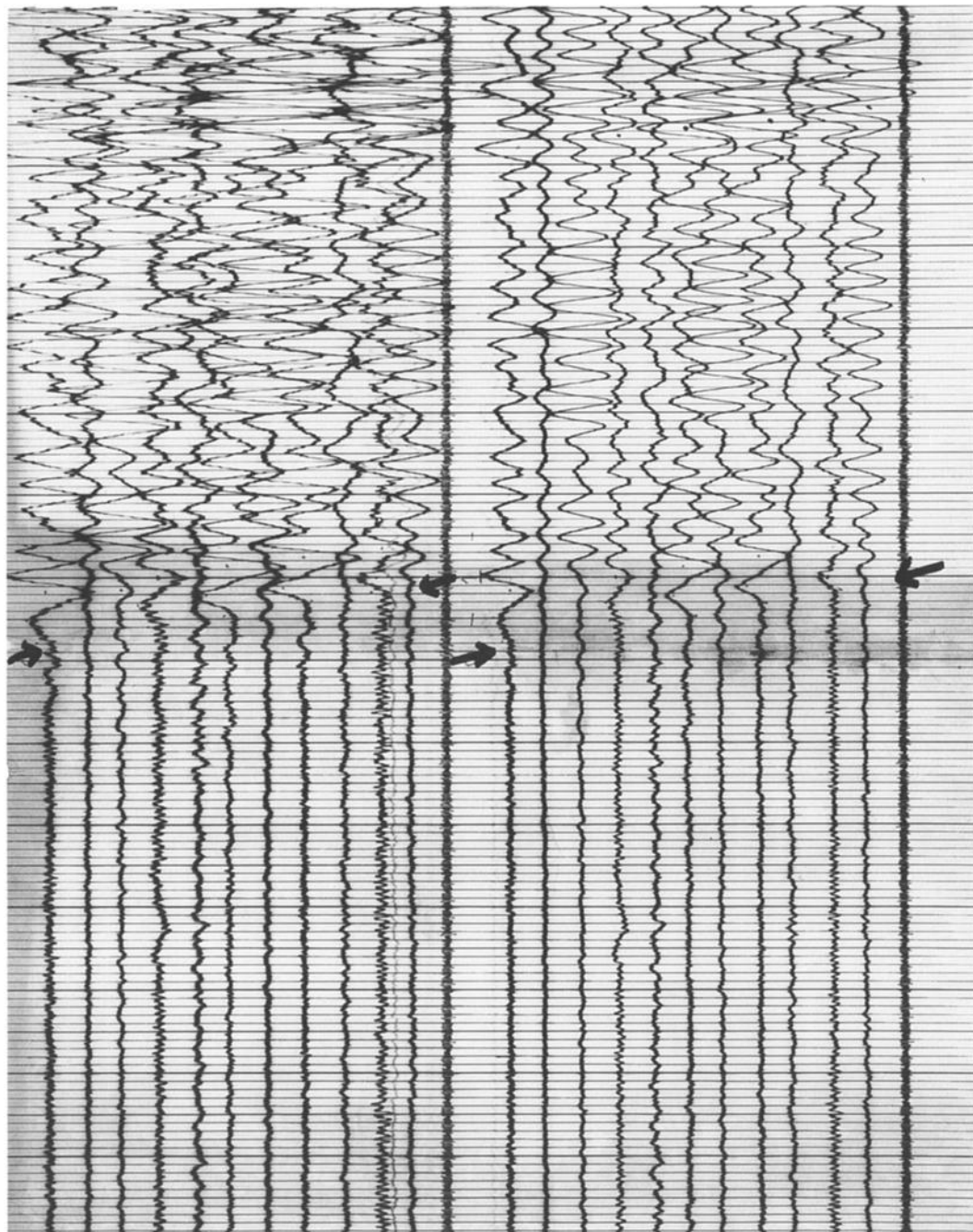


Fig. 29. Portions of seismograms from the long-refraction shot (295 kg in a 15-m hole) recorded near base camp C-16, showing arrivals through seismic basement (arrows). (a) Record 7000B, recorded 23.4 km from the shot on a spread of 12 geophones 30 m apart, recorded at different gain on traces 1-12 and 13-24. Horizontal motion recorded on traces 3, 7, 11, 15, 19, and 23 (longitudinal) and 5, 9, 17, and 21 (transverse); vertical motion on all other traces. (b) Record 174, recorded 26.3 km from the shot on a spread of 24 geophones 30 m apart. Horizontal motion recorded on traces 3, 7, 11, 15, 19, and 23 (longitudinal) and 5, 9, 17, and 21 (transverse); vertical motion on all other traces.

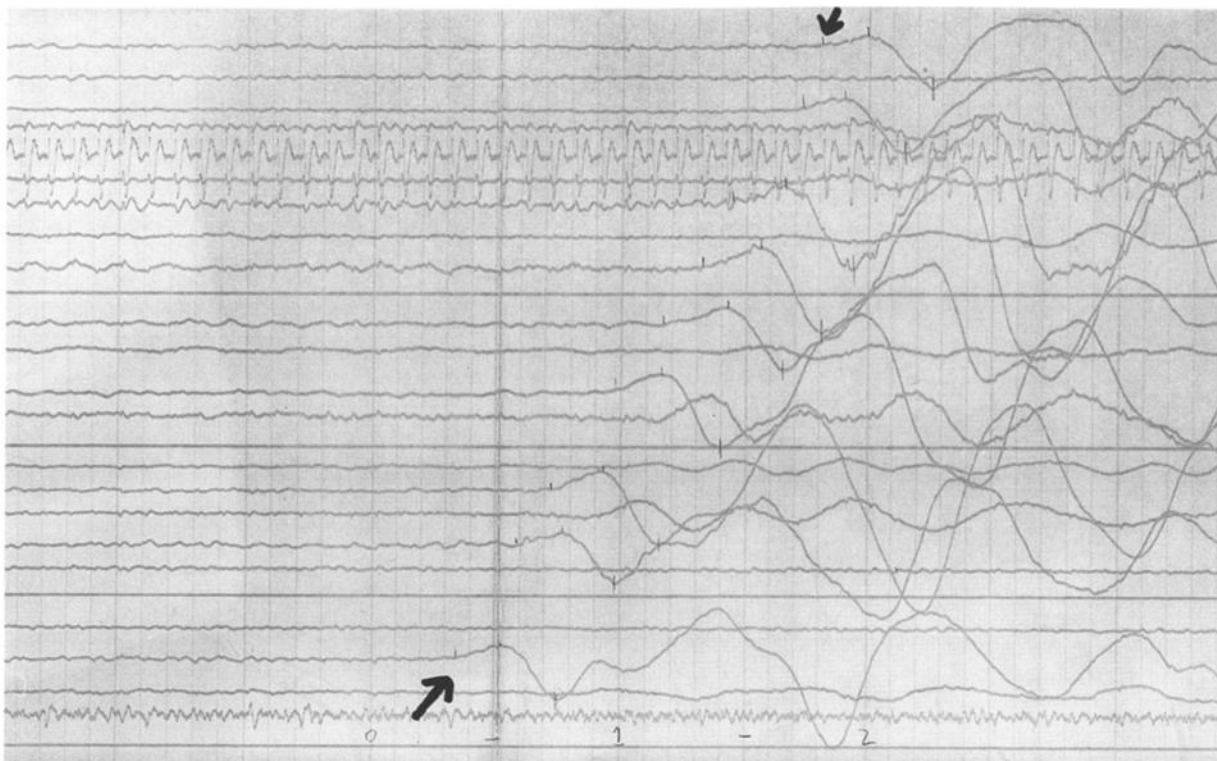


Fig. 29b

same kinds of ambiguities demonstrated by the two-dimensional modeling (Figure 33).

Discussion of Local Gravity Models

The configuration of the low-density sediments at J9DC and Q13 is controlled both by seismic refraction measurements and by the presence of steep gravity gradients that can be satisfactorily modeled only by shallow structure. Restricting sea bottom slopes to 1° or less constrains the gravitational effect of the water

depth to less than half of the total observed variation. At C-16, where the sea bottom is defined seismically, the observed gravity can be modeled satisfactorily by variations in sediment thickness, in basement thickness, or by a combination of the two. However, modeling entirely in terms of the basement/subbasement interface brings the high-density subbasement within 260 m of the seafloor, which is unlikely as no significant magnetic anomalies were observed near C-16 during the Ross Ice Shelf Traverse [Bennett, 1964]. If the basement/subbasement interface is

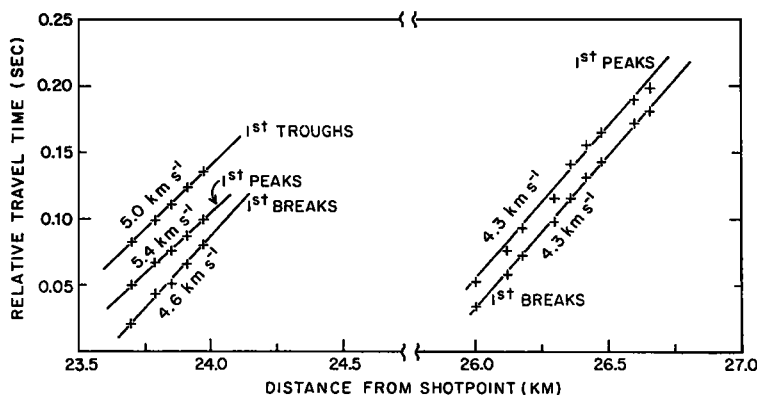


Fig. 30. Relative travel times from the long-refraction shot recorded near base camp C-16. Note the break in the distance scale. Travel times are only relative because no shot instant was recorded.

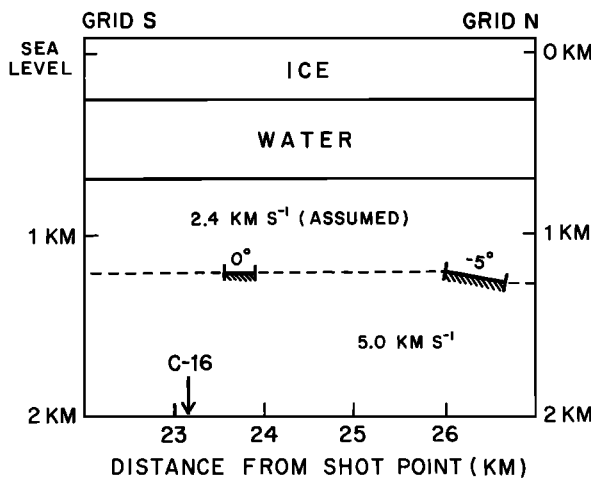


Fig. 31. Seismic section deduced from the travel time plot in Figure 30. Wave speeds in the sediments and the seismic basement and the dips indicated by the cross-spread apparent velocities are shown. The position of C-16 along the line is marked.

everywhere deeper than 5 km, as at Q13, then a decrease in sediment thickness of approximately 900 m to the grid west and 600 m to the grid east is required to fit the observed data. For these intermediate models, the total sediment thickness beneath C-16 can vary from approximately 2.5 km for vertical step changes (vertical faults) to approximately 1 km for gradual changes (slope of $\sim 5^\circ$). The configuration of the basement/subbasement interface is even less constrained, since it is modeled to fit the more "regional" variations of the observed gravity which actually could be due to gradual variations in sediment thickness.

Seismic long-refraction profiles and local gravity observations indicate that the "central high" in the Ross Sea, i.e., the basement ridge that runs along longitude 180° [Davey, 1987], probably extends to the grid north beneath the ice shelf at least as far as Q13. The best fitting two-dimensional gravity model at Q13 includes a vertical fault striking approximately along 030° grid with 450 m of vertical uplift on the grid southeast side.

The sedimentary basin beneath C-16 appears to be related to a regional feature extending grid northwest for several hundred kilometers. More generally, a grid northwest-southeast trend, probably associated with crustal rifting, is, as already discussed, a major feature of the gravity field on the Ross Ice Shelf. The faults modeled at J9DC and RI parallel this trend. However, the fault modeled at BC located only 43 km grid northwest of J9DC strikes approximately normal to this trend; it may be related to a secondary trend, running grid northeast-southwest to the grid northeast of Crary Ice Rise, that is evident in the Bouguer and isostatic gravity anomalies (Figures 4a and 6).

The correspondence of all these local structures to the regional trends in the Ross embayment suggests that they are the result of regional tectonic activity. Furthermore, as the siting of the five stations was not based on any geological knowledge, i.e., was geologically random, the occurrence of pronounced structures at each implies that most of the seafloor beneath the Ross Ice Shelf has been tectonically affected. These facts lend strong support to the concept of the Ross embayment as a zone of rifting [Davey, 1987; Tessensohn and Wörner, 1991; Behrendt et al., 1991].

ANALYSIS OF ISOSTASY IN THE ROSS EMBAYMENT

Spatial Frequency Spectra of Gravity and Bathymetry

Values of gravity and bathymetry were interpolated from the Ross embayment data onto a grid with spacing of 0.5° (55.5 km) extending from grid 5°W to 3.5°E and grid 3°S to 18.5°S (18×32 points). RIGGS stations were planned to be located every 0.5° and were generally placed very close to these grid locations. Over the Ross Sea continental shelf, shipborne coverage is sufficient for good interpolation to these grid points.

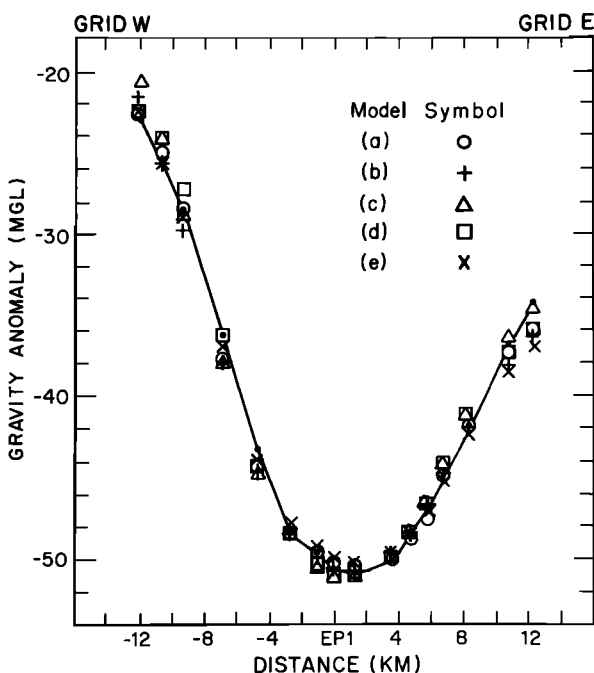


Fig. 32. Free-air anomaly profile along grid east-west line near base camp C-16. Observed values are denoted by solid circles; modeled values refer to the models in Figure 34. Distances are measured from survey point EP1 (Figure 25).

The corners of this rectangular grid extend beyond the edge of the continental shelf to the grid southwest and into the Transantarctic Mountains to the grid northeast. Although some gravity data exist for the Transantarctic Mountains area, no data cover the Ross

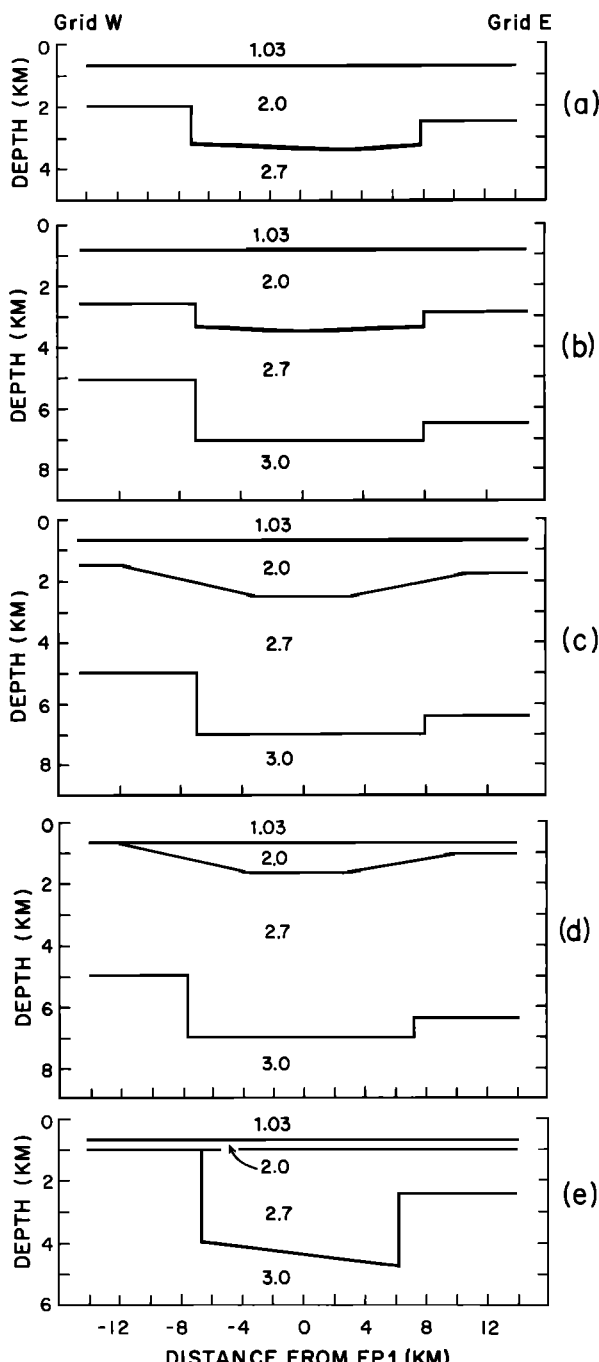


Fig. 33. Density models for the grid east-west profile through survey point EP1 (Figure 25) near base camp C-16. Densities are given in megagrams per cubic meter.

Sea in the grid southwestern corner of the rectangle. As the focus of our study is the Ross embayment, we made no attempt to fill in these corners with realistic estimates of gravity and bathymetry. A plane was fit by least squares to the real data in order to remove the mean and trend. This procedure is standard in time series analysis for minimizing distortions in the finite Fourier transform. Corner data points were then filled with zeroes. Frequency domain representations of the Bouguer and free-air gravity and the bathymetry were computed using MATLAB on an Apple McIntosh computer.

Spatial frequency spectra are generally presented as contour maps of amplitudes of spatial frequency components with the vertical and horizontal axes representing spatial frequencies in the conventional (here grid) map directions. The spectral amplitude at a point (f_x, f_y) on the spatial frequency spectrum represents the amplitude of a "corrugated" wavy surface whose crests and troughs strike normal to the line through the origin and that point. The angular spatial frequency of this corrugated surface $(f_x^2 + f_y^2)^{1/2}$ corresponds to the distance of the point from the origin. Since the original data are represented by real numbers, the spatial frequency spectrum is symmetric about the origin.

Figures 36 to 38 show the magnitudes of the spatial frequency components of the free-air anomaly, Bouguer anomaly, and bathymetry, respectively. The sampling interval of 55.5 km means that the shortest

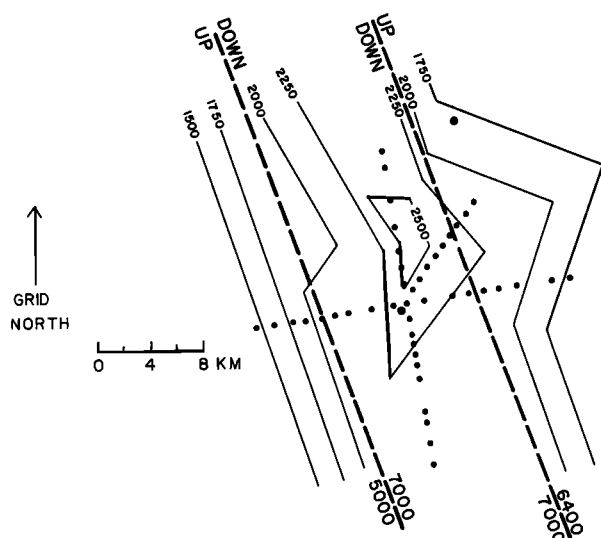


Fig. 34. Diagram of three-dimensional density model, base camp C-16. Solid contours show depths in meters to the base of the sediment layer (layer 2); dashed lines show faults on the boundary between layer 3 and layer 4 with depths to that boundary. Densities are the same as in Figure 33.

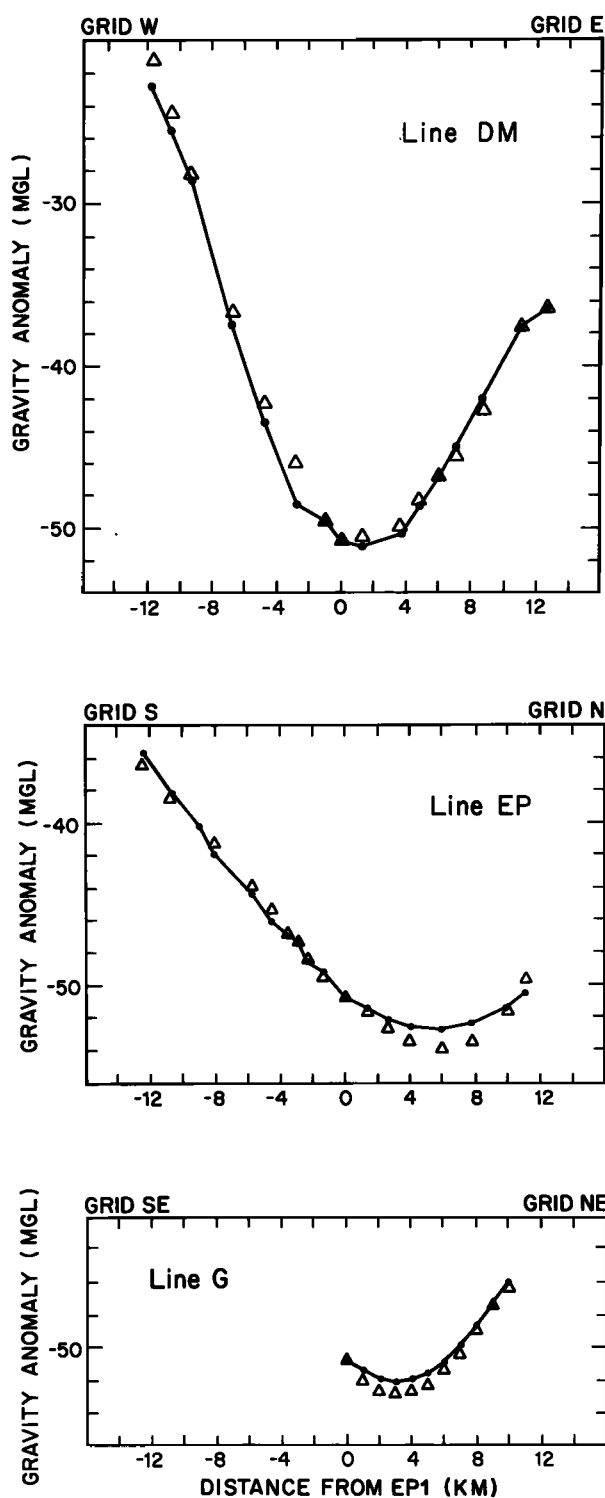


Fig. 35. Free-air anomaly profiles along three lines through survey point EP1 near base camp C-16 (compare Figure 25). Observed values are denoted by circles, and values from the three-dimensional model are shown by triangles.

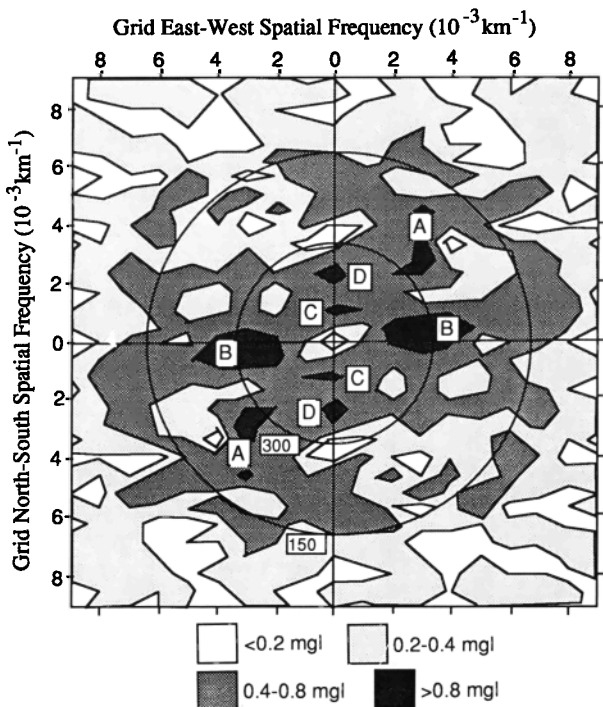


Fig. 36. Spectrum of free-air gravity anomalies in the Ross embayment. Spatial frequencies are in cycles per thousand kilometers. Circles denote wavelengths of 150 km and 300 km, as marked. Letters mark features referred to in the text.

wavelength sampled along each axis is 111 km. The longest wavelengths are 999 km (18×55.5 km) in the grid east-west direction and 1776 km (32×55.5 km) in the grid north-south direction. Circles corresponding to wavelengths of 300 and 150 km are drawn in each figure for reference.

The free-air anomaly (Figure 36) and bathymetric (Figure 38) spectral maps show high amplitudes (>0.8 mGal, >8 m) at wavelengths around 250 km in the grid northeast-southwest direction (labeled A in Figures 36 and 38, respectively) corresponding to spatial features aligned along grid NW-SE. These arise from the bathymetric ridges and troughs and associated free-air anomalies in the grid northwestern part of the embayment. The corresponding north-south features in the grid eastern embayment can be seen near wavelengths of 300 km along the east-west axes in all three spectra (labeled B in Figures 36–38). Both sets of features are prominent on the maps of gravity and bathymetry low-pass filtered at 160 km (Figures 3b, 4b, and 5b).

There are high spectral amplitudes at wavelengths of about 900 km along the grid north-south axis on all three spectral maps (labeled C in Figures 36–38). These correspond to alternating highs and lows that show up clearly on the maps filtered at 870 km (see

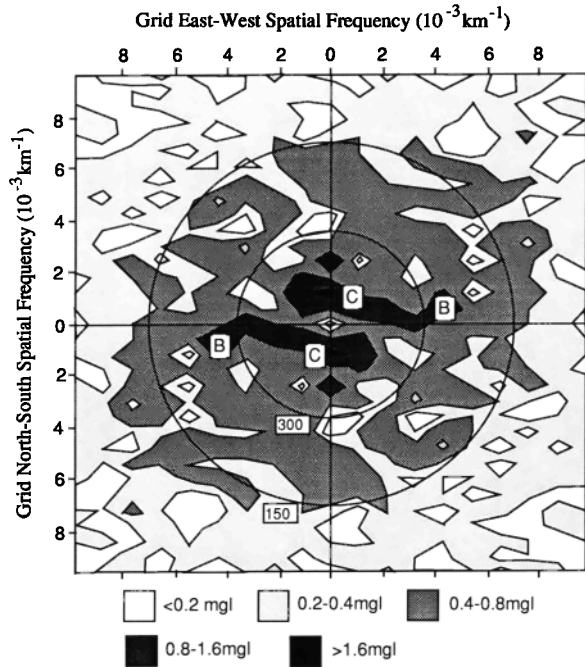


Fig. 37. Spectrum of Bouguer gravity anomalies in the Ross embayment. Spatial frequencies are in cycles per thousand kilometers. Circles denote wavelengths of 150 km and 300 km, as marked. Letters mark features referred to in the text.

Figures 41–43). The free-air anomalies contain an additional spectral maximum at around 500 km on the north-south axis (labeled D in Figure 36) whose origin is uncertain.

Gravity Admittance Function

Insight into the realization of isostasy can be obtained by analyzing the correlation between gravity and elevation [Lambeck, 1988, section 9.1.2]. The filter function or admittance, which relates gravity to bathymetry in the spatial frequency domain, is given by

$$G(f_n, \theta_i) = Z(f_n) \times B(f_n, \theta_i)$$

where Z is the complex admittance, G is the transform of the gravity observations, B is the transform of the bathymetry, f_n is the spatial frequency, and θ_i is the azimuth. We assume that Z is independent of azimuth so that the effects of noise can be reduced by averaging over all azimuths. Then $Z(f_n)$ is estimated by

$$Z(f_n) = \frac{\sum_{i=1}^N G(f_n, \theta_i) \times B^*(f_n, \theta_i)}{\sum_{i=1}^N B(f_n, \theta_i) \times B^*(f_n, \theta_i)} \quad (5)$$

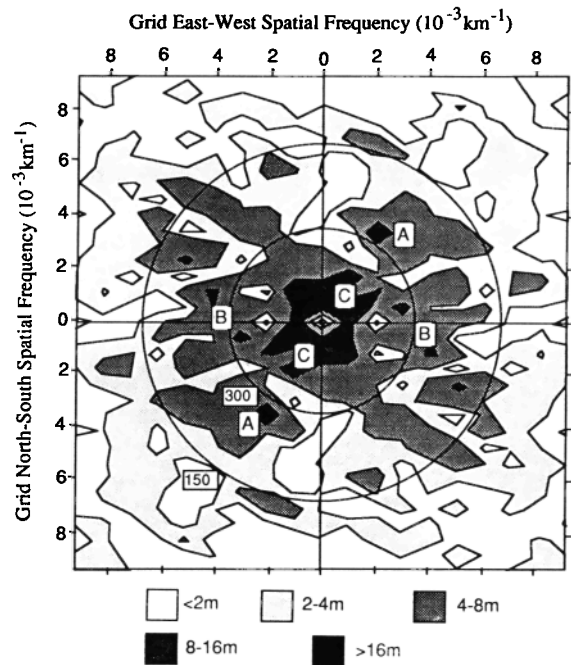


Fig. 38. Spectrum of submarine topography anomalies in the Ross embayment. Spatial frequencies are in cycles per thousand kilometers. Circles denote wavelengths of 150 km and 300 km, as marked. Letters mark features referred to in the text.

The asterisks denote the complex conjugates, and N , which depends upon f_n , is the number of azimuths.

An estimate of the fraction of the power spectrum of the gravity anomalies that results (directly or indirectly) from bathymetry, is given by the coherence $C(f_n)$, where

$$C^2(f_n) = \frac{\left[\sum_{i=1}^N G(f_n, \theta_i) \times B^*(f_n, \theta_i) \right]}{\left[\sum_{i=1}^N B(f_n, \theta_i) \times B^*(f_n, \theta_i) \right]} \cdot \frac{\left[\sum_{i=1}^N G(f_n, \theta_i) \times B^*(f_n, \theta_i) \right]^*}{\left[\sum_{i=1}^N G(f_n, \theta_i) \times G^*(f_n, \theta_i) \right]} \quad (6)$$

(see, e.g., *McKenzie and Bowin* [1976]).

The free-air gravity admittance and coherence functions were computed for the Ross embayment from equations (5) and (6) in spatial frequency bands $1/1776 \text{ km}^{-1}$ wide. Sixteen points were computed for spatial frequencies $n/1776 \text{ km}^{-1}$, $n = 1-16$; N

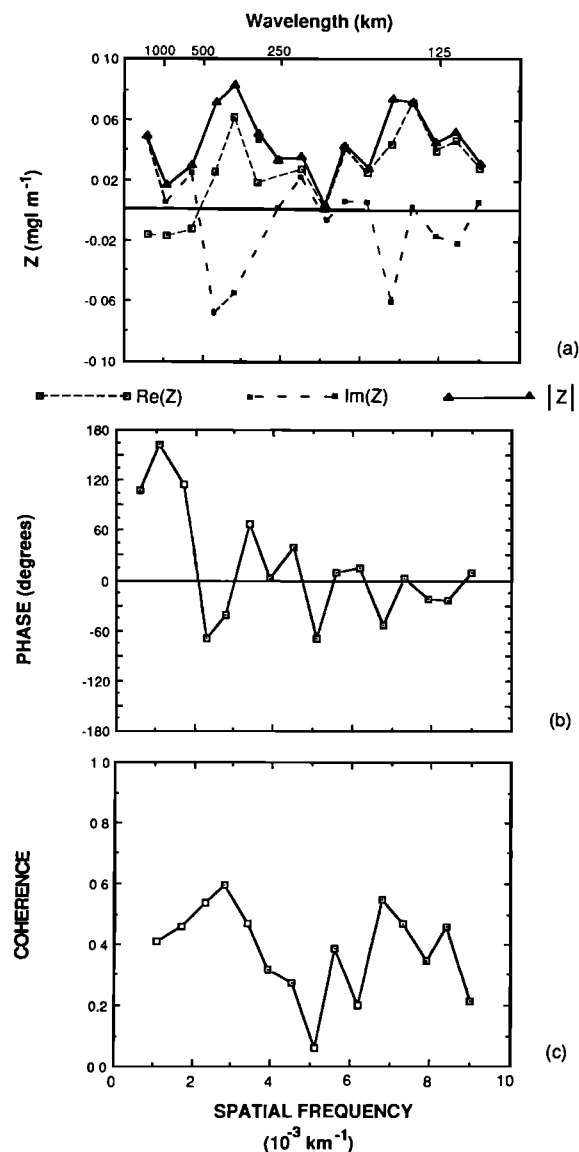


Fig. 39. Spectrum of the free-air gravity versus bathymetry admittance function: (a) real part (open squares), imaginary part (solid squares), and magnitude (triangles); (b) phase; (c) coherence.

correspondingly ranged from 1 to 24. Mean values were subtracted from both the gravity anomalies and the bathymetry, so smaller water depths and less negative anomalies were transformed into positive numbers. The real part, imaginary part, and magnitude of $A(f)$ are plotted in Figure 39a, its phase is plotted in Figure 39b, and the coherence is plotted in Figure 39c.

For very high spatial frequencies, i.e., topographic wavelengths short enough not to be isostatically compensated, one would expect a high coherence

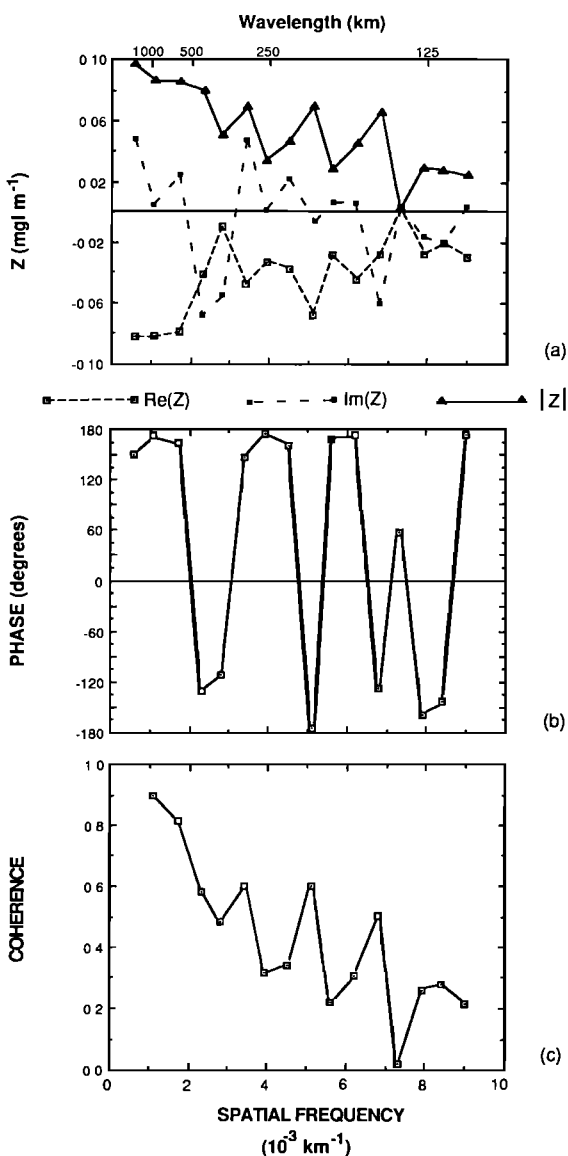


Fig. 40. Spectrum of the Bouguer gravity versus bathymetry admittance function: (a) real part (open squares), imaginary part (solid squares), and magnitude (triangles); (b) phase; (c) coherence.

between the free air anomaly and the bathymetry, and the magnitude of Z should approximate the submarine Bouguer correction: 0.07 mGal m^{-1} . If topography and compensation were the only effects, $|Z|$ should then diminish toward zero at the wavelength limit. In the presence of additional sources of gravity anomalies unrelated to the topography, the coherence would also diminish with increasing wavelength.

The representation of the Ross embayment (Figure 39) is far different. The admittance and the coherence both show strong maxima around wavelengths of 150

km and 350 km and a minimum around 200 km; at both maxima, $|Z|$ equals or even exceeds the expected value for totally uncompensated topography. Clearly, these maxima must reflect structure beneath the seafloor. Since the phase of Z is about 0° (Figure 39b), there must be at least the same thickness of relatively low density rocks beneath the topographic troughs as beneath the ridges. The existence of two maxima suggests that there are two characteristic wavelengths to the structure, a feature that is not readily apparent from the spatial or spectral maps themselves. The large amplitude at 350 km makes it unlikely that this peak is simply a subharmonic, or modulation, of the 150-km peak. This evidence of deep structure correlated with the ridge-trough topography is further support for the concept of the Ross embayment as a rift zone.

At the longest wavelengths, $|Z|$ again becomes large, but with a phase that is closer to 180° than to 0° . This we interpret to reflect incomplete isostatic recovery after retreat of a more extended late Pleistocene grounded ice sheet. The phase reversal arises because of the decrease in water depth grid westward beneath the ice shelf, a decrease that is unrelated to, and in fact masks, the remanent glacio-isostatic depression (see the next section).

The decrease in free-air gravity grid westward across the embayment combined with the decrease in water depth leads to the pronounced Bouguer gravity gradient seen in Figure 42. That combination appears also in the Bouguer gravity admittance and coherence functions (Figure 40) as the large magnitude, reversed phase, and high coherence at long wavelengths. The disappearance of the peaks around 150 km and 350 km shows that the free-air anomalies at these wavelengths are caused principally by the submarine topography, a fact upon which we already commented in noting that the corresponding values of $|Z|$ for the free-air anomalies were about 0.07.

The strong nonisostatic signal in the Ross embayment precludes the modeling of the computed admittance in terms of the isostatic response of the Earth's crust and upper mantle.

Speculations on Glaciological Implications of Isostatic Gravity

To search for the imprint of isostasy, we have filtered the gravimetric and bathymetric maps at 870 km (Figures 41–43). A pronounced inverse correlation between bathymetry and Bouguer anomalies, which indicates that the large-scale features are isostatically compensated, is apparent in Figures 42 and 43. The ratio of gravity difference to bed elevation difference between the relatively shallow water around Iselin Bank in the grid southern Ross Sea and

the deep water along the Transantarctic Mountain front beneath the grid eastern Ross Ice Shelf is about $-0.07 \text{ mGal m}^{-1}$, which is the value expected for oceanic compensation. However, the same ratio computed for the grid eastern to the grid northwestern Ross Ice Shelf is about $-0.10 \text{ mGal m}^{-1}$, which is 50% greater (numerically) than the value expected for oceanic compensation and is associated with a pronounced gradient in the free-air anomaly (Figure 41). We believe that this extra 50% is due to glacio-isostatic imbalance.

If part of the regional free-air anomaly field in the Ross embayment does indeed arise from remanent crustal depression caused by ice loading during late Wisconsin/Holocene time, then it reflects the former extent of the Antarctic ice sheet in this area, the degree of isostatic equilibrium attained by this ice sheet, and its retreat history. We will attempt first to separate the glacio-isostatic signal from other gravity effects.

Free-air gravity anomalies from Goddard Earth Model (GEM) 10B computed through degree and order 4 (Figure 44) should represent deep-seated mantle effects [Bentley *et al.*, 1982]. Gravity anomalies on our low-passed free-air anomaly map (Figure 41) are more negative than the low-order satellite-derived gravity field and have a different trend: the latter increase grid northward from -14 mGal to -11 mGal across the Ross embayment, whereas the former decrease from greater than -20 mGal to less than -28 mGal grid northwestward across the ice shelf.

There is little doubt that during late Wisconsin time the grounded portion of the West Antarctic ice sheet extended farther seaward into the Ross embayment than at present, but the amount and duration of the grounding line advance are a matter of some dispute. The "maximum" reconstruction of Denton *et al.* [1989] for the late Wisconsin maximum (Figure 45) indicates that the West Antarctic ice sheet was then approximately 1000 m thick near the present grounding line and that the grounded margin was near the edge of the continental shelf. Evidence from Ross Sea cores also suggests that grounded ice reached the continental shelf margin during the late Pleistocene [Kellogg *et al.*, 1979]. Geologic data in McMurdo Sound and the dry valley areas yield minimum ages of ice retreat ranging from 3000 to 10,000 years B.P. [Denton *et al.*, 1970] and have further been interpreted as showing that the grounding of the ice sheet occurred more than 47,000 years B.P. [Denton and Bons, 1974], long enough ago for isostatic compensation to have become virtually complete.

Not all investigators accept this model. Some analyses of marine and glacial geologic evidence indicate only minor expansions of the grounded ice

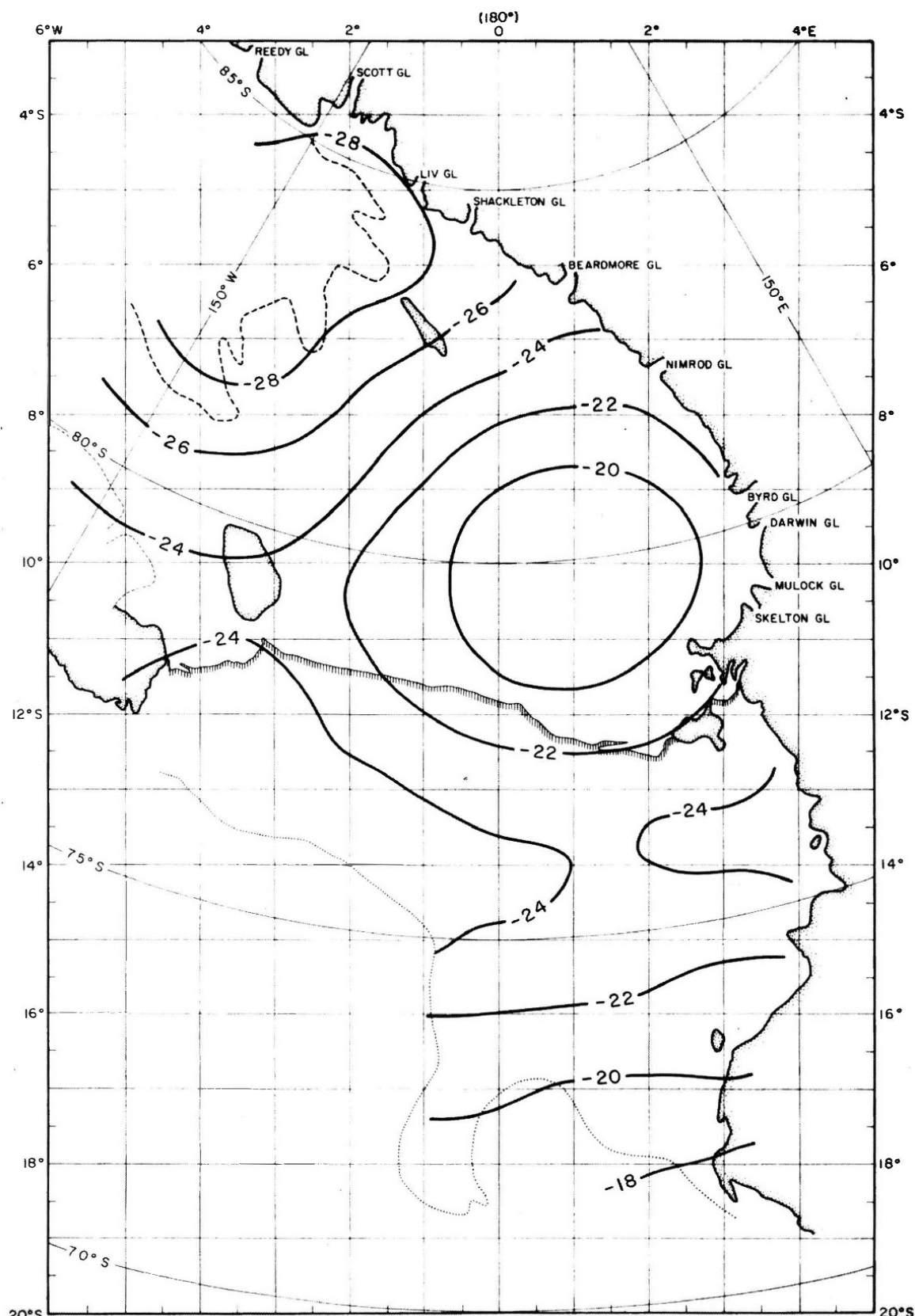


Fig. 41. Map of free-air anomalies in the Ross embayment, filtered to remove wavelengths less than 870 km. The contour interval is 10 mGal.

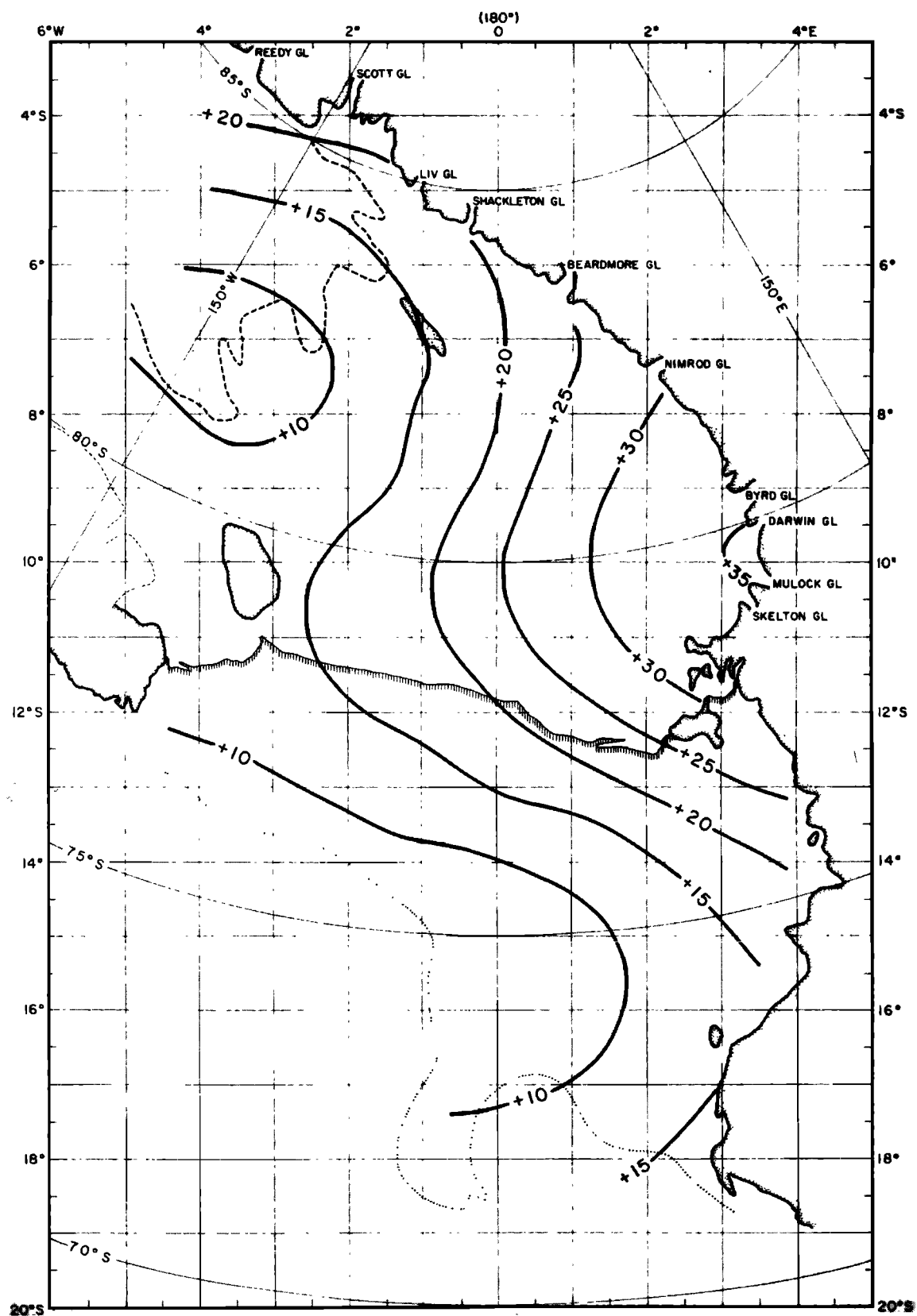


Fig. 42. Map of Bouguer anomalies in the Ross embayment, filtered to remove wavelengths of less than 870 km. The contour interval is 10 mGal.

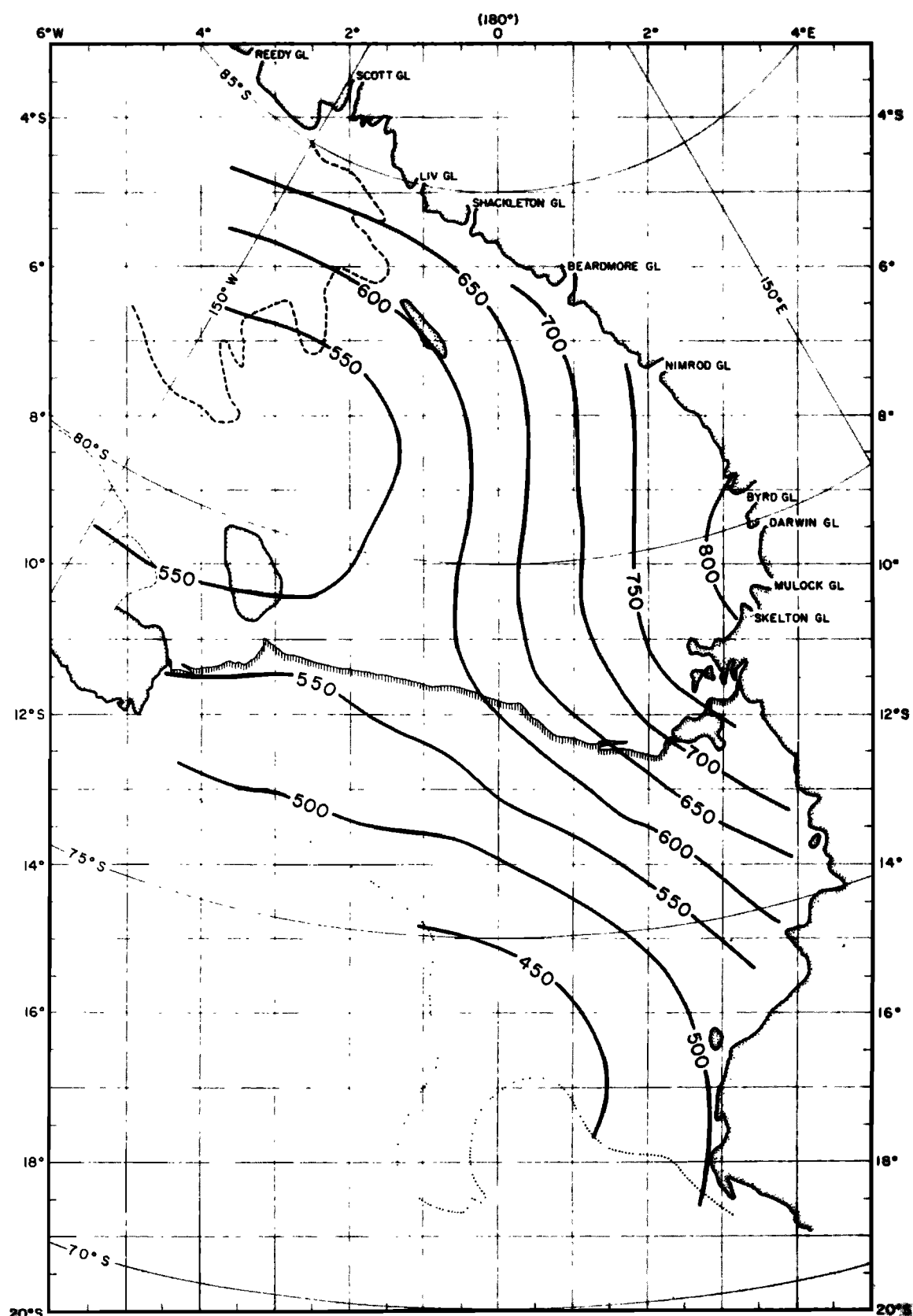


Fig. 43. Map of submarine topography anomalies in the Ross embayment, filtered to remove wavelengths of less than 870 km. The contour interval is 50 m.

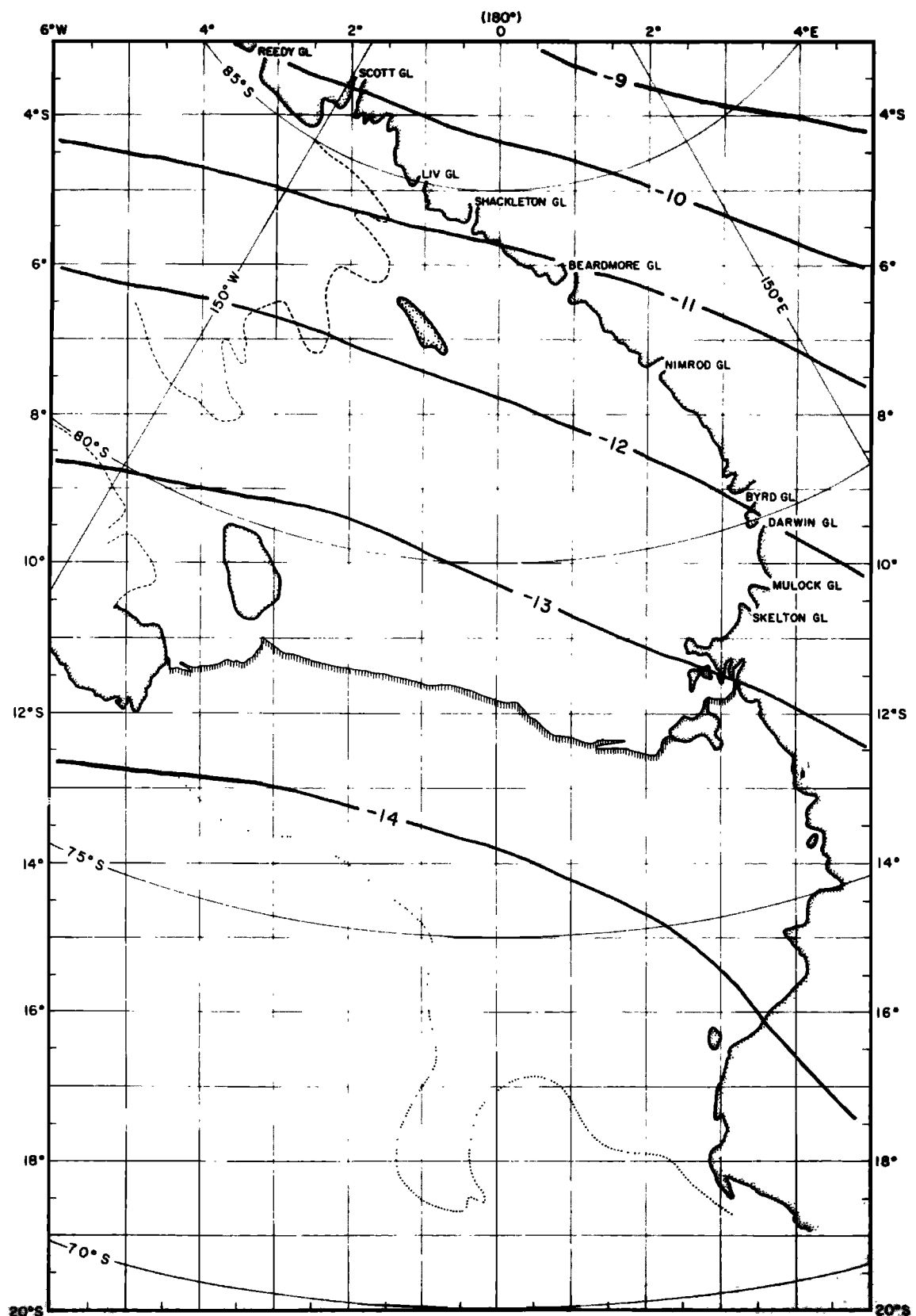


Fig. 44. Free-air gravity contours in the Ross embayment from gravity model GEM 10B, spherical harmonics through degree and order 4. The contour interval is 1 mGal.

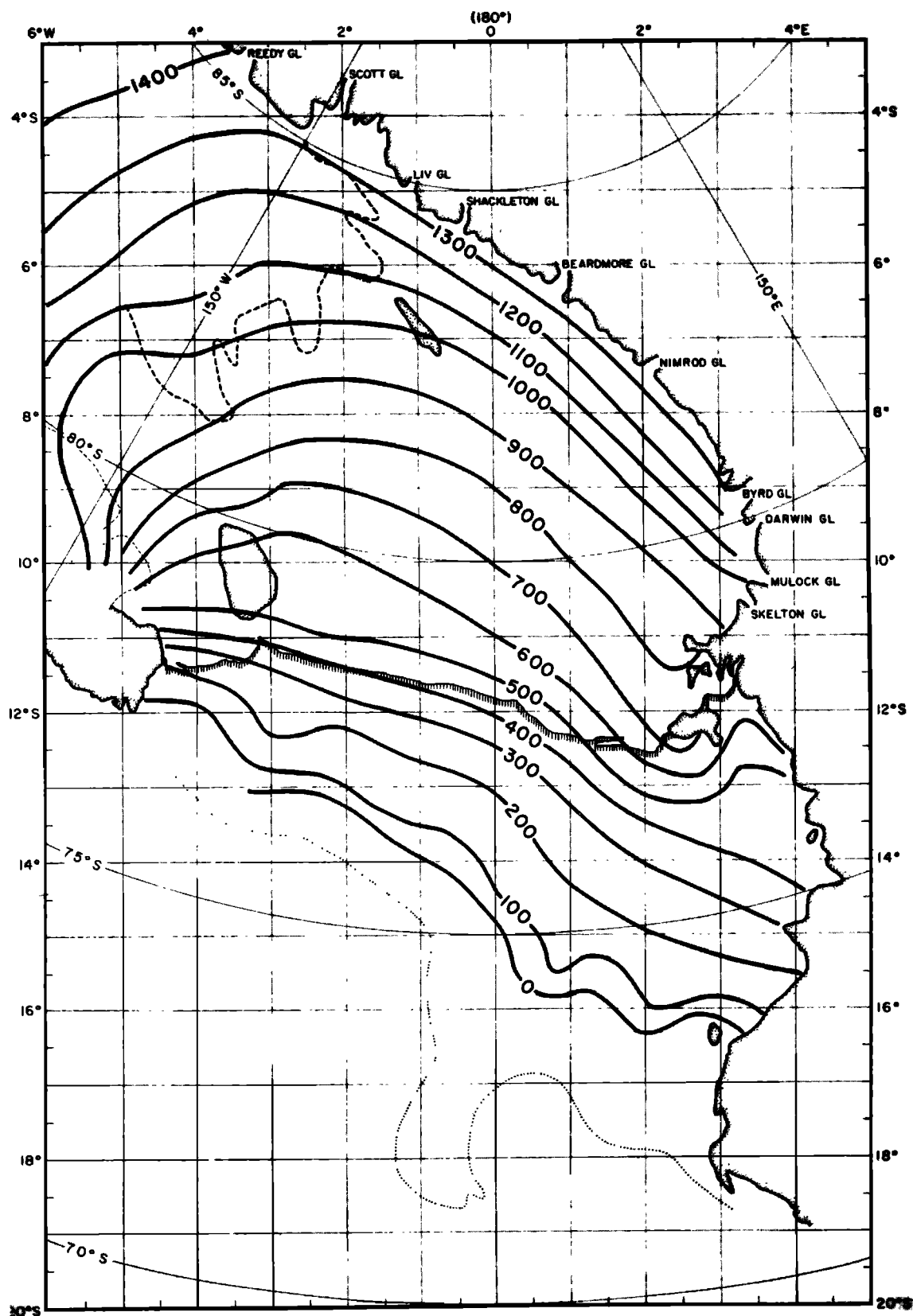


Fig. 45. Map of grounded ice thickness in the Ross embayment during the late Pleistocene glacial maximum, according to the "maximum" reconstruction of Denton *et al.* [1989]. The contour interval is 100 m.

during the Quaternary [Fillon, 1975; Drewry, 1979; Mayewski and Goldthwait, 1985]. Drewry's [1979] reconstruction shows grounding line advance approximately to a line extending from Roosevelt Island to Beardmore Glacier with isolated grounding on shoals in the Ross Sea and around Ross Island. The minimum reconstruction of Denton et al. [1989] is similar to Drewry's with the addition of extensive grounding in the grid eastern Ross embayment.

"Minimum" models for the advance of grounded ice leave the margin approximately in the middle of the gradient in regional gravity, so that the grid southeastern portion of the gravity gradient would have to be attributed to sources other than glacial isostasy. But regional gravity gradients of 10 mGal per thousand kilometers are uncommon in regions away from lithospheric plate boundaries. Furthermore, the gravity gradient on the Ross Ice Shelf is primarily parallel rather than normal to the Transantarctic Mountains. Thus we will assume that the regional gravity gradient reflects incomplete recovery of the lithosphere from former ice loading. We will adopt the "maximum" model of Denton et al. [1989] for the purpose of modeling.

The anomaly gradient can be interpreted qualitatively as implying that the ice sheet retreated from grid east to grid west. To model this retreat, we assume that crustal uplift following "instantaneous" unloading can be adequately described by a simple exponential equation [Heiskanen and Vening Meinesz, 1958; Andrews, 1968; Walcott, 1969; Cathles, 1975] and take the Denton et al. [1989] maximum ice sheet model. The lithospheric depression remaining at present, Z_p , is given by

$$Z_p = Z_0 \exp(-t/t_r) \quad (7)$$

where Z_0 is the original lithospheric depression, t is time since unloading, and t_r is a time constant that depends upon the size of the rebounding area. Cathles [1975] plotted t_r versus linear dimension from values measured in the northern hemisphere and predicted by model studies. Figure 46, adapted from Cathles [1975], shows that for the linear dimension of the Ross embayment (~1000 km) t_r is approximately 4400 years and is relatively independent of both the linear dimension of the load and the crustal rigidity.

From equation (7) the time since unloading is

$$t(\text{years}) = 4400 \ln(Z_0/Z_p) \quad (8)$$

Z_p can be estimated from Δg , the difference between the regional free-air gravity anomaly and the reference field (GEM 10B) using the flat plate approximation

$$Z_p = \frac{\Delta g}{0.042\Delta\rho} \text{ m}$$

where $\Delta\rho = 2.27 \text{ Mg m}^{-3}$, the density contrast between seawater and mantle material, and Δg is in milligals. Bennett [1964] derived an equation for Z_0 in terms of former ice thickness, T (taken from Denton et al. [1989] "maximum" reconstruction Figure 45), and the present average depth of the seafloor, \bar{D} (≈ 650 m):

$$Z_0 = \frac{\rho_i}{\rho_m} T - \frac{\rho_w}{\rho_m} (\bar{D} - Z_p)$$

where ρ_i , ρ_w , and ρ_m are densities of ice, seawater, and mantle rock, respectively. Equation (8) can now be solved for t , the time since "instantaneous" ice unloading occurred.

Critical to this calculation of t is the choice of Δg . The entire difference between the low-pass-filtered gravity anomaly and the GEM 10B fourth-order model (Figure 47) may not reflect only glacio-isostatic imbalance [Bentley et al., 1982] and, in fact, cannot, if the assumed "maximum" ice sheet configuration is approximately correct, because negative anomalies of 4 to 10 mGal lie beyond the edge of that ice sheet (Figure 45).

Consequently, we assume that those negative values of Δg represent a uniform bias for the entire Ross embayment. The mean of Δg in the northern Ross Sea is about -5 mGal; so we increase Δg (decrease Δg numerically) everywhere by 5 mGal. This does not entirely solve the problem, as the isostatic gravity minimum in the southern Ross Sea is in some places still numerically too large to represent even no recovery at all after retreat of the extended ice sheet. Nevertheless, we proceed to model the retreat over the ice shelf itself to see what sort of a model is implied if glacio-isostatic imbalance is, as we believe,

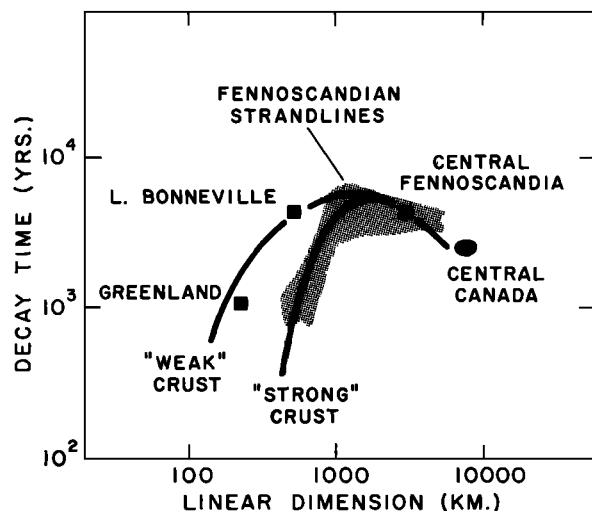


Fig. 46. Decay time constant for isostatic rebound versus linear dimension of areas relieved of loads of ice (Canada, Greenland, Fennoscandia) or water (Lake Bonneville). Adapted from Cathles [1975].

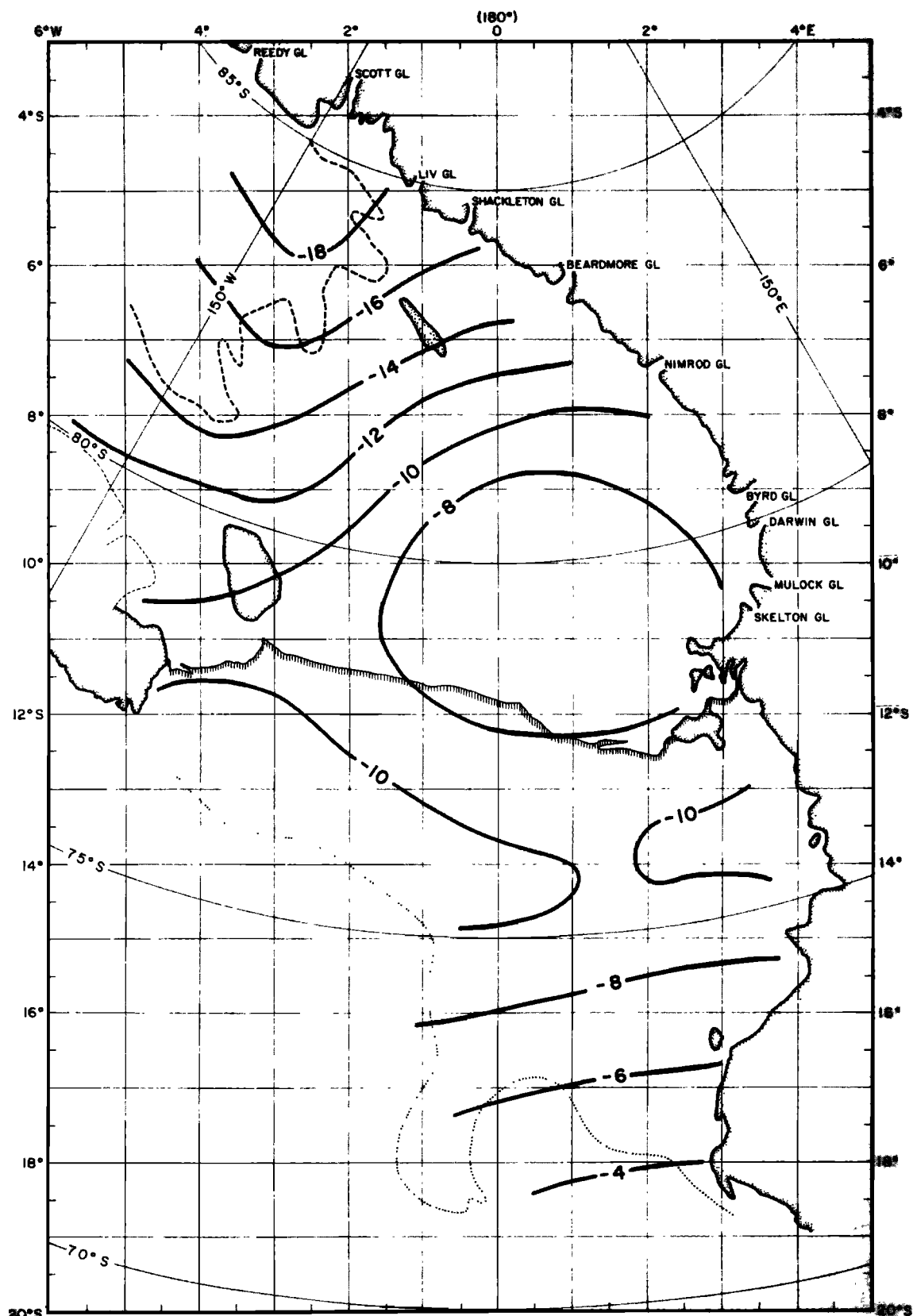


Fig. 47. Map of Δg , the difference between the free-air anomaly fields mapped in Figures 41 and 44, in the Ross embayment. The contour interval is 2 mGal.

the principal source of the observed isostatic anomaly pattern. The resulting map (Figure 48) shows progressive unloading across the ice shelf from more than 10,000 (actually ~12,000) to 4000 years ago. This retreat history is generally similar in timing and configuration to those of *Thomas and Bentley* [1978], *Stuiver et al.* [1981], *Fastook* [1984], and *Lingle* [1984]. Despite the uncertainties about the non-glacio-isostatic component of the isostatic anomalies, we take this agreement as supportive of a model like the maximum reconstruction of *Denton et al.* [1989] rather than a model that involves only a minor advance of the grounding line in the Ross embayment during the late Pleistocene. (The gravity anomalies are also consistent with an ice sheet model [*Stuiver et al.*, 1981] that implies grounding across the entire continental shelf [Greischar, 1982]; however, such a model appears to be incompatible with glacial geological evidence along the East Antarctic margin of the embayment [*Denton et al.*, 1989].)

Isostatic Equilibrium Grounding Line Between the West Antarctic Inland Ice Sheet and the Ross Ice Shelf

Greischar and Bentley [1980] showed how the grounding line might advance if rebound continues and ice dynamic effects do not predominate. Their minimum advance line would have to be moved farther into the ice shelf in light of recent discoveries about the current position of the grounding line; the maximum advance line would not be affected. However, recent knowledge of the dynamic non-steady state of the ice sheet [*Shabtaie et al.*, 1988; *Bindschadler et al.*, 1989] and likely subglacial/submarine sedimentation [*Alley et al.*, 1989] makes it unlikely that isostatic rebound effects will dominate grounding line movement.

SUMMARY

By Antarctic standards the RIGGS gravity survey is remarkably good, both for its areal coverage and for the accuracy of observations. The Ross Ice Shelf, with an area of 560,000 km², was covered by a grid of stations spaced approximately 55 km apart. Since most of the gravity observations were made on floating ice, where accurate elevations could be computed from ice thicknesses, the effect of the commonly principal source of error in calculating gravity anomalies in Antarctica was greatly diminished.

Free-air, Bouguer, and Airy isostatic anomaly maps of the Ross embayment reveal long linear anomalies paralleling the Transantarctic Mountains that are a dominant feature on all of the maps. A likely tectonic

source for these anomalies is block faulting due to extension between East Antarctica and West Antarctica. Deep structural control of gravity lineations implies deep structural control of sea bottom topographic lineations since the two sets of lineations are close to parallel. The control obviously predates the current episode of glaciation in West Antarctica, which suggests that long-standing geologic conditions have determined such glaciological phenomena as the present courses of ice streams. The topography of the ocean bottom below the ice shelf is not fundamentally determined by the ice streams themselves.

The regional data are too widely spaced to determine whether the transition between the gravity highs and lows is steep, indicative of faulting, or gradual, indicative of folding. However, four out of five gravity surveys, at four widely scattered sites (base camps RI, Q13, and C-16 and station J9DC), indicated faults approximately paralleling the Transantarctic Mountains. Faulting also was indicated at the fifth (base camp BC), although there the direction parallels a secondary grid northeast-southwest trend running through Crary Ice Rise. The correspondence of the strikes of these locally modeled structures to regional trends suggests that they are the result of regional tectonic activity.

Spectra were calculated for the free-air anomaly, Bouguer anomaly, and bathymetric maps of the Ross embayment, and an admittance function relating bathymetry to free-air anomaly was calculated to investigate the gravitational response to topographic loading. This technique revealed a long-wavelength signal that we interpret to reflect incomplete isostatic recovery from the load of a more extended late Pleistocene ice sheet. Admittance maxima at shorter wavelengths (150 km and 350 km) we believe to be related to tectonically produced troughs and ridges with trends parallel to the Transantarctic Mountains.

There is little doubt that during late Wisconsin/Holocene time the grounded portion of the West Antarctic ice sheet extended farther seaward than at present. The fact that the low-passed ($\gamma \geq 870$ km) free-air gravity anomalies are even more negative than the low-order satellite-derived gravity field in the Ross embayment suggests recent grounding of the West Antarctic ice sheet out to, or nearly to, the edge of the continental shelf in the Ross Sea. Using the "maximum model" of *Denton et al.* [1989] as a reconstruction of the Antarctic ice sheet during the late Wisconsin glacial maximum and a simple exponential model of crustal rebound, isochrons of grounding line retreat have been mapped in the Ross embayment. The general aspects of this retreat are similar to those calculated from ice dynamical models.

The water layer beneath the Ross Ice Shelf is thin enough near the present grounding line that isostatic

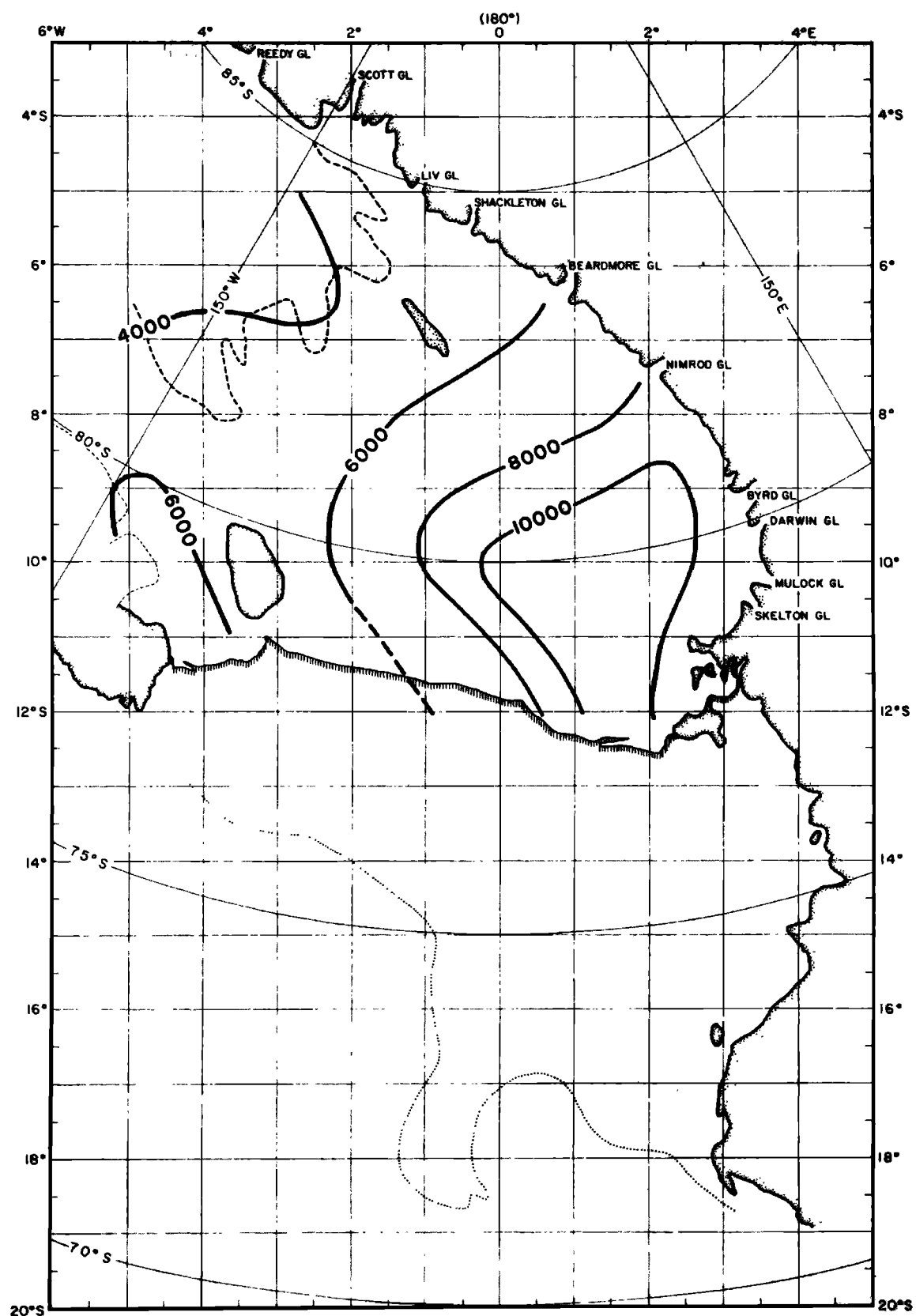


Fig. 48. Map of Holocene retreat of grounded ice from the Ross Ice Shelf modeled on the assumption that $\Delta g + 5$ mGal represents the glacio-isostatic imbalance. The contour interval is 2000 years B.P.

rebound could lead to a kilometer of grounding line advance for each meter of uplift. If the West Antarctic ice sheet were approximately in steady state, an advance of the grounding line into the Ross Ice Shelf would be expected. However, it is probable that ice dynamic effects will swamp isostatic rebound effects in this highly non-steady state system.

APPENDIX

The principal facts for all the RIGGS gravity stations and all other gravity stations on the Ross Ice Shelf are listed in Tables A1-A6 (on microfiche, enclosed in a pocket inside the back cover of this book). An explanation of the columns and column headings follows.

Stn, station.

Numerals in the left column under Code refer to the year of measurement. I: 1973-1974; II: 1974-1975; III: 1976-1977; IV: 1977-1978; letters in the right column refer to the kind of position measurement. G: geoceiver; GR: geoceiver-real time only; I: aircraft inertial navigation system; S: sunshots; L: sighting on landmarks.

GLAT, grid latitude, degrees south.

GLON, grid longitude, degrees.

T_i , ice thickness, meters.

T_w , water layer thickness, meters.

G obs, observed gravity.

Elev, elevation of the ice surface, calculated from the ice thickness except where otherwise indicated by superscripts: 1, from elevation map [Shabtaie and Bentley, 1987]; 2, geoceiver measurement; 3, altimeter measurement.

Depth, depth to the sea floor, meters below sea level.

FAA, free-air anomaly, milligals.

BA, Bouguer anomaly, milligals.

IA, isostatic anomaly, milligals.

Table A7 gives the magnitudes and direction of local gravity gradients at RIGGS stations.

Tables A8-A12 contain the free-air gravity anomalies in the five extensive local surveys, at base camp BC, station J9DC, and base camps RI, Q13, and C-16.

Note. This paper was written as a contribution to Antarctic Research Series volume 42, *The Ross Ice Shelf: Glaciology and Geophysics*, but is published here instead for technical reasons. It should be thought of as paper 6 of that series.

Acknowledgments. We would like to thank especially the many other members of the RIGGS field parties for their capable assistance in collecting the data presented here. Particular thanks go to Tom Kolich for the many hours

spent taking gravity readings. The logistic support of Holmes and Narver, Inc., United States Naval Support Force, Antarctica, and Antarctic Development Squadron Six is gratefully acknowledged. Discussions with J. W. Clough, J. D. Robertson, and C. S. Lingle were helpful during the early stages of writing. Consultation with C. S. Clay substantially improved the section on admittance functions. Comments by U. S. ten Brink and an anonymous referee led to substantial improvements in the paper. This work was supported by National Science Foundation grants GV-36963 and DPP79-20736. This is contribution 511 of the Geophysical and Polar Research Center, University of Wisconsin, Madison.

REFERENCES

- Albert, D. G., and C. R. Bentley, Seismic studies on the grid eastern half of the Ross Ice Shelf, Antarctica: RIGGS III and RIGGS IV, in *The Ross Ice Shelf: Glaciology and Geophysics, Antarct. Res. Ser.*, vol. 42, edited by C. R. Bentley and D. E. Hayes, pp. 87-108, Washington, D. C., 1990.
- Albert, D. G., C. R. Bentley, and L. L. Greischar, 1978, Submarine topography of the Ross embayment from the continental shelf to the Byrd Subglacial Basin, paper presented at the 1978 AGU Spring Meeting, Miami Beach, Fl., April 17-21, 1978.
- Alley, R. B., D. D. Blankenship, S. T. Rooney, and C. R. Bentley, Sedimentation beneath ice shelves—The view from Ice Stream B, *Mar. Geol.*, 85, 101-120, 1989.
- Andrews, J. T., The pattern and interpretation of restrained postglacial and residual rebound in the area of Hudson Bay, in *Earth Science Symposium on Hudson Bay*, edited by P. J. Hood, pp. 49-62, Geological Survey of Canada, Ottawa, Ont., 1968.
- Behrendt, J. C., Gravity increase at the south pole, *Science*, 155, 1015-1017, 1967.
- Behrendt, J. C., W. E. LeMasurier, A. K. Cooper, E. Tessensohn, A. Treku, and D. Damaske, The West Antarctic rift system: A review of geophysical investigations, in *Contributions to Antarctic Research II, Antarct. Res. Ser.*, vol. 53, edited by D. H. Elliot, pp. 67-112, AGU, Washington, D. C., 1991.
- Bennett, H. F., A gravity and magnetic survey of the Ross Ice Shelf area, Antarctica, *Res. Rep.* 64-3, Geophys. and Polar Res. Center, Univ. of Wis., Madison, 1964.
- Bentley, C. R. The structure of Antarctica and its ice cover, in *Research in Geophysics, Solid Earth and Interface Phenomena*, vol. 2, edited by H. Odishaw, pp. 335-389, Massachusetts Institute of Technology, Cambridge, 1964.
- Bentley, C. R., Secular increase of gravity at South Pole Station, in *Antarctic Snow and Ice Studies II, Antarct. Res. Ser.*, vol. 16, edited by A. P. Crary, pp. 191-198, AGU, Washington, D. C., 1971.
- Bentley, C. R., Crustal structure of Antarctica, *Tectonophysics*, 20(1-4), 229-240, 1973.
- Bentley, C. R., The Ross Ice Shelf geophysical and glaciological survey (RIGGS): Introduction and summary of measurements performed, in *The Ross Ice Shelf: Glaciology and Geophysics, Antarct. Res. Ser.*, vol. 42, edited by C. R. Bentley and D. E. Hayes, pp. 1-20, AGU, Washington, D. C., 1984.

- Bentley, C. R., and J. D. Robertson, Isostatic gravity anomalies in West Antarctica, in *Antarctic Geoscience*, edited by C. Craddock, pp. 949–954, University of Wisconsin Press, Madison, 1982.
- Bentley, C. R., J. D. Robertson, and L. L. Greischar, Isostatic gravity anomalies on the Ross Ice Shelf, Antarctica, in *Antarctic Geoscience*, edited by C. Craddock, pp. 1077–1081, University of Wisconsin Press, Madison, 1982.
- Bindschadler, R. A., E. P. Roberts, and D. R. MacAyeal, Distribution of net balance in the vicinity of Crary Ice Rise, Antarctica, *J. Glaciol.*, 35, 370–377, 1989.
- Cathles, L. M., *The Viscosity of the Earth's Mantle*, Princeton University Press, Princeton, N. J., 1975.
- Chiang, E., and C. C. Langway, Antarctic ice core recovery, *Antarct. J. U. S.*, 13, 59–61, 1978.
- Clough, J. W., and B. L. Hansen, The Ross Ice Shelf project, *Science*, 203, 433–434, 1979.
- Cooper, A. K., and F. J. Davey (Eds.), *The Antarctic Continental Margin: Geology and Geophysics of the Western Ross Sea*, *Earth Sci. Ser.*, vol. 5B, Circum-Pacific Council for Energy and Mineral Resources, Houston, Tex., 1987.
- Cooper, A. K., F. J. Davey, and J. C. Behrendt, Seismic stratigraphy and structure of the Victoria Land basin, western Ross Sea, Antarctica, in *The Antarctic Continental Margin: Geology and Geophysics of the Western Ross Sea*, *Earth Sci. Ser.*, vol. 5B, edited by A. K. Cooper and F. J. Davey, pp. 27–76, Circum-Pacific Council for Energy and Mineral Resources, Houston, Tex., 1987.
- Cooper, A. K., F. J. Davey, and K. Hinz, Crustal extension and origin of sedimentary basins beneath the Ross Sea and Ross Ice Shelf, Antarctica, in *Geological Evolution of Antarctica*, edited by M. R. A. Thomson, J. A. Crame, and J. W. Thomson, pp. 285–291, Cambridge University Press, New York, 1991.
- Crary, A. P., Glaciological studies at Little America Station, Antarctica, 1957 and 1958, *IGY Glaciol. Rep.* 5, Int. Geophys. Year World Data Center A, Glaciol. Am. Geogr. Soc., New York, 1961a.
- Crary, A. P., Marine sediment thickness in the eastern Ross Sea area, Antarctica, *Geol. Soc. Am. Bull.*, 72, 787–790, 1961b.
- Crary, A. P., E. S. Robinson, H. F. Bennett, and W. W. Boyd, Glaciological studies of the Ross Ice Shelf, Antarctica, 1957–60, *IGY Glaciol. Rep.* 6, Int. Geophys. Year World Data Center A, Glaciol. Am. Geogr. Soc., New York, 1962.
- Davey, F. J., Geology and structure of the Ross Sea region, in *The Antarctic Continental Margin: Geology and Geophysics of the Western Ross Sea*, *Earth Sci. Ser.*, vol. 5B, edited by A. K. Cooper and F. J. Davey, pp. 1–15, Circum-Pacific Council for Energy and Mineral Resources, Houston, Tex., 1987.
- Davey, F. J., and A. K. Cooper, Gravity studies of the Victoria Land basin and Iselin Bank, in *The Antarctic Continental Margin: Geology and Geophysics of the Western Ross Sea*, *Earth Sci. Ser.*, edited by A. K. Cooper and F. J. Davey, pp. 119–137, Circum-Pacific Council for Energy and Mineral Resources, Houston, Tex., 1987.
- Denton, G. H., and H. W. Borns, Former grounded ice sheets in the Ross Sea, *Antarct. J. U. S.*, 9, 167, 1974.
- Denton, G. H., R. L. Armstrong, and M. Stuiver, Late Cenozoic glaciation in Antarctica: The record in the McMurdo Sound region, *Antarct. J. U. S.*, 5, 15–21, 1970.
- Denton, G. H., J. G. Bockheim, S. C. Wilson, and M. Stuiver, Late Wisconsin and early Holocene glacial history, inner Ross embayment, Antarctica, *Quat. Res.*, 31, 151–182, 1989.
- Drewry, D. J., Late Wisconsin reconstruction for the Ross Sea region, Antarctica, *J. Glaciol.*, 24, 231–244, 1979.
- Elliot, D. H., The Transantarctic Mountain front and the Ross embayment, *Eos Trans. AGU*, 61, 1194, 1980.
- Fastook, J. L., West Antarctica: The sea level controlled marine instability: Past and future, in *Climate Processes and Climate Sensitivity, Geophys. Monogr. Ser.*, vol. 29, edited by J. E. Hansen and T. Takahashi, pp. 275–287, AGU, Washington, D. C., 1984.
- Fillon, R. H., Late Cenozoic paleo-oceanography of the Ross Sea, Antarctica, *Geol. Soc. Am. Bull.*, 86, 839–845, 1975.
- Giovinetto, M. B., E. S. Robinson, and C. W. Swithinbank, The regime of the western part of the Ross Ice Shelf drainage system, *J. Glaciol.*, 6, 55–68, 1966.
- Gow, A. J., The inner structure of the Ross Ice Shelf at Little America V, Antarctica, as revealed by deep core drilling, *IAHS Publ.* 61, 272–284, 1963.
- Grieschar, L. L., An analysis of gravity measurements on the Ross Ice Shelf, Antarctica, Ph.D. thesis, 210 pp., Univ. of Wis., Madison, 1982.
- Grieschar, L. L., and C. R. Bentley, Isostatic equilibrium grounding line between the West Antarctic ice sheet and the Ross Ice Shelf, *Nature*, 283, 651–654, 1980.
- Grieschar, L. L., S. Shabtaie, D. G. Albert, and C. R. Bentley, Ross Ice Shelf geophysical survey, 1977–1978, *Antarct. J. U. S.*, 13, 56–59, 1978.
- Hammond, J. A., and R. L. Iliff, The AFGL gravity program, in *Proceedings of the Ninth Geodesy/Solid Earth and Ocean Physics (GEOP) Research Conference*, edited by I. Mueller, Department of Geodetic Science and Surveying, Ohio State University, Columbus, 1978.
- Harrison, J. C., and L. J. LaCoste, The measurement of surface gravity, in *Proceedings of the Ninth Geodesy/Solid Earth and Ocean Physics (GEOP) Research Conference*, edited by I. Mueller, Department of Geodetic Science and Surveying, Ohio State University, Columbus, 1978.
- Hayes, D. E., and F. J. Davey, A geophysical study of the Ross Sea, Antarctica, *Initial Rep. Deep Sea Drill. Proj.*, 28, 887–907, 1975.
- Hayes, D. E., M. Talwani, R. Houtz, and W. C. Pitman III, Preliminary report of volume 22 U.S.N.S. *Eltanin* cruises 28–32 March 1967–March 1968, *Tech. Rep. CU-1-72*, Lamont-Doherty Geol. Observ. of Columbia Univ., Palisades, N. Y., 1972.
- Hayes, D. E., J. Weissel, T. Aitken, R. Houtz, M. Talwani, R. A. Shearer, and A. B. Watts, Preliminary report of volume 26 U.S.N.S. *Eltanin* cruises 51–55A January 1972–December 1972, *Tech. Rep. CU-1-78*, Lamont-Doherty Geol. Observ. of Columbia Univ., Palisades, N. Y., 1978.
- Heiskanen, W. A., and F. A. Vening Meinesz, *The Earth and Its Gravity Field*, McGraw-Hill, New York, 1958.

- Houtz, R., and F. J. Davey, Seismic profiler and sonobuoy measurements in the Ross Sea, Antarctica, *J. Geophys. Res.*, **78**, 3448–3468, 1973.
- Kellogg, T. B., R. S. Truesdale, and L. E. Osterman, Late Quaternary extent of West Antarctic ice sheet: New evidence from Ross Sea cores, *Geology*, **7**, 249–253, 1979.
- Kirchner, J. F., and C. R. Bentley, RIGGS III: Seismic short-refraction studies using an analytical curve-fitting technique, in *The Ross Ice Shelf: Glaciology and Geophysics, Antarct. Res. Ser.*, vol. 42, edited by C. R. Bentley and D. E. Hayes, pp. 109–126, AGU, Washington, D. C., 1990.
- Kososki, B. A., A gravity study of West Antarctica, M. S. thesis, 78 pp., Univ. of Wis., Madison, 1972.
- Lambeck, K., *Geophysical Geodesy: The Slow Deformations of the Earth*, 718 pp., Oxford University Press, New York, 1988.
- Langway, C. C., Jr., Antarctic ice core studies, *Antarct. J. U. S.*, **10**, 152–153, 1975.
- Lingle, C. S., A numerical model of interactions between a polar ice stream and the ocean: Application to ice stream E, West Antarctica, *J. Geophys. Res.*, **89**, 3523–3549, 1984.
- Mayewski, P., and R. P. Goldthwait, Glacial events in the Transantarctic Mountains: A record of the East Antarctic ice sheet, in *Geology of the Central Transantarctic Mountains, Antarct. Res. Ser.*, vol. 36, edited by M. D. Turner and J. F. Splettstoesser, pp. 275–324, AGU, Washington, D. C., 1985.
- McKenzie, D. P., and C. Bowin, The relationship between bathymetry and gravity in the Atlantic Ocean, *J. Geophys. Res.*, **81**, 1903–1915, 1976.
- Morelli, C., *Geodetic Reference System 1971, Spec. Publ. 3*, 116 pp., Bureau Central de L'Association International de Géodésie, Paris, 1971.
- Nettleton, L. L., *Gravity and Magnetics in Oil Prospecting*, 464 pp., McGraw-Hill, New York, 1976.
- Robertson, J. D., Geophysical studies on the Ross Ice Shelf, Antarctica, Ph.D. thesis, 214 pp., Univ. of Wis., Madison, 1975.
- Robertson, J. D., and C. R. Bentley, Seismic studies on the grid western half of the Ross Ice Shelf: RIGGS I and RIGGS II, in *The Ross Ice Shelf: Glaciology and Geophysics, Antarct. Res. Ser.*, vol. 42, edited by C. R. Bentley and D. E. Hayes, pp. 55–86, AGU, Washington, D. C., 1990.
- Robertson, J. D., C. R. Bentley, J. W. Clough, and L. L. Greischar, Sea bottom topography and crustal structure below the Ross Ice Shelf, Antarctica, in *Antarctic Geoscience*, edited by C. Craddock, pp. 1083–1090, University of Wisconsin Press, Madison, 1982.
- Shabtaie, S., and C. R. Bentley, Tabular icebergs: Implications from geophysical studies of ice shelves, *J. Glaciol.*, **29**, 413–430, 1982.
- Shabtaie, S., and C. R. Bentley, West Antarctic ice streams draining into the Ross Ice Shelf: Configuration and mass balance, *J. Geophys. Res.*, **92**, 1311–1336, 1987.
- Shabtaie, S., C. R. Bentley, R. A. Bindschadler, and D. R. MacAyeal, Mass balance studies of ice streams A, B, and C and possible surging behavior of Ice Stream B, *Ann. Glaciol.*, **11**, 129–136, 1988.
- Simpson, R. W., R. C. Jachens, and R. J. Blakely, A new residual map of the conterminous United States with a discussion on the significance of isostatic residual anomalies, *J. Geophys. Res.*, **91**, 8348–8372, 1986.
- Stern, T. A., and U. S. ten Brink, Flexural uplift of the Transantarctic Mountains, *J. Geophys. Res.*, **94**, 10,315–10,330, 1989.
- Stuiver, M., G. H. Denton, T. J. Hughes, and J. L. Fastook, The history of the marine ice sheet in West Antarctica during the last glaciation: A working hypothesis, in *The Last Great Ice Sheets*, edited by G. H. Denton and T. J. Hughes, pp. 319–436, Wiley-Interscience, New York, 1981.
- Talwani, M., and M. Ewing, Rapid computation of gravitational attraction of three-dimensional bodies of any shape, *Geophysics*, **25**, 203–225, 1960.
- Talwani, M., J. Lamar, and M. Landisman, Rapid gravity computations for two-dimensional bodies with application to the Mendocino Submarine Fracture Zone, *J. Geophys. Res.*, **64**, 49–59, 1969.
- Tessensohn, F., and G. Wörner, The Ross Sea rift system, Antarctica: Structure, evolution and analogues, in *Geological Evolution of Antarctica*, edited by M. R. A. Thomson, J. A. Crame, and J. W. Thomson, pp. 273–277, Cambridge University Press, New York, 1991.
- Thomas, R. H., and C. R. Bentley, The equilibrium state of the eastern half of the Ross Ice Shelf, *J. Glaciol.*, **20**, 509–518, 1978.
- Thomas, R. H., D. R. MacAyeal, D. H. Eilers, and D. R. Gaylor, Glaciological studies on the Ross Ice Shelf, Antarctica, 1973–1978, in *The Ross Ice Shelf: Glaciology and Geophysics, Antarct. Res. Ser.*, vol. 42, edited by C. R. Bentley and D. E. Hayes, pp. 21–53, AGU, Washington, D. C., 1984.
- Walcott, R. I., Isostatic response to loading of the crust in Canada, *Can. J. Earth sci.*, **7**, 716–734, 1969.
- Williams, R. T., and S. Robinson, The ocean tide in the southern Ross Sea, *J. Geophys. Res.*, **85**, 6689–6696, 1980.
- Woollard, G. P., The new gravity system—Changes in international gravity base values and anomaly values, *Geophysics*, **44**, 1352–1366, 1979.

(Received April 3, 1992;
accepted July 27, 1992.)